(12) LEVEL II

DNA 4561F

ELECTRON DENSITY STRUCTURE IN BARIUM CLOUDS—MEASUREMENTS AND INTERPRETATION

Utah State University
P.O. Box 1357
Logan, Utah 84322

February 1978

Final Report for Period 1 June 1976—28 February 1978

CONTRACT No. DNA 001-76-C-0278

THIS WORK SPONSORED BY THE DEFENSE NUCLEAR AGENCY
UNDER RDT&E RMSS CODE B322077462 I25AAXHX63341 H2590D.

Prepared for
Director
DEFENSE NUCLEAR AGENCY
Washington, D. C. 20305

Destroy this report when it is no longer needed. Do not return to sender.

PLEASE NOTIFY THE DEFENSE NUCLEAR AGENCY, ATTN: TISI, WASHINGTON, D.C. 20305, IF YOUR ADDRESS IS INCORRECT, IF YOU WISH TO BE DELETED FROM THE DISTRIBUTION LIST, OR IF THE ADDRESSEE IS NO LONGER EMPLOYED BY YOUR ORGANIZATION.

(18) DNA, SBIE (19) 4561F, AD-E300 332

UNCLASSIFIED

SECURITY CLASSIFICATION OF THIS PAGE (When Data Entered)

REPORT DOCUMENTATION PAGE

READ INSTRUCTIONS BEFORE COMPLETING FORM

1. REPORT NUMBER: DNA 4561F ✓
2. GOVT ACCESSION NO.
3. RECIPIENT'S CATALOG NUMBER

4. TITLE (and Subtitle): (6) ELECTRON DENSITY STRUCTURE IN BARIUM CLOUDS— MEASUREMENTS AND INTERPRETATION

5. TYPE OF REPORT & PERIOD COVERED: (9) Final Report ~~for Period~~ 1 Jun 76—28 Feb 78
6. PERFORMING ORG. REPORT NUMBER

7. AUTHOR(s): (10) K. D. Baker, J. C. Ulwick, M. C. Kelley, L. C. Howlett, G. D. Allred, ~~D. Delorey~~, ~~N. Grossbard~~
8. CONTRACT OR GRANT NUMBER(s): (15) DNA 001-76-C-0278

9. ~~PERFORMING ORGANIZATION~~ NAME AND ADDRESS: Utah State University, P.O. Box 1357, Logan, Utah 84322 (17) X633
10. PROGRAM ELEMENT, PROJECT, TASK AREA & WORK UNIT NUMBERS: (16) Subtask I25AAXHX633-41

11. CONTROLLING OFFICE NAME AND ADDRESS: (11) Director, Defense Nuclear Agency, Washington, D.C. 20305
12. REPORT DATE: Feb~~ruary~~ 1978
13. NUMBER OF PAGES: 100

14. MONITORING AGENCY NAME & ADDRESS (if different from Controlling Office)
15. SECURITY CLASS (of this report): UNCLASSIFIED (12) 101p.
15a. DECLASSIFICATION/DOWNGRADING SCHEDULE

16. DISTRIBUTION STATEMENT (of this Report)

Approved for public release; distribution unlimited.

627101

17. DISTRIBUTION STATEMENT (of the abstract entered in Block 20, if different from Report)

18. SUPPLEMENTARY NOTES

This work sponsored by the Defense Nuclear Agency under RDT&E RMSS Code B322077462 I25AAXHX63341 H2590D.

19. KEY WORDS (Continue on reverse side if necessary and identify by block number)

Measurements in Barium Clouds
Rocketborne Measurements of Electron Density
Electron Density in Barium Clouds

20. ABSTRACT (Continue on reverse side if necessary and identify by block number)

Six instrumented rockets were used to probe three separate ion clouds that resulted from F-region barium releases, and measure electron density structure within the clouds. Two probes were launched into each of the three ion clouds, and each probe showed considerable enhancement in F-region electron density over the normal background levels. In four traversals the electron density exceeded 10^6 cm^{-3} (1,000,000/cu.cm) with a maximum of 5×10^6 cm^{-3} (5,000,000/cu.cm) observed in one case. → next page

DD FORM 1 JAN 73 1473 EDITION OF 1 NOV 65 IS OBSOLETE

UNCLASSIFIED

SECURITY CLASSIFICATION OF THIS PAGE (When Data Entered)

78 08 25 016
362 850

20. ABSTRACT (Continued)

Two showed dramatic structure in the electron density profiles associated with passage through striated portions of the cloud. These structures had spatial extent as measured by the rocket probes normal to the terrestrial magnetic field of hundreds of meters with the density changing by factors of from about 2 to 10 as the probes passed into and out of the structure. The change of density on some of the features had particularly fast drop off, corresponding to less than 20 meters travel normal to the magnetic field.

TABLE OF CONTENTS

TABLE OF CONTENTS (cont.)

LIST OF ILLUSTRATIONS

LIST OF ILLUSTRATIONS (cont.)

LIST OF ILLUSTRATIONS (cont.)

LIST OF TABLES

1. INTRODUCTION

A program of measurements to investigate radio wave propagation through ionospheric regions perturbed by the presence of ionized, barium-vapor clouds, was undertaken during the period extending from December, 1976 through mid-March, 1977. These investigations have been termed the STRESS (Satellite Transmission Effects Simulations) Program. The primary objective of the program was to define and correlate the effects on radio wave propagation with observed characteristics of the ionized barium regions through which the radio waves were propagated. Fundamental to these studies were high spatial resolution measurements of ionospheric electron density structure within the ionized barium regions and particularly within the striated portions of the clouds. These investigations were the objective of the rocket probe measurements program reported herein.

The desired measurements were achieved by releasing barium vapor from rockets upon attaining altitudes of approximately 185 km. The timing of the releases was such that the region was sunlit. Subsequently, as the barium-vapor was ionized and developed striations, additional rocket-borne payloads, equipped with instrumentation to make fine-scale measurements of electron density, were launched in an effort to penetrate the striated portion of the ionized clouds. These probes provided profiles of electron density and fine-scale structure (~1 m) internal to the clouds as the payloads traversed these regions and external to the clouds throughout the remainder of the flights.

The investigations were conducted from Eglin Air Force Base, Florida. Twelve rockets were used in the program. Six of these were two-stage, Honest John-Hydac vehicles equipped for 48 kg chemical (barium) releases at predetermined altitudes. Six additional vehicles, two-stage Nike-Hydacs, were instrumented with electron density probes and VHF transmitters. Ground-based and aircraftborne instrumentation provided coverage related to vehicle and cloud tracking and radio wave propagation effects.

The initial barium release (Anne) was accomplished in December, 1976 as a certification round for program readiness and was not probed for electron density measurements or propagation effects. Subsequent flights were conducted during late February and early March, 1977 with electron density probes accomplished for the last three barium releases. After each barium release, radar tracking, and optical tracking (where possible) of the resulting cloud provided inputs for computer prediction of probe launch azimuth and elevation for a given launch time. These coordinates were planned to permit the probes to intercept and penetrate the ionized portion of the barium cloud. Figure 1.1 is a scenario of STRESS launches for a typical barium event. Table 1.1 is a summary of launches accomplished during the STRESS program.

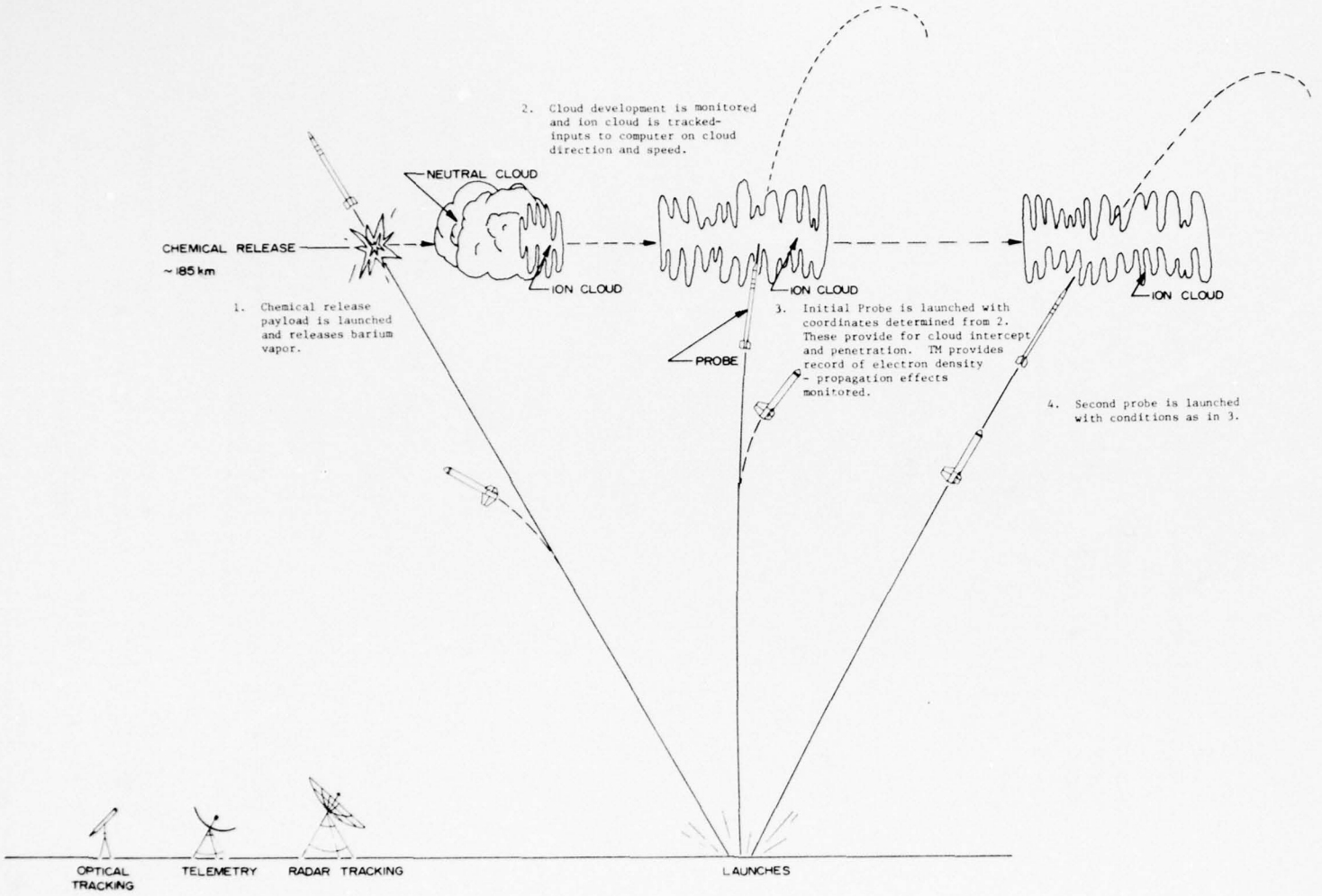

Figure 1.1. A scenario of rocket launches for a typical barium event during project STRESS.

TABLE 1.1

VEHICLE LAUNCH SUMMARY - PROJECT STRESS

Vehicle	Event Name	Experiment	Launch Date/Time	Remarks
ST610.31-1	Anne	Barium Release	1 Dec 76 2308:37(GMT)	Certification
ST710.31-2	Betty	Barium Release	26 Feb 77 2349:33(GMT)	Not Probed
ST710.31-3	Carolyn	Barium Release	2 Mar 77 2351:00(GMT)	Not Probed
ST710.31-4	Dianne	Barium Release	7 Mar 77 2358:00(GMT)	Probed at Release +15 min by ST707.51-1 Probed R(Release) +33 min by ST707.51-2
ST707.51-1	Dianne	Probe	8 Mar 77 0014:05(GMT)	Dianne early probe R + 15 min.
ST707.51-2	Dianne	Probe	8 Mar 77 0032:04(GMT)	Dianne late probe R + 33 min.
ST710.31-5	Esther	Barium Release	13 Mar 77 2258:00(GMT)	Probed at R + 28 min by ST707.51-3 Probed at R + 46 min by ST707.51-4
ST707.51-3	Esther	Probe	13 Mar 77 2327:00(GMT)	Esther early probe R + 28 min
ST707.51-4	Esther	Probe	13 Mar 77 2344:50(GMT)	Esther late probe R + 46 min
ST710.31-6	Fern	Barium Release	14 Mar 77 2243:00(GMT)	Probed at R + 41 min by ST707.51-5 Probed at R + 80 min by ST 707.51-6
ST707.51-5	Fern	Probe	14 Mar 77 2325:20(GMT)	Fern early probe R + 41 min
ST707.51-6	Fern	Probe	15 Mar 77 0003:10(GMT)	Fern late probe R + 80 min

2. PAYLOADS - CONFIGURATION AND INSTRUMENTATION

All of the six payloads for probing the barium ion clouds were identical, and all were propelled by two-stage Nike-Hydac motors. The pre-launch vehicle configuration is shown in Figure 2.1. As can be noted from Figure 2.1, the payloads consisted of four separate sections: The main payload (including the nosespike), an Amplitude Modulated, P-band propagation experiment, telemetry and beacon, and a section for ballast to achieve desired vehicle performance and payload stability. The main payload, illustrated in Figure 2.2, contained two electron density measuring instruments, a plasma frequency probe, and a DC probe. Each of these probes utilized a portion of the 1-m long, 6.35-cm diameter nosespike as their sensing element in contact with the ionospheric plasma. The payload spin axis symmetry and freedom from payload doors and mechanisms produced a flight unit that was simple, rugged, and caused minimal effects from wakes or spin modulation in the obtained data.

In addition to the instrumentation for measurement of ionospheric electron density, each payload included a Heliflux RAM 5C magnetic aspect sensor mounted across the rocket's major axis to provide a measure of rocket spin and to give some indication of vehicle attitude and stability. A C-band radar transponder was included to provide a signal for solid radar tracking, and an S-band telemetry system, operating at a link frequency of 2251.5 MHz provided for data transmission to the ground station. Table 2.1 details the telemetry IRIG channels and assignments. Total payload weight for the probes was 130 lbs, with the main payload weighing in at 70 lbs.

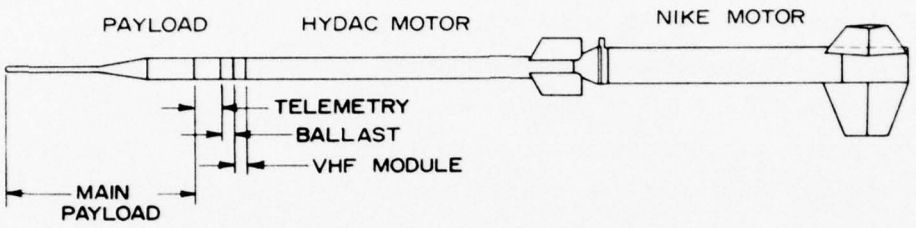

Figure 2.1. STRESS electron density probe pre-launch configuration.

TABLE 2.1

PROJECT STRESS PROBE TELEMETRY ASSIGNMENTS

IRIG Channel	Assignment	IRIG Channel	Assignment
21	DC Probe x10	17	DC Probe x100
20	DC Probe x1	16	PFP Digital
19	ΔPFP	15	DC Probe x1000
18	PFP Analog	13	Magnetometer

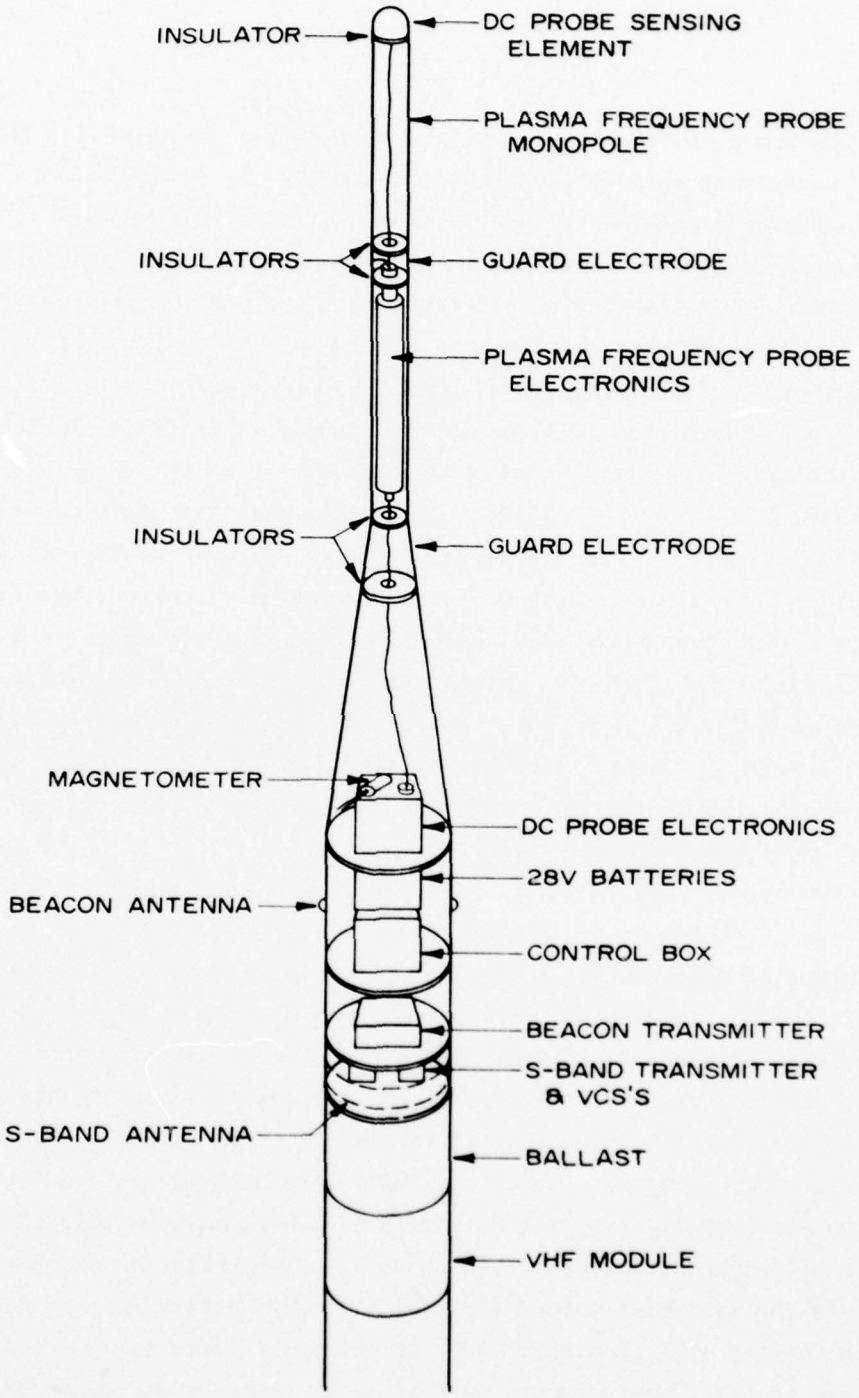

Figure 2.2. STRESS payload configuration.

DC Probe

The DC probe operates on the principle that the electron flow to a small, positively charged electrode immersed in the ionospheric plasma is directly related to the electron density of the plasma. Figure 4 is a conceptual block digram of the DC probes used in the STRESS program. As its sensing electrode in contact with the ionospheric plasma, the DC probe uses the foremost segment of the payload nose spike (see Figure 2.2) with dimensions as noted in Figure 2.3.

The operation of the DC probe is exceptionally simple and is illustrated in Figure 2.3. The current collected by the 63 cm^2 probe electrode (the forward 4.76 cm of the payload nose spike) which is biased at +3 V with respect to the rest of the payload, is fed to the electronics system preamplifier at B. With a finite sensing electrode current caused by electron flow from the plasma to the electrode, the voltages at C and D are not equal, and the differential stage amplifies the difference giving an output which is proportional to the sensing electrode current flow. The output from the differential amplifier is fed to four amplifiers having gains of x1, x10, x100, and x1000 with the four outputs going to the payload telemetry section.

The DC probes used in the STRESS program were designed to be capable of measuring fine-scale spatial variations of electron density. This high spatial resolution capability is determined by the dimension of the probe electrode, the payload velocity, and the electrical bandwidth of the telemetry system. For these applications the telemetry system bandwidth and the payload velocity through the ion cloud of approximately 1 km/sec limits the DC probe spatial resolution to the order of 30 cm.

The DC probe current cannot be related independently to electron with high absolute accuracy but will give reliable relative values. This does not present a serious draw-back here since the relative changes $\Delta N_e/N_e$ are the important values and over a limited altitude range the electron density will be proportional to the probe current. By cross comparison to other measurements such as an rf probe or an ionosonde the DC probe can be calibrated in absolute numbers. This is the manner in which we utilize this probe.

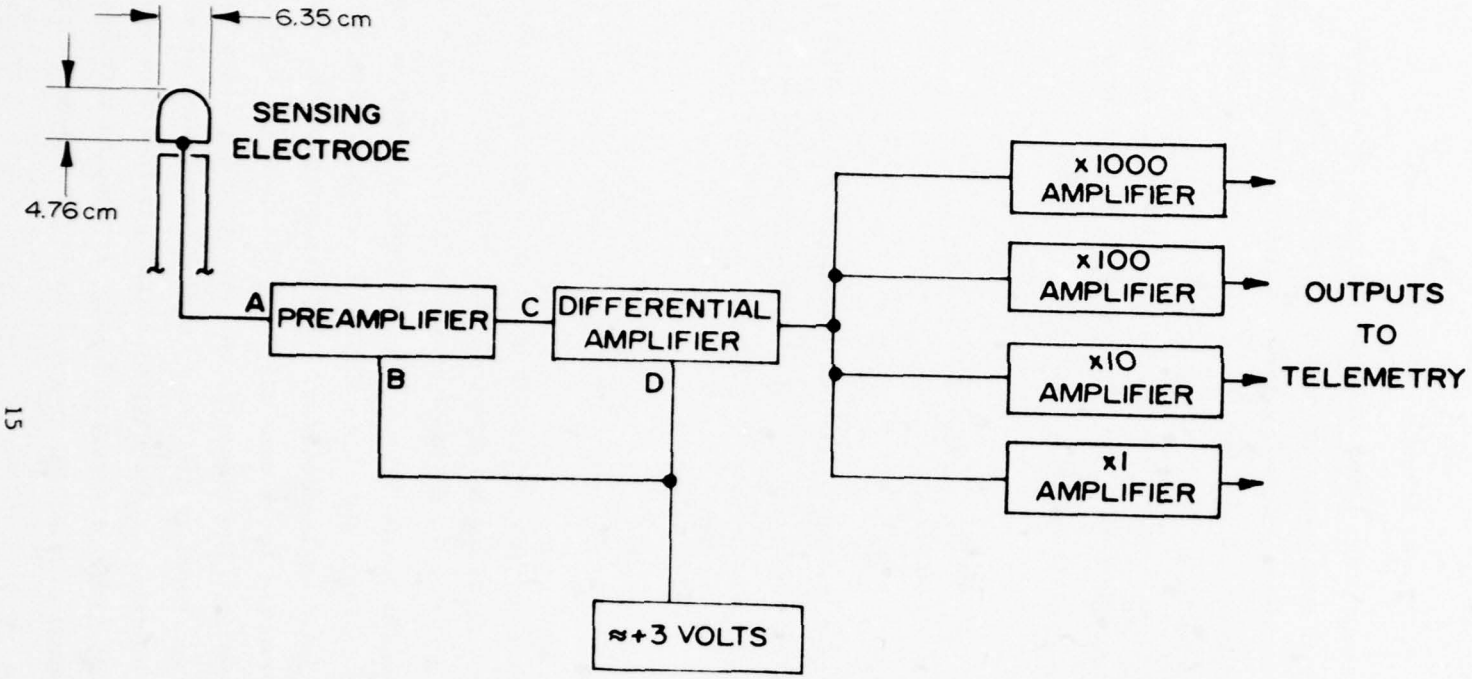

DC PROBE BLOCK DIAGRAM

Figure 2.3. Block diagram of DC probe.

Plasma Frequency Probe

The plasma frequency probe (PFP) utilizes the well established relationships between plasma frequency, electron density, and the reactance of a probe immersed in the plasma to provide a measurement of electron density (*Baker, et al.*, 1969). In the version of the PFP flown in the STRESS program a phase-locked loop is used to track the frequency that produces zero phase angle between rf current and voltage being fed to the sensing antenna. This frequency of resonance is closely related to the electron plasma frequency, in kHz

$$f_N^2 = \frac{e^2 N_e}{4\pi^2 m_e} = 80.6 \times 10^6 N_e(cm^{-3})$$

In the absence of a magnetic field the resonance occurs at this electron plasma frequency. The effect of the magnetic field is to shift the resonance slightly higher in frequency to the upper hybrid frequency

$$f_H^2 = \sqrt{f_N^2 + f_B^2} \quad , \text{where } f_B = \frac{eB}{2\pi m_e}$$

The phased-locked version of the PFP which is shown in the block diagram in Figure 2.4 utilizes the forward half of the 1-m long nose as its antenna. The system is designed to sense the zero phase condition of the antenna impedance at the hybrid resonant frequency and to cause a phase-locked loop to force the rf oscillator to track the frequency producing the zero phase angle condition. The frequency of the oscillator is digitally counted for 1 msec and forms the data for a digital plasma frequency readout. Additionally, the voltage controlling the loop oscillator is monitored to provide an analog measurement of plasma frequency and loop operation. The digital output provides excellent accuracy in the measurement of electron density at samples with about a meter spatial dimension separated in space by the distance the payload

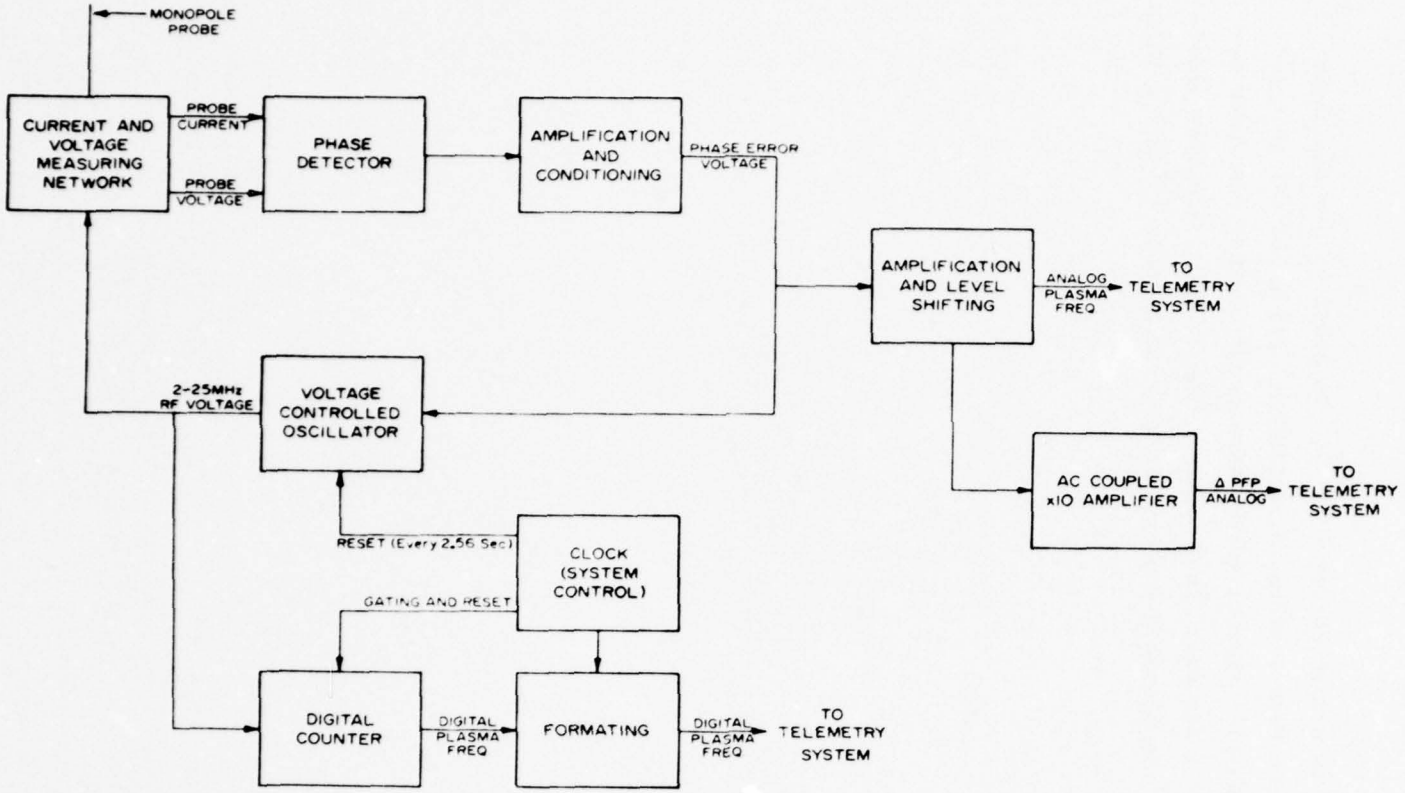

PLASMA FREQUENCY PROBE BLOCK DIAGRAM

Figure 2.4. Block diagram of plasma frequency probe.

travels in a 16-ms sample period (~25 m). In order to provide higher spatial resolution measurements, a continuous analog channel and ac-coupled x 10 amplified channel (ΔPFP) were provided that responded down to about 1 meter scale size fluctuations. The range of electron densities covered by the plasma frequency probe is from about 10^5 to 7 x $10^6 cm^{-3}$.

3. STRESS PROBE FIRING SUMMARY AND GEOMETRY

The electron density probe rockets were flown in pairs into the last three barium clouds as briefly summarized earlier in Table 1.1 and elaborated on in Table 3.1 which includes a listing of parameters relevent to the description of each flight.

Probe encounters with the barium clouds are described in Table 3.2 where entries under "probe residence in the Ba cloud" were determined from significant electron density enhancements over background as determined from the in-situ probe results. The age of the cloud is given in minutes after release for the maximum observed electron density on each probe flight.

To assist in visualizing the probe/cloud encounter and penetration, Figures 3.1 through 3.5 are conceptual drawings which include the geographic coordinates of the launches, the vehicle ground track and trajectory, coordinates of the barium release, and subsequent development of the barium cloud. Probe entry point into the cloud, point of maximum electron density, and exit point (all from electron density results) are marked by dots along the rocket trajectory. Rocket apogee is noted in each figure as is the track of the barium cloud vs. time.

The flight of rocket ST707.51-6 is omitted from these conceptual drawings as the cloud track on this probe was doubtful, and the electron density measurements were of limited usefulness as noted later in this report (section 5).

In viewing the electron density results presented in section 5 of this report, it is important to consider the velocity of each probe as it moves through the ion cloud region. Since the ion cloud structure will be aligned along magnetic field lines, perhaps the most important velocity will be that normal to the magnetic field. To aid in viewing the data the pertinent rocket velocities for each probe flight are summarized in Table 3.3 for the region of the maximum measured electron density in each case. V_t is the total rocket velocity having vertical and horizontal components of V_V and V_H, respectively. $V_{||}$ and $V_{\perp}$ are the velocity of the rocket parallel to and perpendicular to the terrestrial magnetic field.

TABLE 3.1

SUMMARY OF PROBE ROCKET FLIGHT CHARACTERISTICS

Event	Rocket No.	Launch Time (UT)	Agogee (km)		Range (km)	Flight Azimuth deg	Roll Rate RPS	Precession Period (sec)	Approximate Precession $^1/_2$ angle, deg
DIANNE	ST707.51-1	00:14:05	213	@	221	156	7	34	8
DIANNE	ST707.51-2	00:32:04	203	@	231	146	7	36	7
ESTHER	ST707.51-3	23:27:00	220	@	191	156	7	37	5
ESTHER	ST707.51-4	23:44:50	199	@	238	146	6.4		0
FERN	ST707.51-5	23:25:20	249	@	164	162	7	32	3
FERN	ST707.51-6	00:03:10	222	@	204	149	7	36	5

TABLE 3.2

SUMMARY OF STRESS PROBE FLIGHTS

Event	Probe Vehicle No.	Probe Launch Time (UT)	Probe Residence in BA Cloud		Age of Cloud	Cloud Features
			Alt,km	(t + sec)		
DIANNE	ST707.51-1	00:14:05	151-175	(120-145)	15 min	Cloud developed a kink
DIANNE	ST707.51-2	00:32:04	178-183	(156-164)	34 min	Two striated portions of cloud
ESTHER	ST707.51-3	23:27:00	160-192	(123-160)	28 min	Striations not yet developed
ESTHER	ST707.51-4	23:44:00	155-181	(130-165)	46 min	Well-developed striations
FERN	ST707.51-5	23:25:20	131-203	(92-152)	42 min	Cloud dropped rapidly (no optical coverage)
FERN	ST707.51-6	00:03:10	112-206	(83-180)	80 min	Beginning of optical coverage

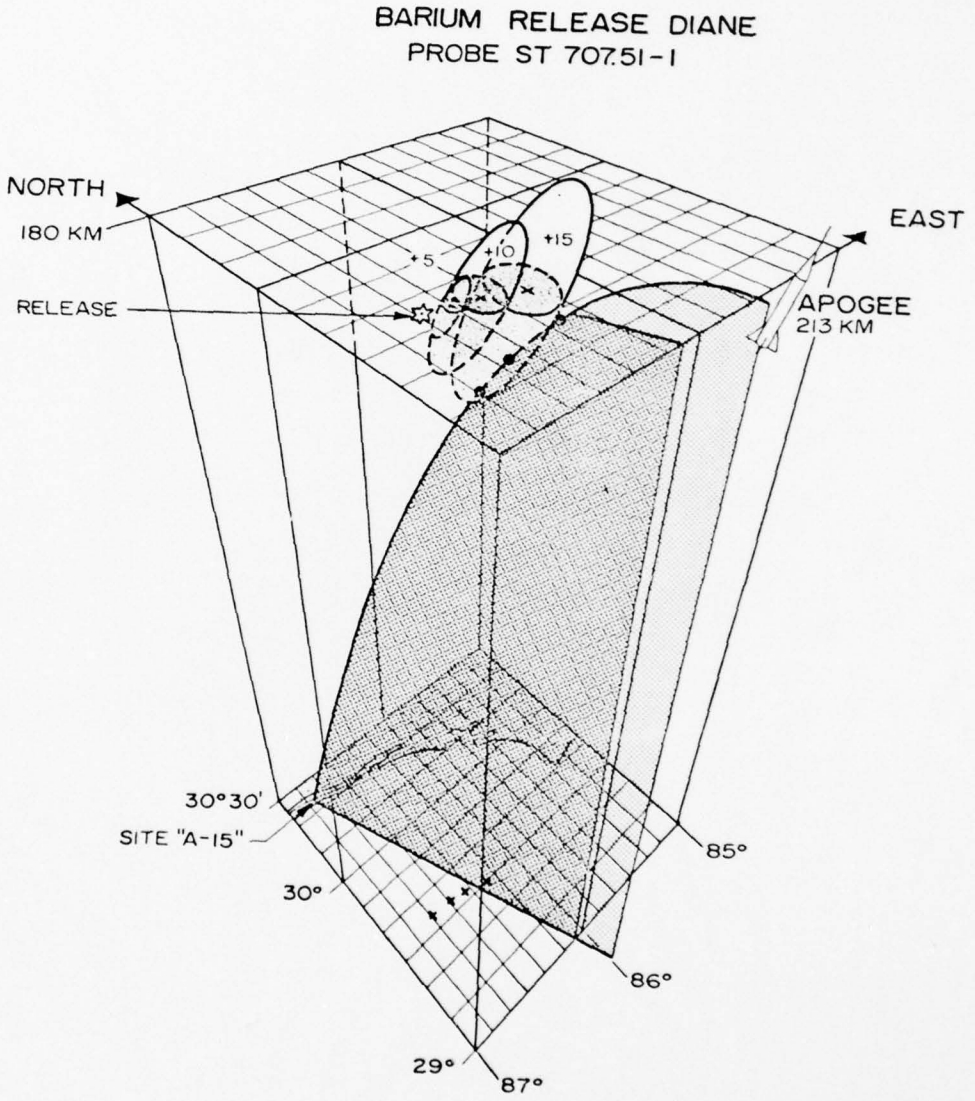

Figure 3.1. Illustration of probe rocket ST707.51-1 trajectory. Release point of Event Diane is shown along with the visible ionized cloud track points at R+5, 10 and 15 minutes. Rocket entry point into the cloud, maximum point and exit point (from electron density results) are indicated by the 3 dots along the trajectory

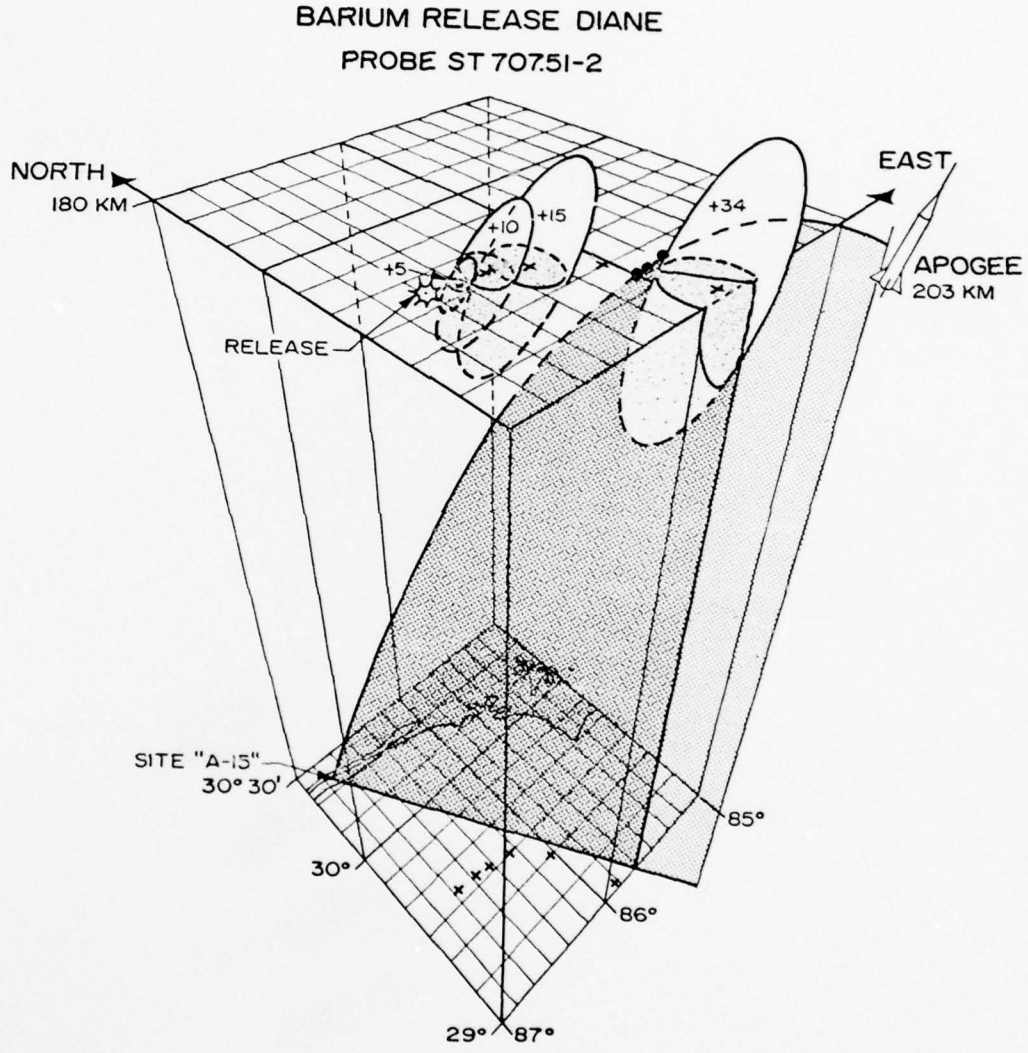

Figure 3.2. Illustration of probe rocket ST707.51-2 trajectory. Release point of Event Diane is shown along with the visible ionized cloud track points at R+5, 10, 15, 34 minutes. Rocket entry point into the cloud, maximum point and exit point (from electron density results) are indicated by the 3 dots along the trajectory.

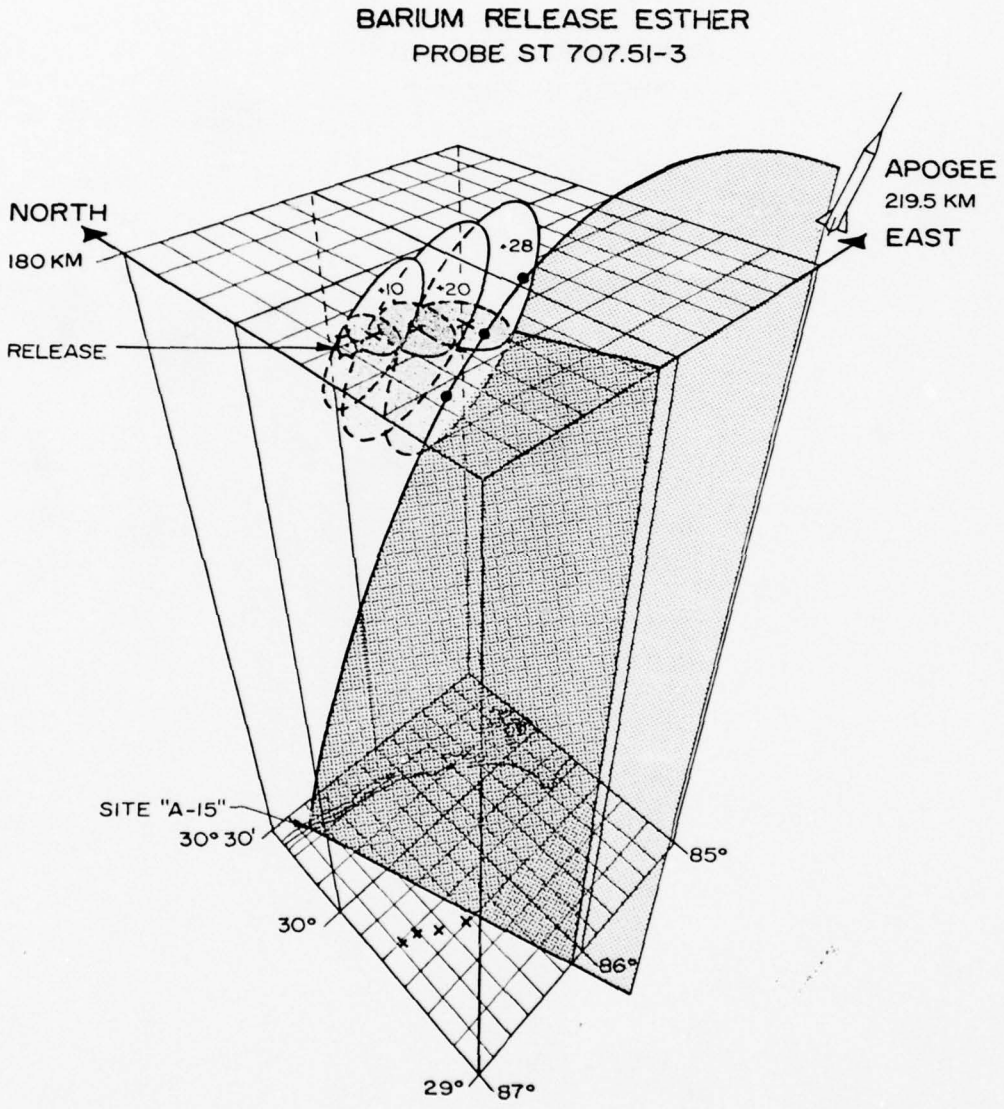

Figure 3.3. Illustration of probe rocket ST707.51-3 trajectory. Release point of Event Esther is shown along with the radar cloud track points at R+10, 20, 28 minutes. Rocket entry point into the cloud, maximum point and exit point (from electron density results) are indicated by the 3 dots along the trajectory.

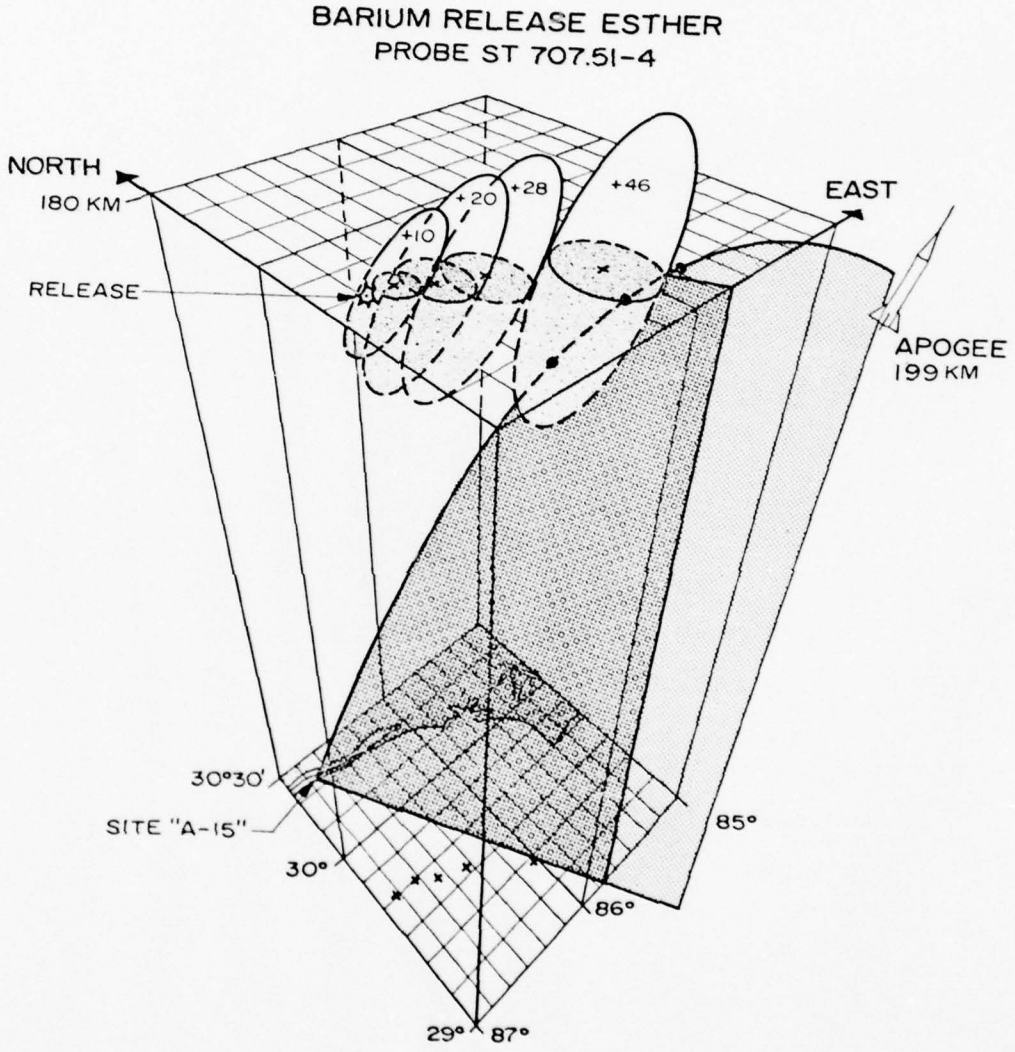

Figure 3.4. Illustration of probe rocket ST707.51-4 trajectory. Release point of Event Esther is shown along with the radar cloud track points at R+10, 20, 28, 46 minutes. Rocket entry point into the cloud, maximum point and exit point (from electron density results) are indicated by the 3 dots along the trajectory.

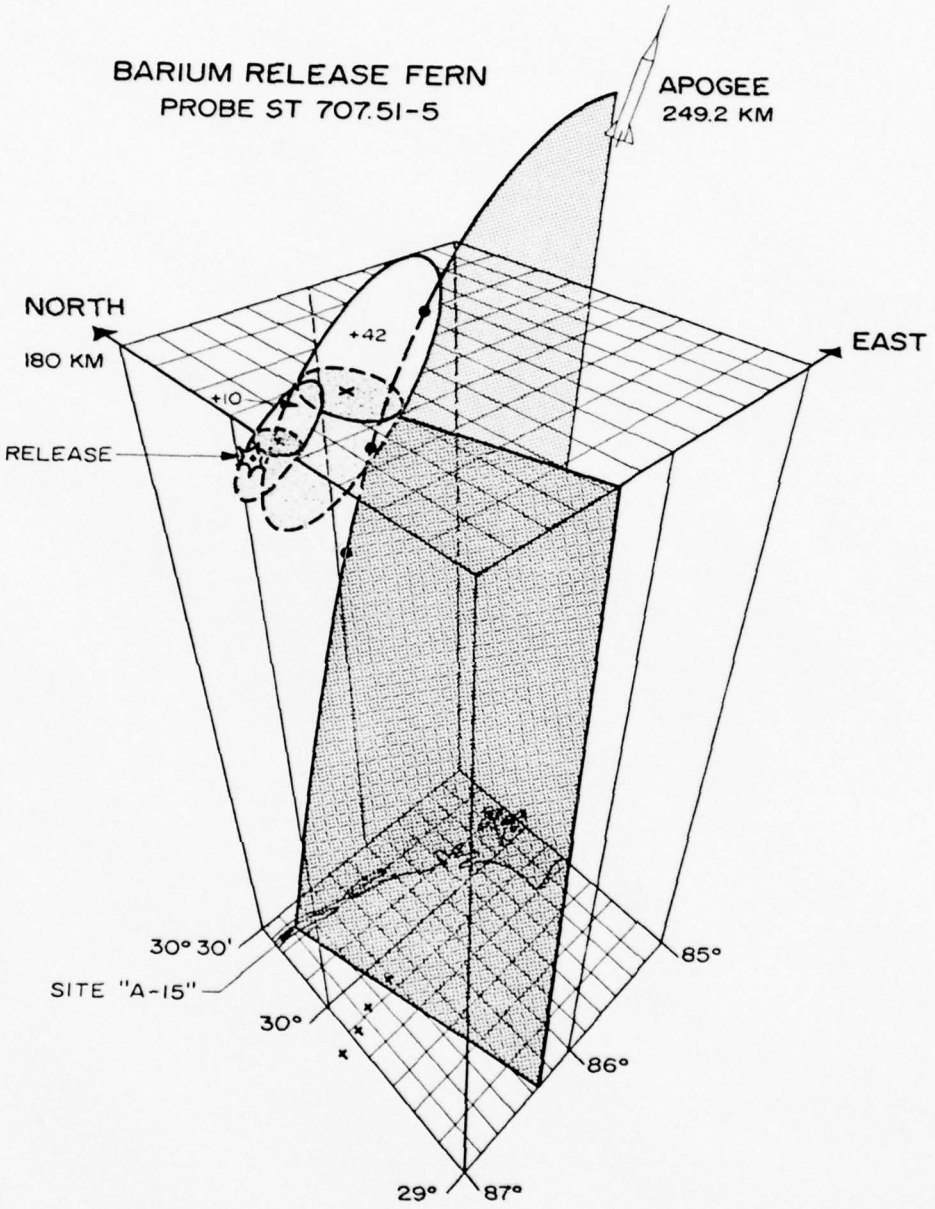

Figure 3.5. Illustration of probe rocket ST707.51-5 trajectory. Release point of Event Fern is shown along with the radar cloud track points at R+10, 42 minutes. Rocket entry point into the cloud, maximum point and exit point (from electron density results) are indicated by the 3 dots along the trajectory.

TABLE 3.3

SUMMARY OF ROCKET PROBE VELOCITIES

Rocket No.	Altitude of Maximum N_e; (km)	V_t (km/s)	V_v (km/s)	V_h (km/s)	$V_{\parallel}$ (km/s)	$V_{\perp}$ (km/s)
ST707.51-1	162	1.41	0.98	1.01	-1.29	0.58
ST707.51-2	182	1.25	0.62	1.09	-0.95	0.81
ST707.51-3	177	1.25	0.89	0.88	-1.15	0.50
ST707.51-4	173	1.31	0.71	1.10	-1.04	0.80
ST707.51-5	171	1.37	1.19	0.68	-1.34	0.26
ST707.51-6	160	1.41	1.06	0.93	-1.29	0.56

4. DATA REDUCTION

Data Reduction Overview

Figure 4.1 depicts the flow of data through the sequence of routines developed to produce the final STRESS data products. The raw data for each probe, stored on magnetic tape, consisted of a GMT time tag and associated digital counts. Individual processing routines were developed for each of the STRESS probes and these routines converted the raw counts to engineering units, computed vehicle altitude associated with each measurement and created the engineering unit/trajectory data base used as input to various plot, list, and analysis routines. The plot/list routines provided the capability of displaying time and altitude profiles of the engineering unit data for the entire data set or for selected periods of interest. A description of the mathematics involved in the reduction routines is included in a succeeding section.

Engineering Unit/Trajectory Merge Routines

Individual routines were tailored for each of the STRESS probes (PFP analog, PFP digital and DC probe). Each routine computed vehicle altitude based on a quadratic fit to the raw trajectory data. A least square polynomial routine was used in deriving the trajectory coefficients. Table 4.1 summarizes the coefficients for each of the vehicles.

For the PFP analog and the DC probe data, the digital counts contained on the raw data tape were converted to voltage using conversion factors received with each magnetic tape. The data on the PFP Digital raw data tapes represented direct measurements of frequency.

DC probe routines converted the voltage values (v) to current (I) using the linear conversion expressions. The probe currents were converted to electron densities by multiplication by the appropriate constant over each altitude range as determined by comparison with the plasma frequency probe and ionosonde data.

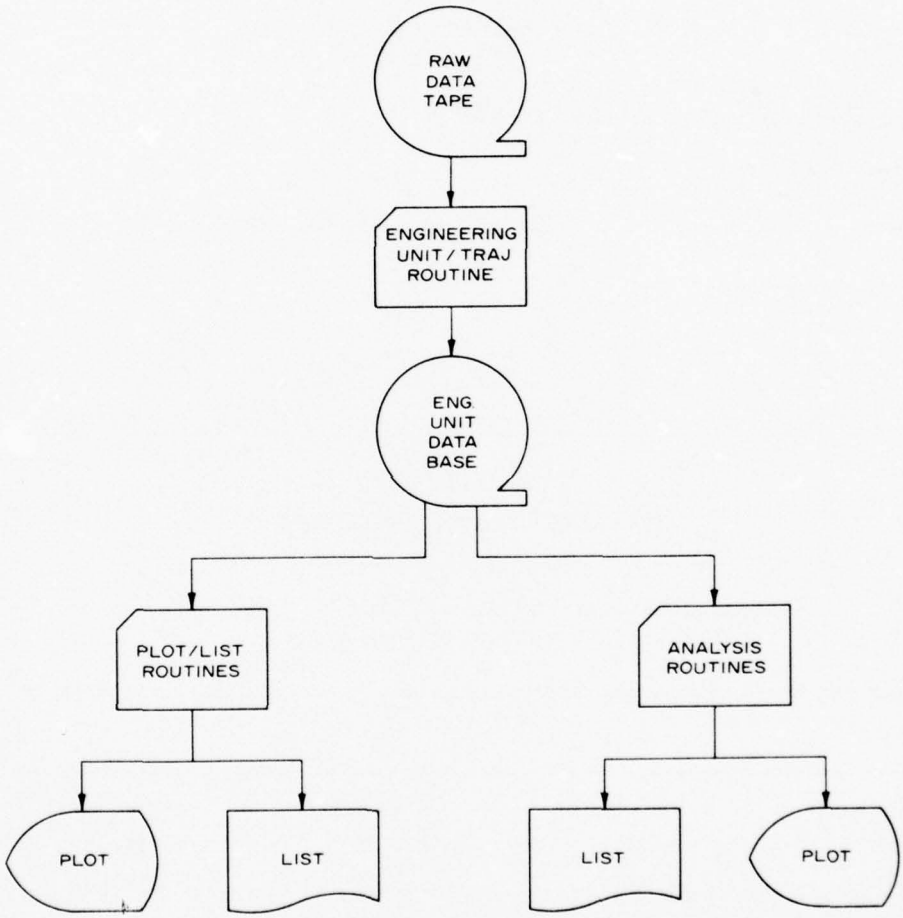

Figure 4.1. Project STRESS data flow.

For the PFP Analog data, voltage (v) was converted to frequency (f) by means of linear calibrations. Frequency for both the PFP Analog and PFP digital data was converted to electron density(N_e) using the expression

$$N_e = 1.24 \times 10^4 [f^2 - (1.5)^2] \text{ cm}^{-3}$$

where f is the measured frequency in MHz.

TABLE 4.1

TRAJECTORY COEFFICIENTS

Trajectory Equation $ALT = at^2 + bt + c$
(t = time in seconds after launch)

Vehicle	a	b	c
ST707.51-1	-.0046	2.18059	-44.0714
ST707.51-2	-.0045	2.0799	-36.798
ST707.51-3	-.0045	2.157	-36.896
ST707.51-4	-.0045	2.0633	-37.102
ST707.51-5	-.0045	2.296	-41.853
ST707.51-6	-.0045	2.1605	-36.6054

Spectral Analysis of Electron Density Variations

A computer program was developed to analyze the variations in the current ($\Delta I/I$) or density ($\Delta N/N$) as a function of time by power spectral density analysis techniques. Negative or zero values (density) indicated a reset pulse of the PFP was being read. The program did not accept data values up to 19 points before or 299 points after a reset pulse. The program linearly interpolates or extrapolates to fill in the gaps in the data created by the reset pulse.

The program analyzes NPOIN + 1 (NPOIN is the number of input data points usually 8192) decimated data points at a time. Each point is found by averaging (decimating) LDEC (input data usually 1 or 5) input points. The program averages the results to form LNN (input data usually 1 or 5) consecutive samples of I (or N) where the last value of one sample is the first value of the next sample.

The program analyzes NPOIN + 1 points as follows. The data is detrended by fitting a least squares polynomial of degree NORDER (input data) to all the input data (not including any interpolated or extrapolated values). Form the values

$$f(t) = \frac{I(t)[\text{or } N(t)]}{y(t)}$$

where $I(t)$ is the value of I and $y(t)$ is the value of the polynomial both at time t. Now calculate

$$\bar{E} = \frac{1}{N} \Sigma[f(t) - \bar{f}(t)]^2$$

where the sum is over the NPOIN + 1 data values and N equals NPOIN + 1 - number of interpolated or extrapolated data values and

$$\bar{f}(t) = \frac{1}{\text{NPOIN} + 1} \Sigma f(t) \quad .$$

Form

$$g(t) = f(t + \Delta t) - \alpha f(t) \quad (\alpha \text{ input data, usually } 1)$$

where Δt is the equal time spacing of the data. Form

$$h(\omega) = \Sigma g(t)^{j\omega t}$$

where

$$j = \sqrt{-1}$$

$$\omega = 0, \pm \omega_R, \pm 2\omega_R, \pm 3\omega_R, \ldots, \pm 4096\omega_R$$

where

$$\omega_R = \frac{2\pi}{8192 * \Delta t} \quad ,$$

$h(\omega)$ is found by using a Fast Fourier Transform on $\Sigma g(t)$.

Form $g_1(\omega) = |g(\omega)|^2$ and smooth the resultant "whitened" power spectral density through Hamming to form $g_2(t)$. Thus

$$g_2(\omega_R) = g_1(\omega_R)$$

$$g_2(\ell\omega_R) = 0.23\left(g_1[(\ell - 1)\omega_R] + g_1[(\ell + 1)\omega_R]\right) + 0.54\, g_1(\ell\omega_R)$$
$$\text{for } \ell = 2, 3, \ldots, 4095$$

$$g_2(4095\,\omega_R) = g_1(4095\,\omega_R)$$

$$g_2(4096\,\omega_R) = g_1(4096\,\omega_R)$$

Find

$$\bar{E}_f = \frac{1}{4096} \sum_{\ell=1}^{4096} g_2(\ell\omega_R) / \left([1 - \alpha \cos(\frac{\pi\ell}{4096})]^2 + \alpha^2 \sin^2(\frac{\pi\ell}{4096})\right) \quad .$$

Renormalize g_2 to form normalized answers g_3

$$g_3(\omega) = \frac{\Delta t\ \bar{E}}{\pi\ \bar{E}_f}\ g_2(\omega)$$

$g_3(\omega)$ is the whitened power spectral density

and

$$g_4(\ell\omega_R) = g_3(\ell\omega_R)/\ [1 - \alpha \cos(\frac{\pi\ell}{4096})]^2 + \alpha^2 \sin^2(\frac{\pi\ell}{4096})$$

is the final power spectral density.

The frequency is often transformed to a wavenumber reading by dividing $\ell\omega_R$ by an appropriate velocity constant (FIXTXS). For short-wavelength calculations FIXTXS $= \frac{1}{N} \Sigma |\vec{V} \times \vec{B}|$ where $\vec{V}$ is the rocket velocity (found from a model) and $\vec{B}$ is the magnetic field (found from a model). The sum is over all non-extrapolated or interpolated data values. Similarly, for long-wavelength calculations let $\vec{w} = \vec{B} \times \vec{U}$ and then forming a unit $y = \frac{\vec{w}}{|\vec{w}|}$ we have FIXTXS $= |\vec{V} \cdot \vec{y}|$. Here $\vec{U}$ is a vector pointing from the center of the cloud in the direction of $-(\vec{E} \times \vec{B})$ based on model of cloud development (see section 7 and particularly Eqn. 7.4)

$$\vec{U} = \vec{V}_n - \frac{\vec{E} \times \vec{B}}{|B|^2} \quad .$$

Two types of plots have been provided: the first is a plot of the irregularity amplitude distribution (square-root of Power $[g_4(f)]$ versus frequency ($f = \frac{\omega}{2\pi}$)) and the second is Power $[g_4(\text{wave-number})]$ * FIXTXS versus wavenumber. Both of these plots are on a $\log_{10}$ versus $\log_{10}$ scale.

5. ELECTRON DENSITY RESULTS

Electron density measurements were attained on all 6 flights. The plasma frequency probe indicated proper lock onto the plasma resonance frequency during all regions of interest with data being available on both the straight analog channel and the ΔPFP channel. The digital counter, however, failed at liftoff on all but rocket ST707.51-5. The failure did not negate the probe measurements but did make absolute electron density values more difficult to ascertain. The repeating difficulty was attributed to failure of an integrated circuit comparator used to interface the rf oscillator to the digital frequency counter. In the field attempts to determine exact cause of the failure and to alleviate the problem were not successful with the possible exception of probe ST707.51-5 which did give complete results on the digital channel as well as the analog channel. The cause of the integrated circuit failures is still not understood past the fact that it appears that a high voltage transient is somehow generated in conjunction with the rocket ignition that is coupled back through the antenna to the comparator and wipes it out.

The DC probe provided consistently good results on all but the last flight (ST707.51-6). Some difficulty was encountered with the high humidity at the launch site producing leakage currents, but these did not impair the measurements in the region of the barium cloud except on rocket ST707.51-6 which did not yield any meaningful data. Data were obtained on the analog PFP channel but are of limited accuracy.

The electron densities profiles are presented for each rocket flight.

Rocket ST707.51-1
(Dianne, R+15 min)

The electron density profile measured on rocket ST707.51-1 flown at release +15 minutes for event Dianne is shown in Figure 5.1. Also shown for comparison is the approximate electron density profile of the undisturbed ionosphere (dotted line) as determined by probe measurements

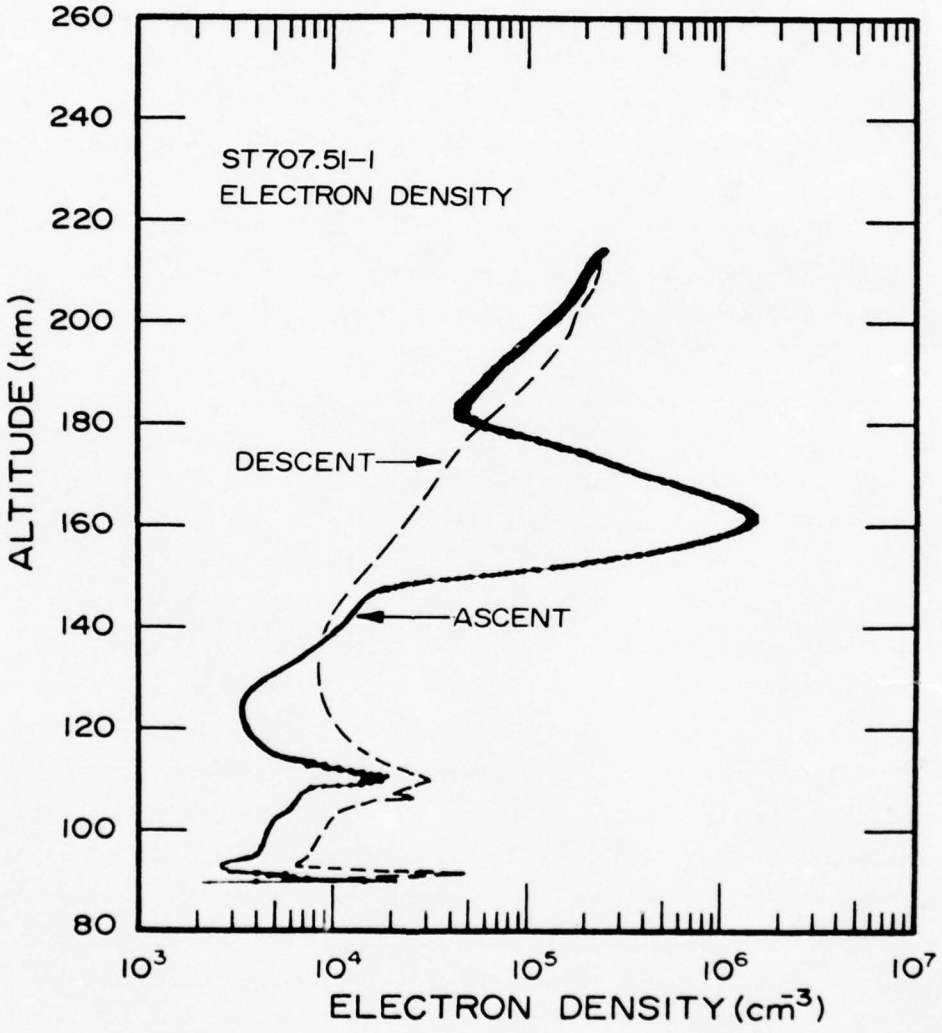

Figure 5.1. Electron density profile from probe flight ST707.51-1 on event Dianne (R+15 min). The dashed line shows the undisturbed F-region.

above and below the cloud region and measurements on rocket descent. A check was also made by comparing the F-region density with the ground based ionosonde value. It is obvious that the rocket probe traversed the region of enhanced electron density associated with the barium ion cloud over the altitude range from about 150 to 180 km. The peak electron density of the barium cloud layer of $1.4 \times 10^6 cm^{-3}$ found at 162 km is about a factor of 100 larger than the electron density at that altitude in the undisturbed ionosphere. The layer is relatively smooth and devoid of large scale structure that would be expected if cloud striations had been penetrated. The layer has a width at half amplitude of 10 km in vertical extent which would correspond to a movement of the rocket probe of 6 km across the terrestrial magnetic field.

Rocket ST707.51-2
(Dianne, R+34 min)

Rocket probe ST707.51-2 was flown in event Dianne about 19 minutes after ST707.51-1 and just penetrated the edge of the ion cloud as can be seen in the profile presented in Figure 5.2. The peak density found was the same as the earlier probe ($1.4 \times 10^6 cm^{-3}$) but the penetration was at the higher altitude of 182 km. The sharp feature at 182 km has an electron density about 2 orders of magnitude over the ambient density and is imbedded in a broader region of enhanced density more of the shape of the profile found on ST707.51-1, but with less density and at a higher altitude. The apparent higher altitude of the layer is due to the late penetration of the cloud since the rocket flew to the north of the cloud (see section 3, Figure 3.2). The sharp finger rises above the broader region by about an order of magnitude. The finger has a width (half amplitude) of about 1.5 to 2 kilometers in extent either vertically or normal to B.

Rocket ST707.51-3
(Esther R+28 min)

The electron density profile measured on probe rocket ST707.51-3 which penetrated the barium cloud Esther at about 28 minutes after release is shown in Figure 5.3. The profile is smooth, showing no large scale

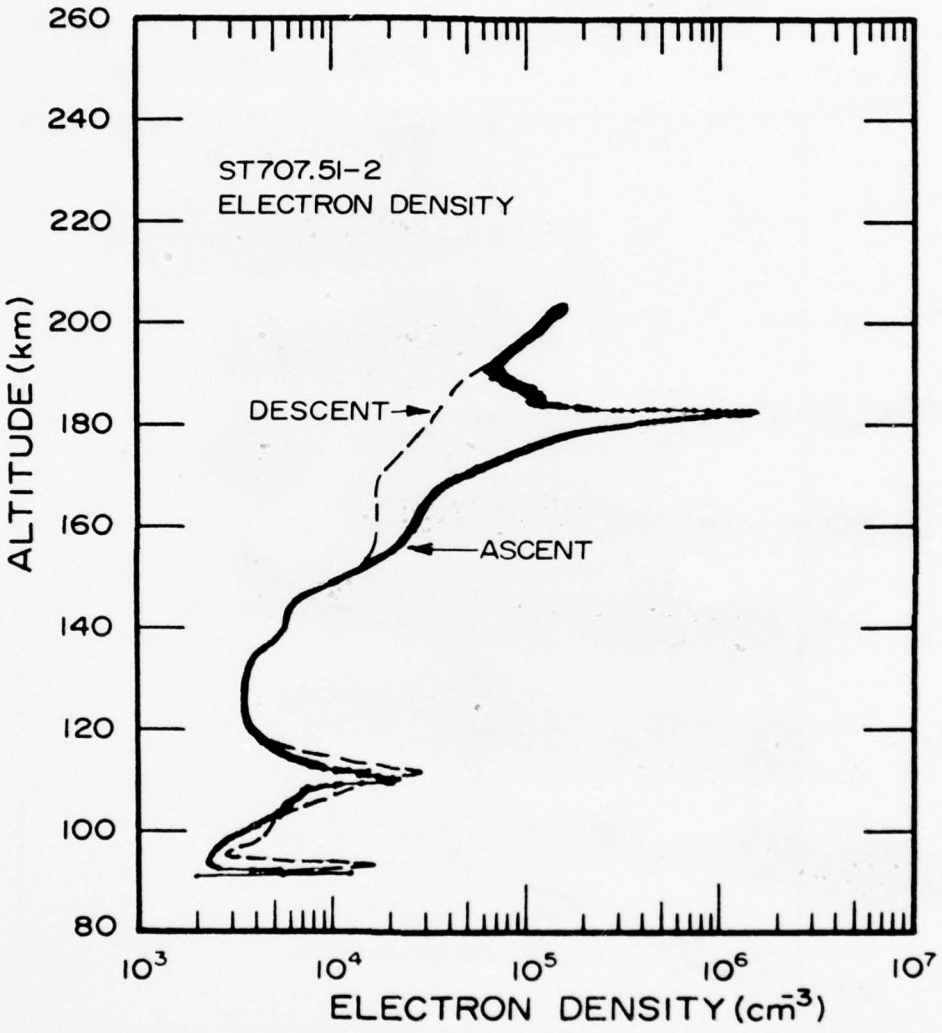

Figure 5.2. Electron density profile from probe flight ST707.51-2 on event Dianne (R+34 min). The dashed line shows the undisturbed F-region.

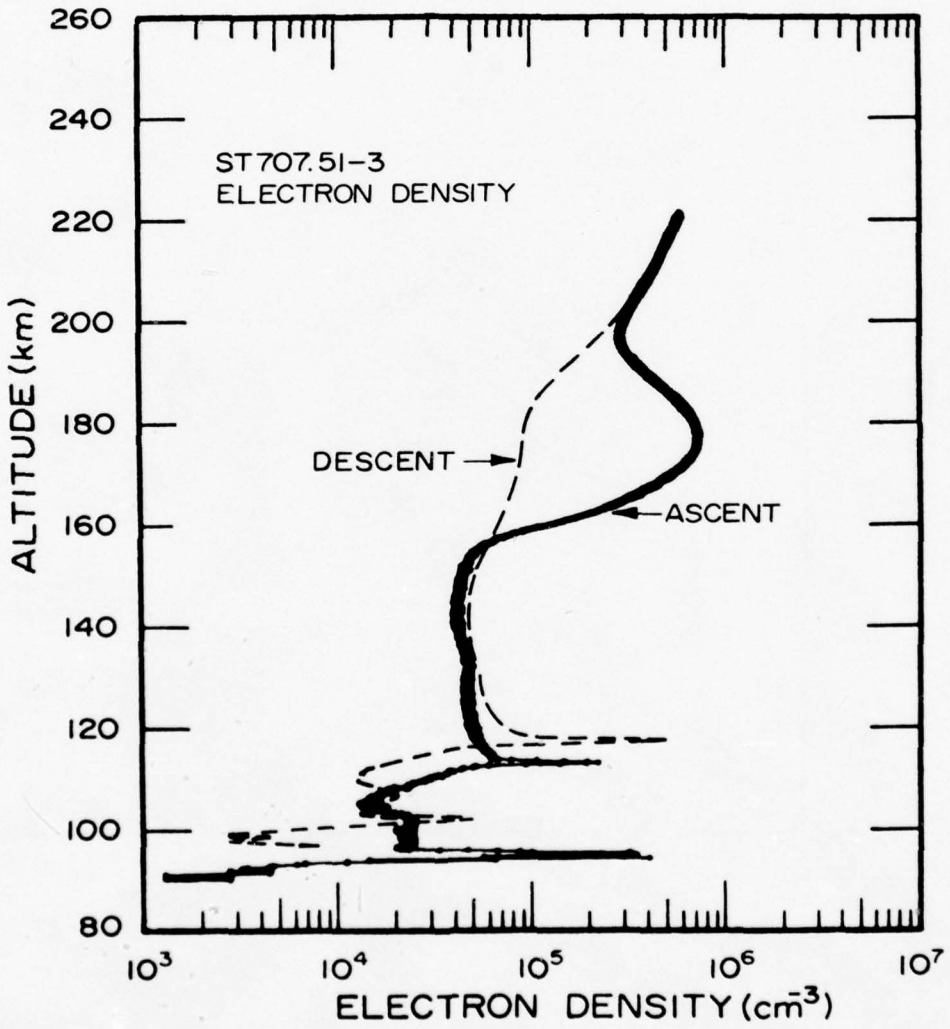

Figure 5.3. Electron density profile from probe flight ST707.51-3 on event Esther (R+28 min). The dashed line shows the undisturbed F-region.

structures of evidence of cloud striations. (The sharp peaks in the E-region are sporadic E-layers not associated with the barium release.) The layer associated with the ion cloud has a peak electron density of $7 \times 10^5 cm^{-3}$ at 177 km with a width (half amplitude) of 24 km. At the peak of the layer the density is enhanced over the ambient (determined by rocket descent) of nearly an order of magnitude. For comparison with the ion cloud formation, the rocket trajectory is superimposed upon the electron density contours measured by the ground-based radar in Figure 5.4 (courtesy SRI, Victor Gonzalez).

Rocket ST707.51-4
(Esther R+46 min)

The second probe rocket (ST707.51-4) flown into the barium cloud Esther at release plus 46 minutes penetrated the ion cloud and produced an electron density profile, Figure 5.5, that showed large scale structures in the 163-178 km region imbedded in a general layer similar to the layer probed by rocket ST707.51-3 (Figure 5.4). The observed layer has moved down from the earlier 177 km height to being centered at about 170 km. The peak value of electron density at 173 km of $5 \times 10^6 cm^{-3}$ shows an enhancement of about two orders magnitude over the normal ionosphere.

The entry of the rocket probe into the striated cloud region is consistent with the cloud geometry as determined from electron density contours furnished by SRI from the ground-based radar returns (courtesy Victor Gonzalez) (due to the ambient light level, no optical images of cloud and striations were possible). Figure 5.6 shows this cloud geometry, the rocket trajectory and the region of expected striations from a simple barium cloud model (see Section 7). An expanded version of the electron density structure as the probe penetrated the striated region is shown in the time plot of Figure 5.7. This plot shows the electron density from T+140 to T+160 sec of probe rocket flight time. This includes all of the striations penetrated by the probe in the altitude region between 163 and 178 km. For discussion, the striation fingers have been numbered. The features have varying widths (half amplitude) from 0.17 sec (feature 9) to 2.45 sec on feature 7. Note how some of the fingers, notably 3 and 6, have very fast

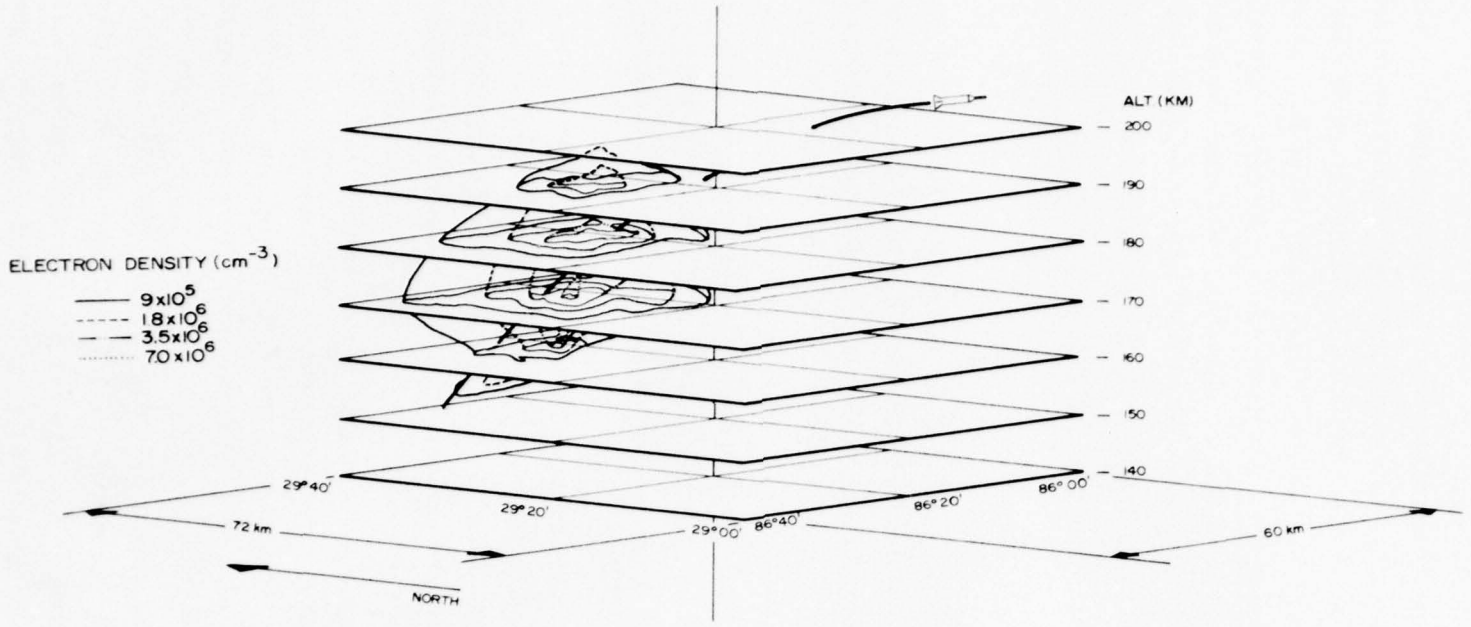

BARIUM EVENT ESTHER
PROBE ST707.51-3

Figure 5.4. Representation of ion cloud geometry at time of rocket probe ST707.51-3 in terms of electron density contours at various atltitudes from SRI radar data (from Gonzalez).

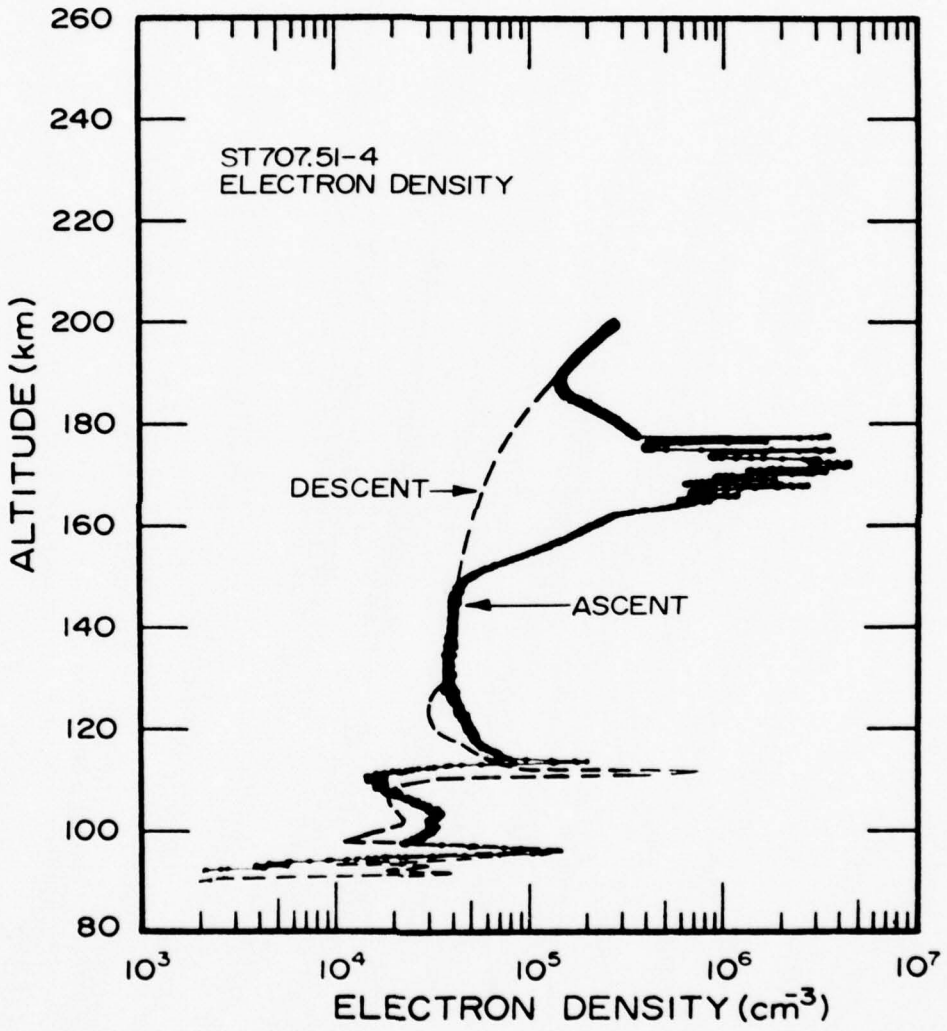

Figure 5.5. Electron density profile from probe flight ST707.51-4 on event Esther (R+46 min). The dashed line shows undisturbed F-region.

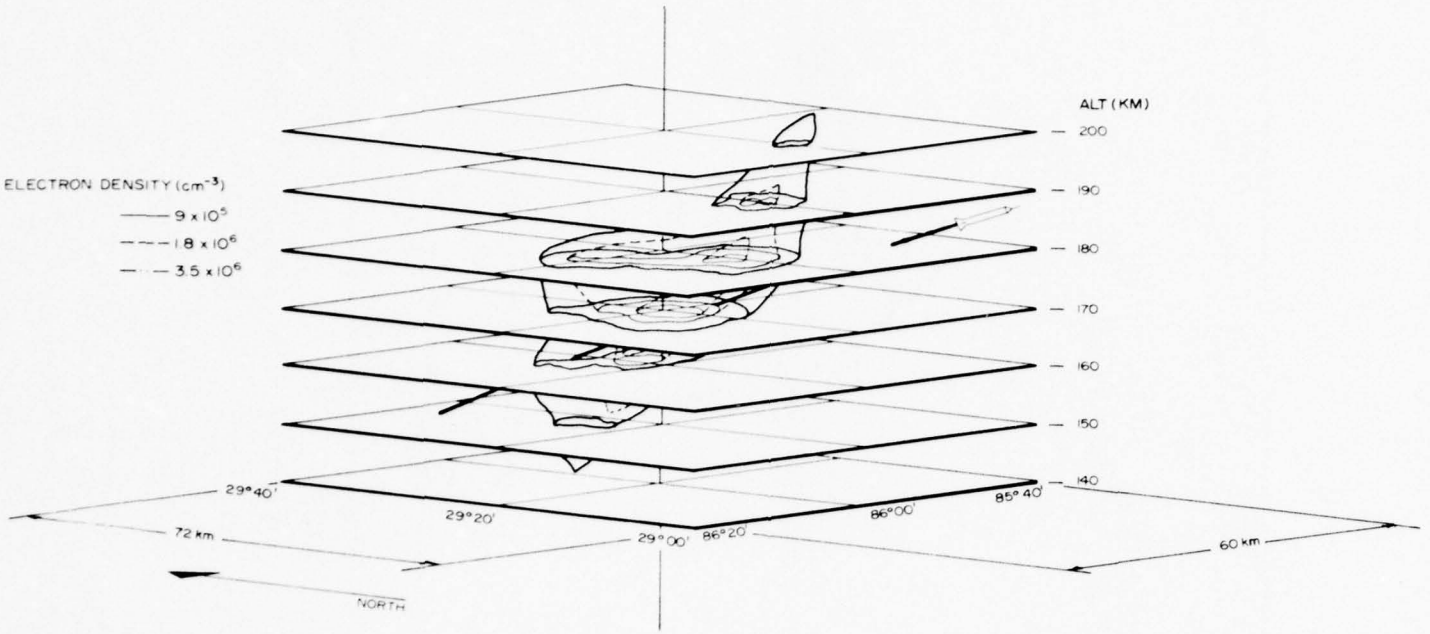

Figure 5.6. Representation of ion cloud geometry at time of rocket probe ST707.51-4 in terms of electron density contours at various altitudes from SRI radar data (from Gonzalez).

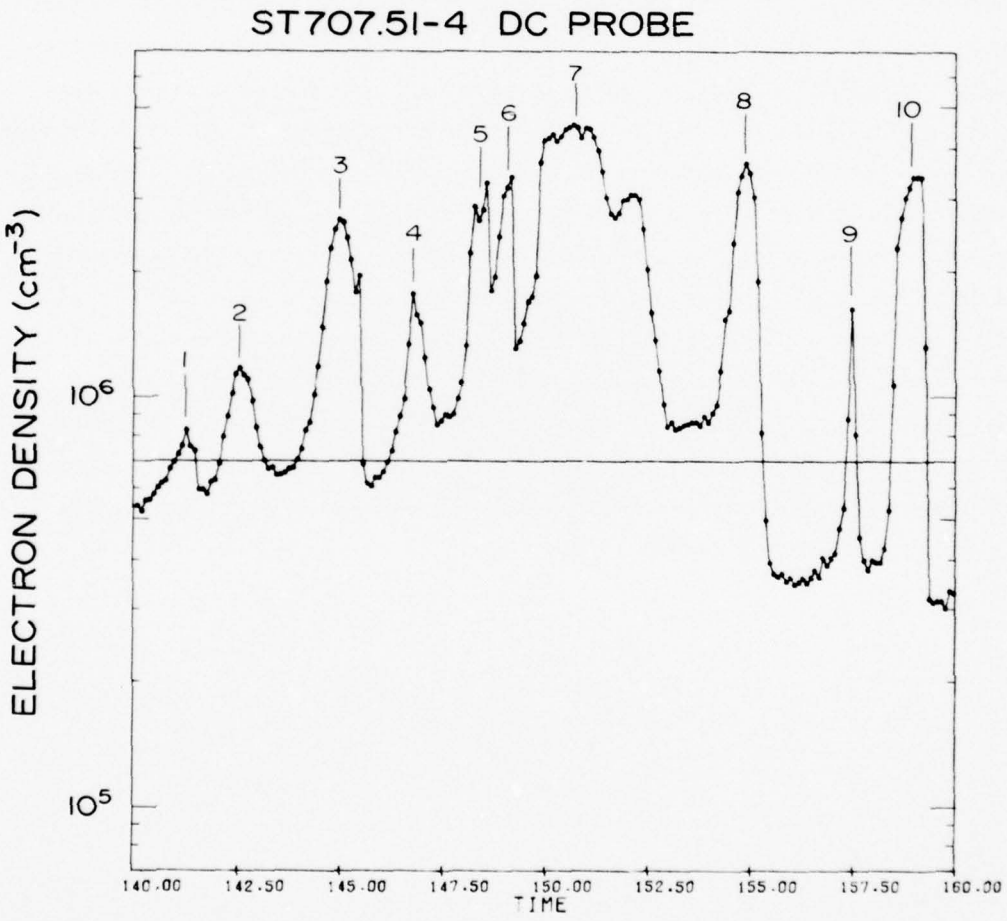

Figure 5.7. Region of electron density striations measured from T+140 to 160 seconds (163-178 km) on probe flight ST707.51-4 (Esther R+46 min). The density striations are numbered to aid discussion.

fall times (about 20 milliseconds). Figures 5.8 and 5.9 show a further magnification of portions of the striated region to facilitate a better visualization of the structure shapes.

Relating the observed variations to spatial feature geometry is not simple since the observations represent a single path cut through the spatial structure. The observations of the striation features (fingers) are summarized in Table 5.1. As a first attempt to relate the observations to spatial structure, the dimensions of the features across magnetic field lines is given bu utilizing the component of the rocket velocity perpendicular to the terrestrial magnetic field (800 m/sec). The total rocket velocity at this time is about 1310 m/sec so all dimensions would be about a factor of 1.6 larger as measured by actual rocket probe cut through the structures along the flight path. If the velocity normal to the $\bar{V} - \bar{E} \times B/B^2$ direction (345 m/sec) (see discussion of section 7) were used, the features would be 40% of those given in the table. The peak density (feature 7) of $4.7 \times 10^6 cm^{-3}$ is a factor of 6 larger than the valley following it. The density falls after the last structure (feature 10) from a value of $2.5 \times 10^6 cm^{-3}$ over an order of magnitude in about 30 m travel normal to B.

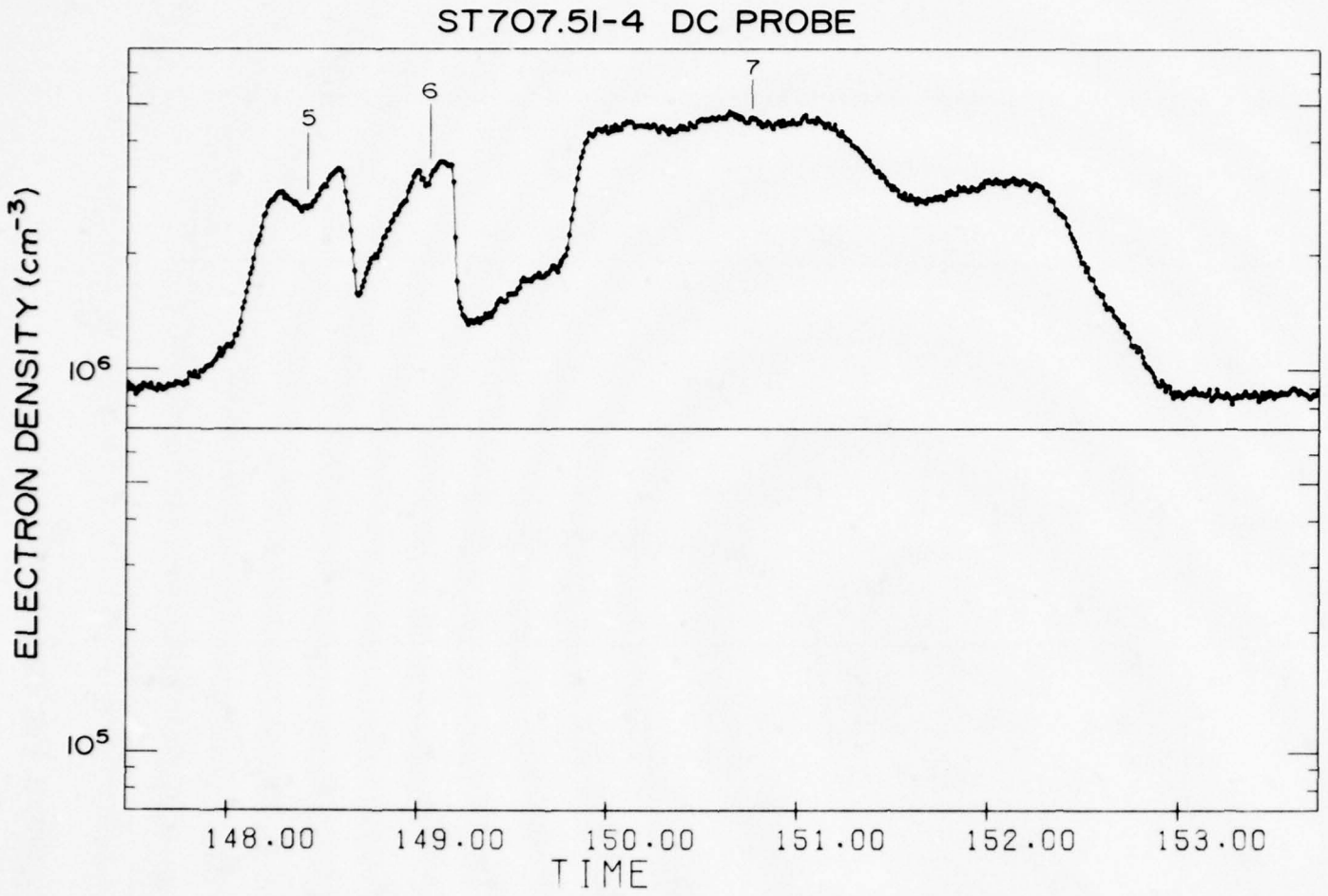

Figure 5.8. Magnification of electron density striations measured on ST707.51-4 showing features 5, 6, and 7.

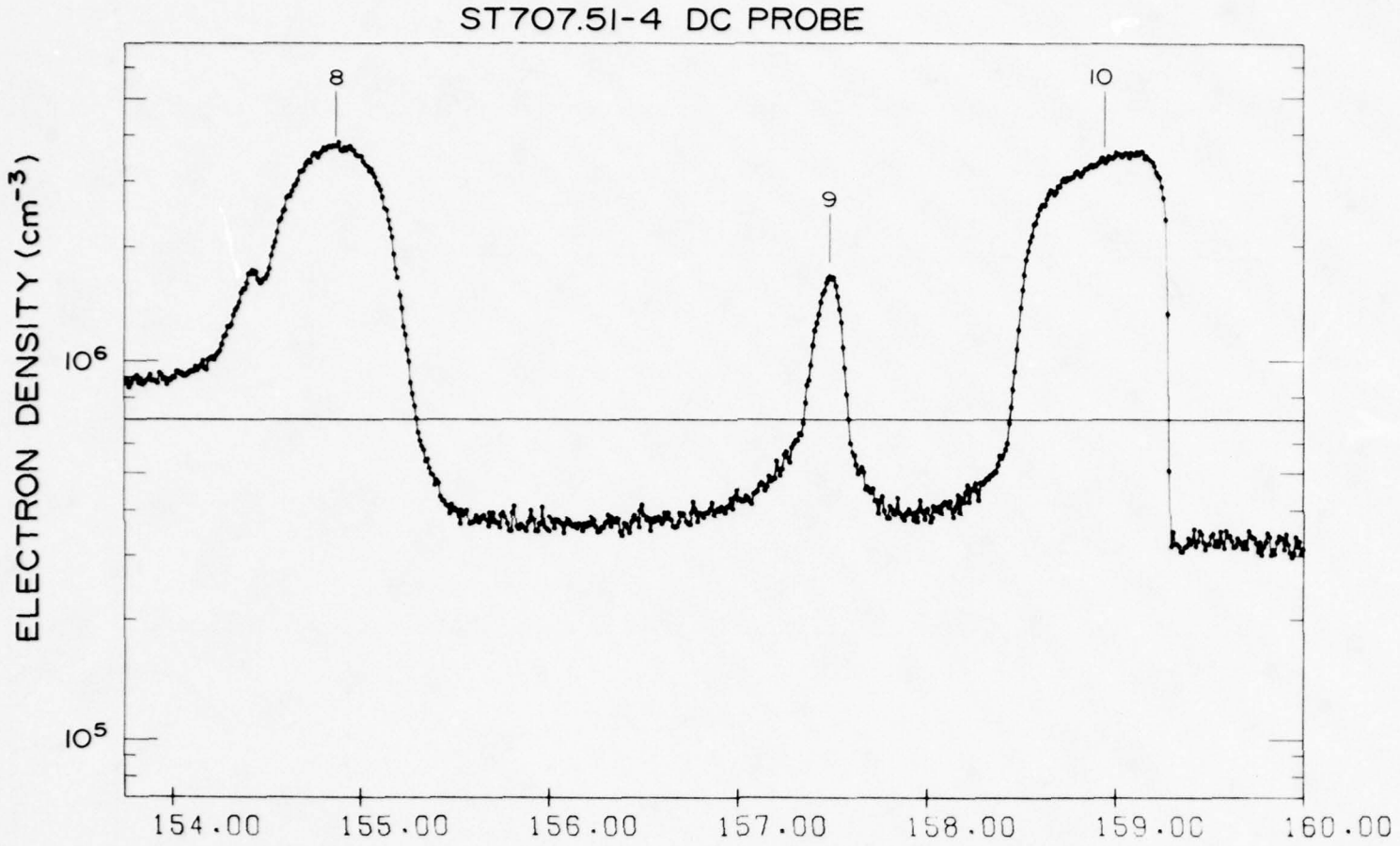

Figure 5.9. Magnification of electron density striations measured on ST707.51-4 showing features 8, 9, and 10.

TABLE 5.1

SUMMARY OF STRIATION FEATURES
(ST707.51-4)

Feature	Peak Time(Sec)	N_e (cm^{-3} x 10^6)			Width		$\frac{i}{e}$ rise		$\frac{i}{e}$ fall	
		Peak	Valley	Following	Sec	Meters ($\perp$B)	Sec	Meters ($\perp$B)	Sec	Meters ($\perp$B)
1	141.3	0.82	0.56		0.63	504	1.27	1016	0.42	336
2	142.6	1.2	0.65		0.65	520	0.84	672	0.62	496
3	145.0	2.7	0.61		0.86	688	0.37	296	0.02	16
4	146.8	1.9	0.88		0.40	320	0.12	96	0.11	88
5	148.6	3.4	1.6		0.48	384	0.18	144	0.10	80
6	149.1	3.5	1.3		0.34	272	0.38	304	0.02	24
7	150.6	4.7	0.84		2.45	1960	0.13	104	0.35	280
8	154.9	3.7	0.37		0.62	496	0.39	312	0.12	96
9	157.5	1.7	0.38		0.17	136	0.11	88	0.07	56
10	159.1	3.5	0.33		0.73	584	0.08	64	0.02	16

Rocket ST707.51-5
(Fern, R+42 min)

Probe ST707.51-5 penetrated barium cloud Fern at 42 minutes after release giving the electron density profile of Figure 5.10. The probe entered the enhanced region due to the cloud at 130 km indicating the effects of the cloud extended well down into the E-region. The enhanced region extended on the high side to over 200 km. The main electron density layer showed a broad peak of $1.3 \times 10^6 \, cm^{-3}$ at about 150 km and showed a relatively smooth profile up to about 170 km when structures appeared giving evidence of passing through a striated region of the cloud. This region of striations persists until the electron density appears to return to the normal F-region values at about 210 km.

The region of striations are shown in the time plot of Figure 5.11 to allow a better visualization of the structure of the striations. An analysis of the spatial structure of this region is given in section 7.

Rocket ST707.51-6
(Fern R+80 min)

No profiles are presented for probe ST707.51-6 since the electron density measurements were of limited usefulness. The enhanced region of electron density associated with the ion cloud was observed and extended over a large altitude range from about 112 to over 200 km.

Table 5.2 is a summary of the STRESS probe results.

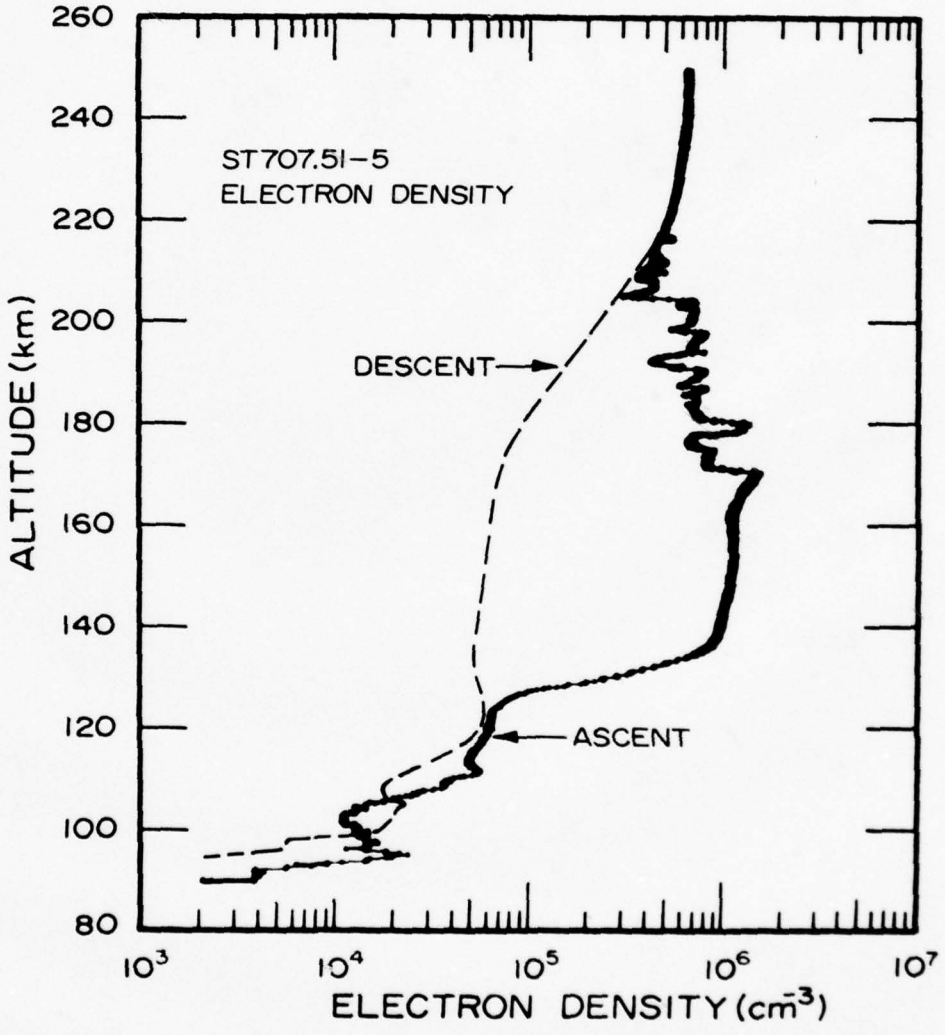

5.10. Electron density profile from probe flight ST707.51-5 on event Fern (R+42 min). The dashed line shows the undisturbed F-region.

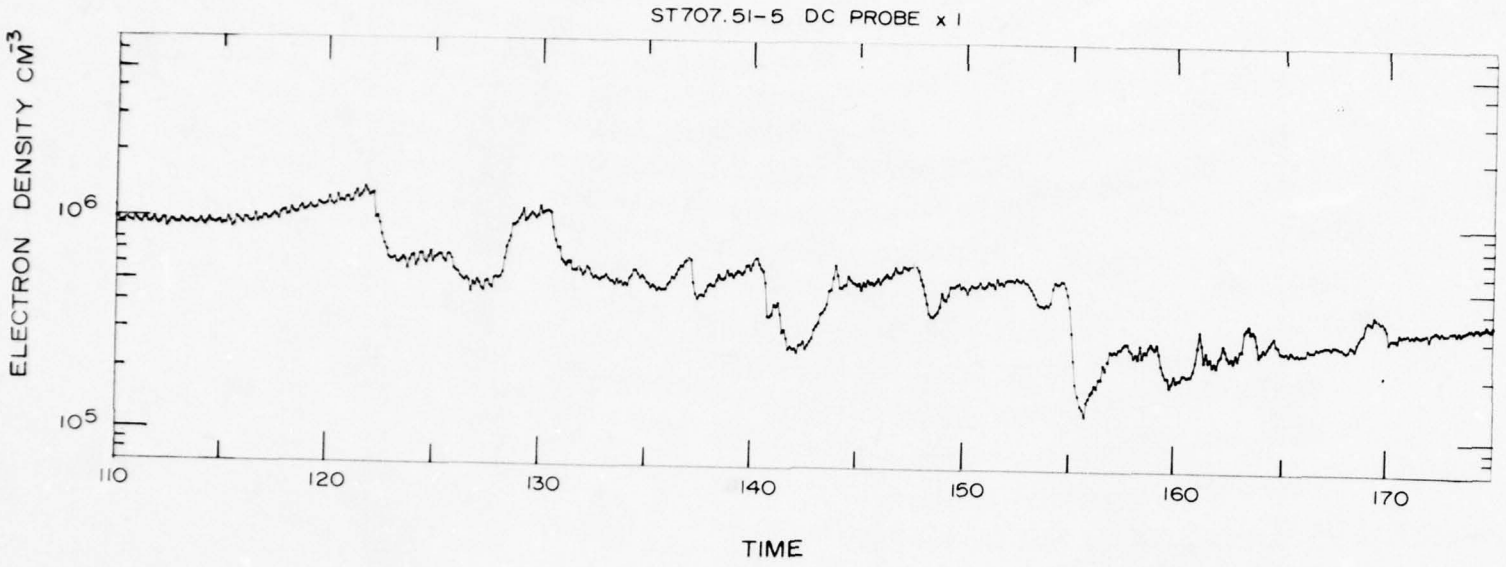

Figure 5.11. Region of electron density striations measured from 170 to 210 km on probe flight ST707.51-5 (Fern R+42 min).

TABLE 5.2

SUMMARY OF STRESS PROBE RESULTS

Event (time from release)	Probe Rocket No.	Summary of Electron Density Cloud Traversal	Ne_{max} x $10^6 cm^{-3}$ @ (km)		Seconds
Dianne (R+15 min)	51-1	Smooth layer (∿10 km)	1.4	(162)	130
Dianne (R+34 min)	51-2	One sharp finger (∿1.5 km) imbedded in layer	1.4	(182)	162
Esther (R+28 min)	51-3	Smooth layer (∿24 km)	0.7	(177)	141
Esther (R+46 min)	51-4	Ten striation fingers imbedded in layer	5	(173)	153
Fern (R+42 min)	51-5	Enhanced region over large altitude range (130-210 km) striations from 170 to 210 km	1.3	(171)	122
Fern (R+80 min)	51-6	Slight enhanced region over large altitude range (112-200 km)			

6. SPECTRAL ANALYSIS OF THE ELECTRON DENSITY VARIATIONS

The concentration in this section is on the examination and comparison of the spectral analysis of the variations of the electron density results which were presented as height profiles in the previous section. These data are presented in two subsections: Short Wavelength Characteristics (less than 50 meters) and Long Wavelength Characteristics (greater than 50 meters). The DC probe results from xl gain range (IRIG channel 20), which had sufficient bandwidth to allow 10 KHz digitization (for the Short Wavelength Studies), were utilized. First, for the Short Wavelength Characteristics, Fourier transforms of the detrended electron density data were obtained every 0.8192 sec. They were spectrally smoothed by averaging each successive 5 spectra, and these resulting spectra are presented in this section. The irregularity amplitude ($\Delta N/N$) spectra are shown in the frequency (time) domain in order to identify non-atmospheric induced characteristics (e.g. rocket spin effects; a 60 hz ground station pick up). Spatial scales are added to the figures, when appropriate, which are obtained by utilizing the rocket velocity perpendicular to the magnetic field (of course, another rocket velocity e.g. that parallel to the magnetic field, could have been used.) Spectra are shown in detail for the two rockets that penetrated the striated barium clouds - rockets ST707.51-4 and ST707.51-5. A few spectra from rocket ST707.51-3 which preceded rocket ST707.51-4 through the same barium cloud (Esther) but with no evidence of striations at that time are shown for comparison purposes. With respect to the Long Wavelength Characteristics, preliminary calculations have shown that only the rockets that penetrated the striated barium regions exhibit spectral distributions that increase in amplitude at these wavelengths (and only in the striated regions). For rocket ST707.51-4 (Esther), the striated region is from 140 to 160 sec rocket flight time, corresponding to rocket altitude from 165 to 178 km. For rocket ST707.51-5 (Fern), the striated region is from 120 to 160 sec rocket flight time, corresponding to rocket altitude 169 to 210 km. These long wavelength data are discussed briefly since the next section (7) discusses the results in detail.

Short Wavelength Characteristics

Rocket ST707.51-4

This rocket entered the barium cloud (Esther) at 125 sec (150 km), entered the striated region at 140 sec (165 km), departed this region at 160 sec (178 km) and was out of the cloud into the normal atmosphere at 180 sec (188 km). The first series of spectra examine the characteristics of the unstriated barium cloud from the time of rocket penetration to the striated region (125-140 sec) using the spectral smoothed results (average of 5 spectra, total interval about 4.1 sec). The spectra prior to 125 sec all look alike and are the same as those obtained after the rocket leaves the barium cloud. This spectrum is shown in frequency because it identifies so clearly the effect of the spin of the rocket on the electron density measurements (fundamental at 6.0 Hz plus upper harmonics) and a ground station pickup superimposed on the data (60 Hz plus odd harmonics most visible). These both can be, of course, eliminated by filtering but are useful in the following discussions as reference points since not only is the irregularity structure of the electron density changing (ΔN), but also the electron density (N). The next spectrum (Figure 6.2) at 128.24 sec (from now on only the end time of the sample interval will be identified) when the rocket is within the unstriated barium cloud shows distinct changes from the previous one. First, with exception of the interval from about 700 Hz to 10^3 Hz, the whole spectrum has moved down in level as expected due to the increased electron density (N) in this interval. However, not expected is the increase in amplitude in the interval 700 to 10^3 Hz (lower scale) which corresponds to scale sizes of approximately 1.1 to 0.8 meters as measured across the terrestrial magnetic field (upper scale). The rocket velocity perpendicular to the magnetic field is about 760 m/sec in this time interval. The next figure (Figure 6.3) at 132.14 sec, shows a distinct increase at about 1.1 meters (by about a factor of two) compared to the previous figure. Note also the relative heights of the peaks in both figures compared to the "300 Hz reference spike" as well as relative to the constant lowest level at the highest frequencies/lowest wavelength

both of which indicate the growth of the peak. More subtle is the increase in power in the wavelengths from about 10 meters to 1.5 meters. The next two figures (Figure 6.4 at 136.4 sec and Figure 6.5 at 140.5 sec) show this increase in the interval 10 to 1.5 meters more distinctly as well as the disappearance of the peak and the increase in the electron density (N). Note throughout Figures 6.1-6.5, the lower frequencies (wavelengths greater than 10 meters) have not changed and that at wavelengths less than about 0.35 meters the level is constant. The concentration in this section is an examination and comparison of the data at the short wavelengths but it will be pointed out, when appropriate, the changes occurring at the longer wavelengths (50 to 500 meters) since in this section (compared to the next - Long Wavelength Characteristics) shorter time (and spatial) intervals are examined.

The next series of spectra, Figures 6.6-6.10 cover the striated region of the cloud, from 140.5 to 161 sec; 5 spectra (each averaging 5 spectra) each in the time interval of 4.1 sec (see Figure 5.7 of the previous section which shows the striated region in the electron density profile). The first spectrum, Figure 6.6, covers the time interval 140.5 to 144.6 sec, the beginning of the time when the rocket enters the striated region through the first two "fingers" (peaks in N_e). Compared to the previous spectra, immediately apparent is the increase in irregularity amplitude at the higher wavelengths (from about 10 to 800 meters). The Long Wavelength Characteristics in the next section show this increase over the whole striated region, not just, as in this case, at the beginning. This spectrum does confirm, however, that the longer wavelengths are only increased in irregularity amplitude or power in the striated region as compared to the unstriated barium cloud. (Figure 6.10 the last spectrum in the striated region compared to Figure 6.11 the first spectrum back in the barium cloud shows this also.) The next few spectra are all pretty much the same as Figure 6.6 except that Figure 6.7 shows a steeper slope than the other lower altitude spectra at the higher wavelengths (>10 meters) and Figure 6.8 shows a higher slope at the very short wavelengths (<1 meter) as well as a distinct increase in irregularity amplitude between 1.6 and 0.8 meters. Figure 6.7 covers the interval

where the rocket goes through the most "fingers" (finger Nos. 5 & 6) which have the sharpest slopes (see Figures 5.7 and 5.8 of the last section showing the striated region in detail). Figure 6.8 covers the interval where the electron density has its highest value (finger no. 7) and for a relatively longer period (again see Figures 5.7 and 5.8). It is also interesting to note that Figure 6.9 which only covers one "finger" (finger no. 8) is very similar to the others which cover two or more.

The next series of spectra Figures 6.11-6.14 cover the time interval 161 to 177.4 sec when the rocket is back in the unstriated barium cloud until the rocket leaves the cloud. First, Figure 6.11 compared with Figure 6.10 shows (1) the decrease in irregularity amplitude in the longer wavelengths (>50 meters) to a slope like that before entering the striated structure (2) a decrease in the region 10 meters to about 1 meter (3) an increase and peaking at about 1 meter and (4) the lowest wavelength spectra about the same. Figure 6.12 continues this trend with the peak first decreasing in amplitude towards the longer wavelength side giving the appearance of a shift of the peak to shorter wavelengths. Figure 6.13 continues to show the decrease out to the longer wavelengths until by Figure 6.14 (the last spectrum in the barium cloud) the spectrum looks like Figure 6.1. Note also how Figures 6.11 & 6.12 compare to Figure 6.3 and Figure 6.13 compares to Figure 6.2. In other words the phenomenology before entering the striated region looks the same as that after leaving the striated region.

Rocket ST707.51-5

The electron density results from rocket ST707.51-5 (Fern) are obviously different from rocket ST707.51-4 as shown in the previous section, but what about the short wave irregularities amplitude characteristics? The discussion will be in two parts (1) the unstriated barium cloud from 90 to 120 sec (128 to 169 km) and (2) the striated region 120 to 160 sec (169 to 210 km). The spectra up until barium cloud entrance are pretty much the same and look like the spectra in the undisturbed atmosphere above 218 km - and like the spectra from rocket ST707.51-4 outside the barium cloud. The first distinct change is shown in Figure 6.15 for the

time interval 99.6 to 103.7 sec. A sharp peak is formed at 1260 Hz on the frequency scale which is 0.25 meter in wavelength (rocket velocity perpendicular to the magnetic field at this time 300 meters/sec). Note that for rocket ST707.51-4 (Figure 6.2) the peak occurred at 1 meter and also different is the fact that the frequency of the peak was near 750 Hz with the rocket velocity perpendicular to the magnetic field 760 meters/sec. The next series of figures until rocket entrance into the striated region Figures 6.16-6.19 show the growth in power in the region from about 10 meters to about 0.2 meters.

The spectra in the striated region of the cloud from 120 to 136.5 sec (157 km to about 175 km) are all about the same and Figure 6.20 is representative of the irregularity amplitude spectrum for this region. This spectrum compared with one from rocket ST707.51-4 in the striated region, e.g. Figure 6.7 shows similarity for the short wavelengths. From 136.5 sec to departure from the barium cloud near 160 sec (210 km) there is a general decrease in irregularity amplitude in the spectra as shown in three representative spectra; Figure 6.21 (140.6 sec-191 km), Figure 6.22 (153 sec-203 km) and Figure 6.23 (161 sec-210 km). The latter figure is representative of the spectra obtained up to rocket apogee of 250 km. Note that rocket ST707.51-4 came out of the striated region abruptly into the background barium cloud whereas rocket ST707.51-5 went from a gradually decreasing striated region (and of course not nearly as striated as ST707.51-4) into the normal ionosphere.

In Figures 6.1-6.23 amplitude distribution of electron density irregularities ($\Delta N/N$) versus frequency (lower scale) and spatial dimension (upper scale) derived from the rocket velocity perpendicular to the terrestrial magnetic field. The spectral distributions were derived by taking a fast fourier transform (FFT) of the detrended $\Delta N/N$ results digitized at a 10 kHz rate over about 0.8 seconds and then averaging over 5 spectra for a total time of about 4 seconds for each plot. The rocket probe number and time and altitude of the end of the 4-second period of the spectra are shown on each figure.

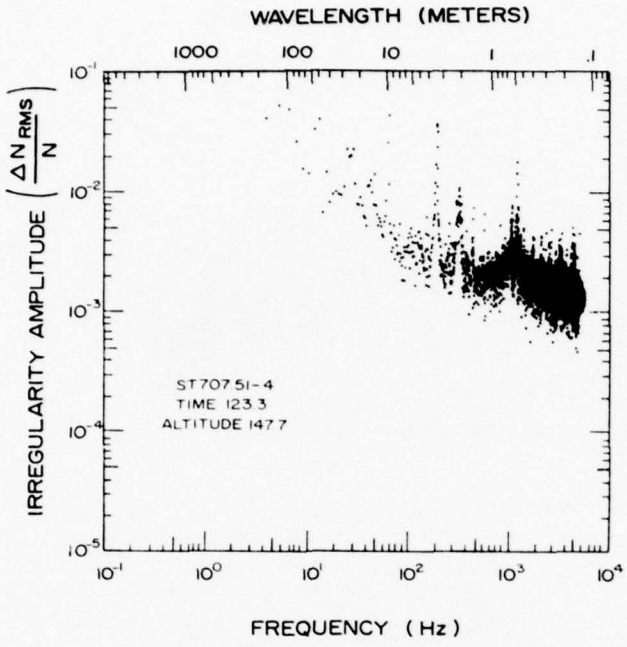

Figure 6.1

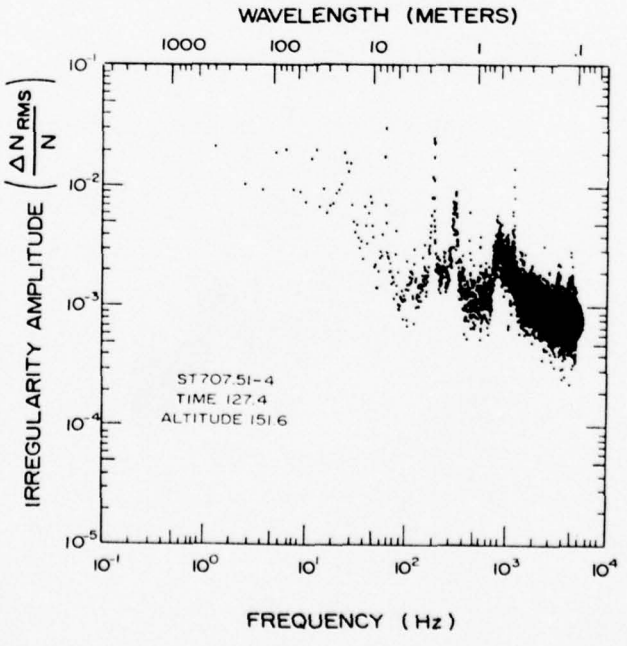

Figure 6.2

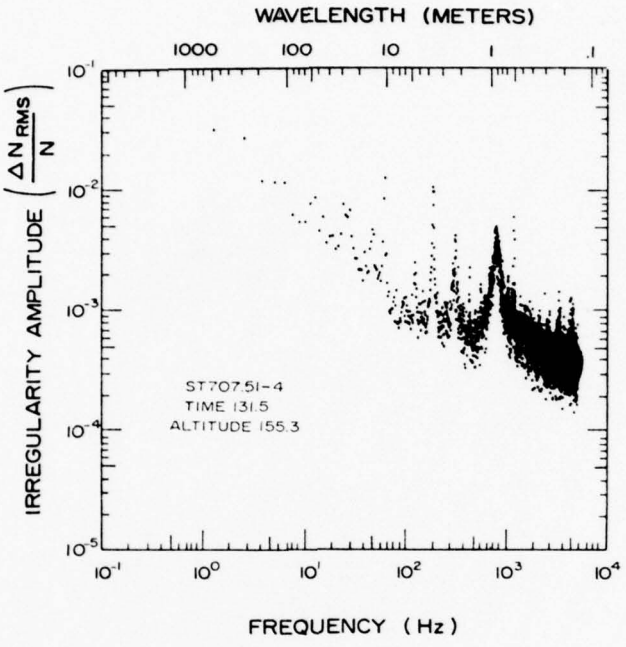

Figure 6.3

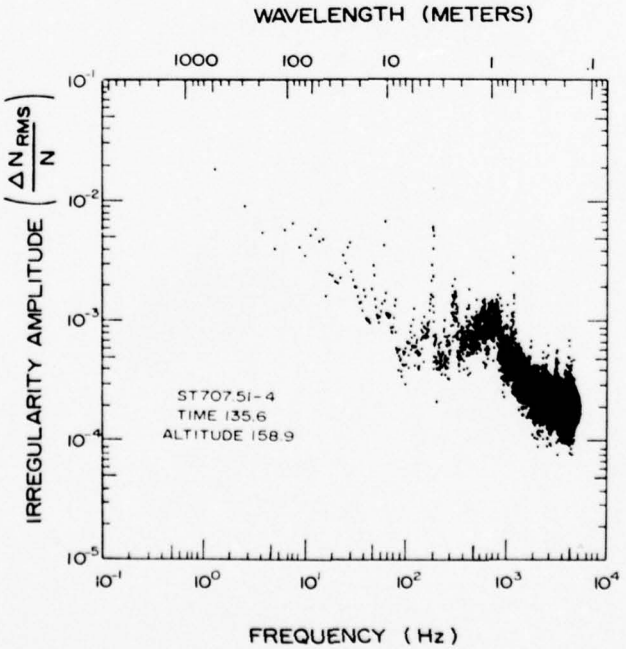

Figure 6.4

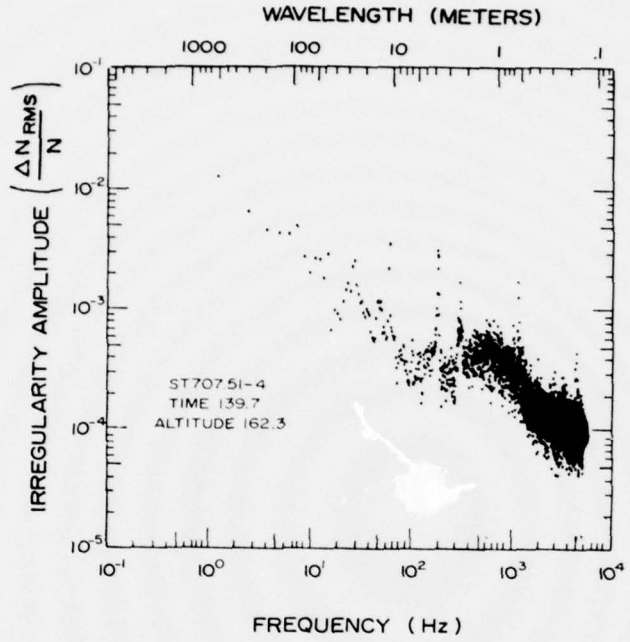

Figure 6.5

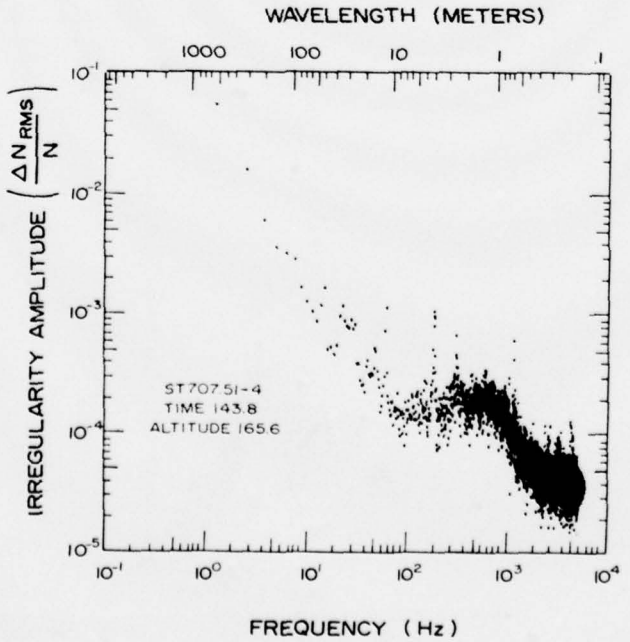

Figure 6.6

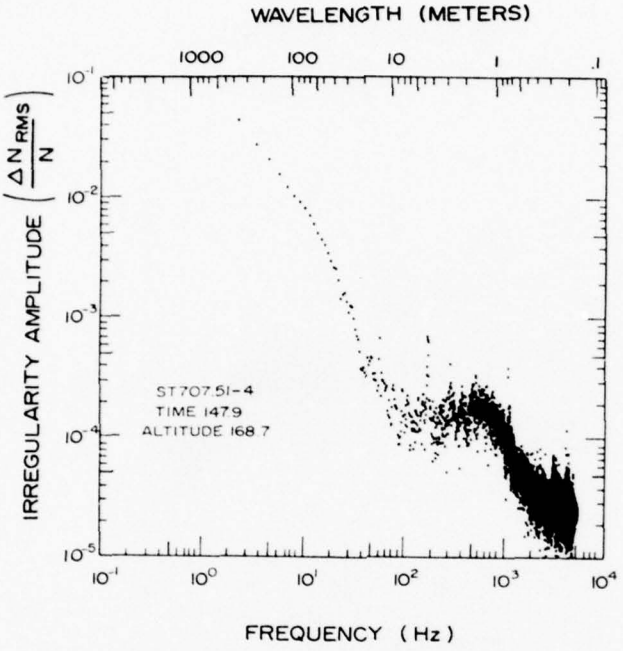

Figure 6.7

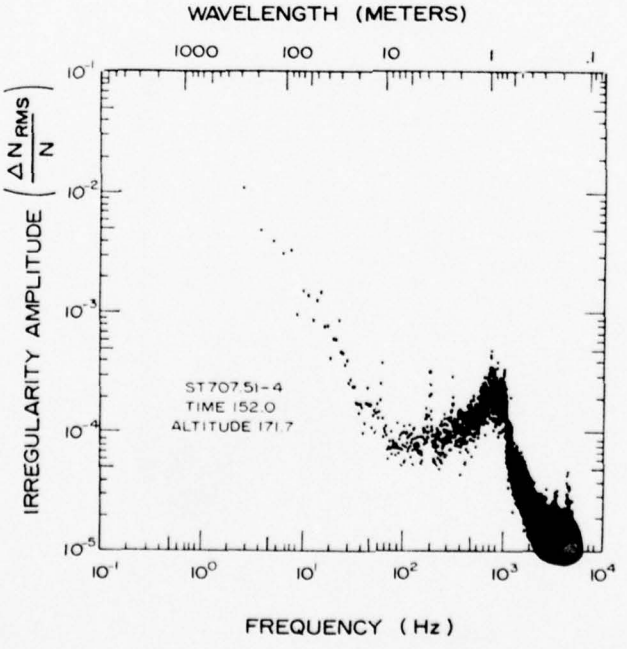

Figure 6.8

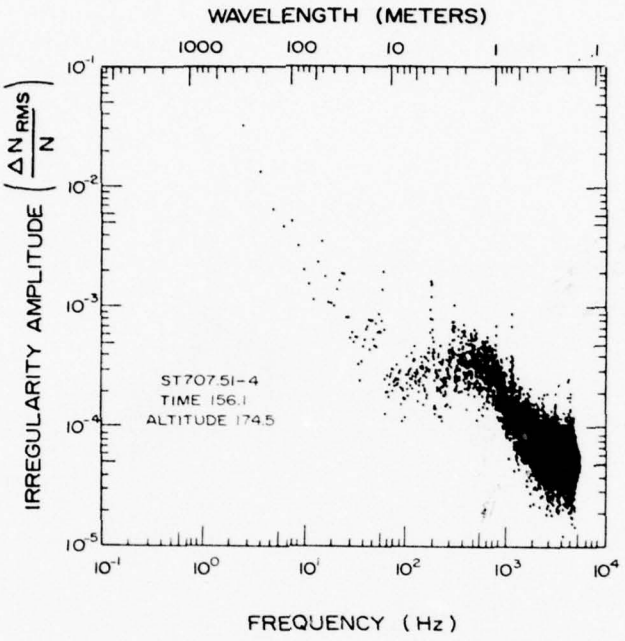

Figure 6.9

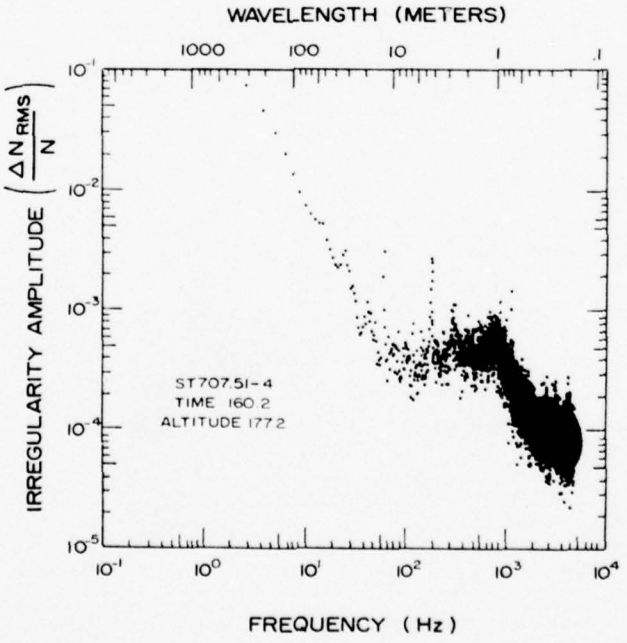

Figure 6.10

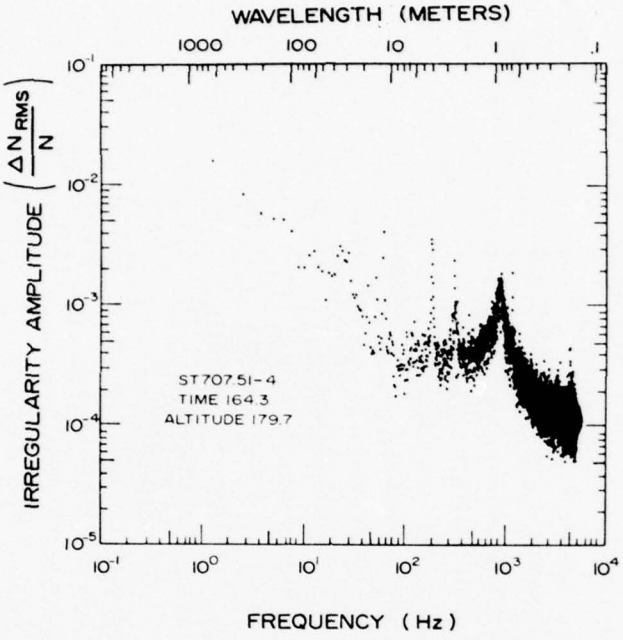

Figure 6.11

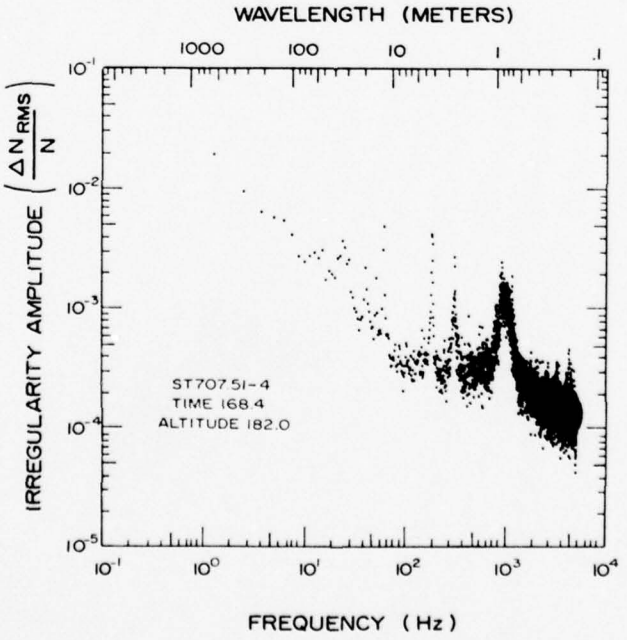

Figure 6.12

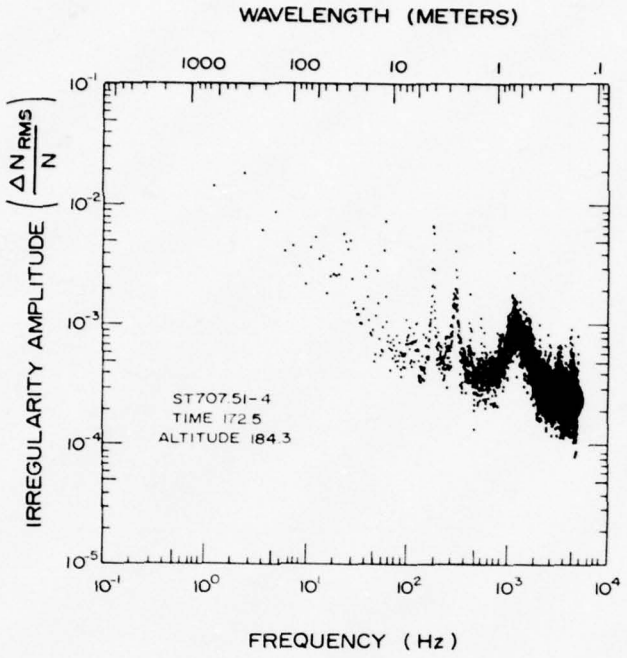

Figure 6.13

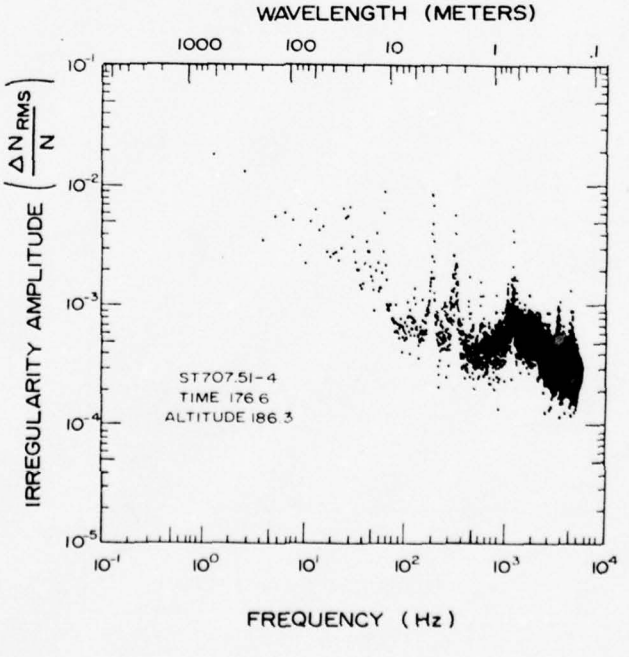

Figure 6.14

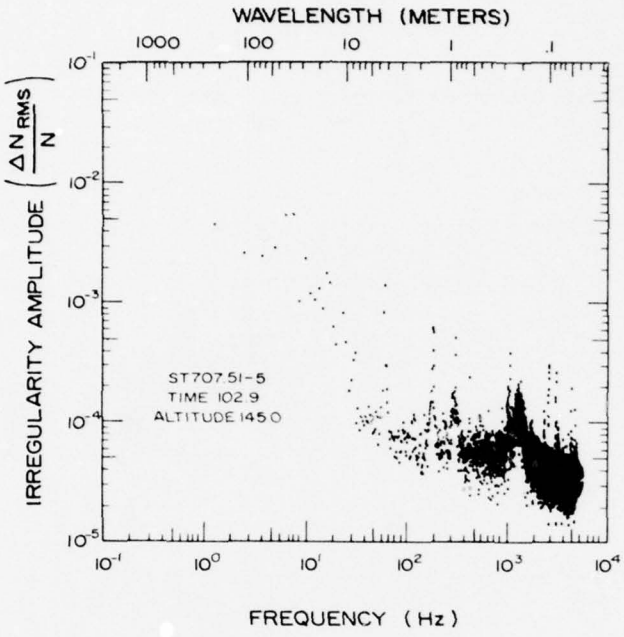

Figure 6.15

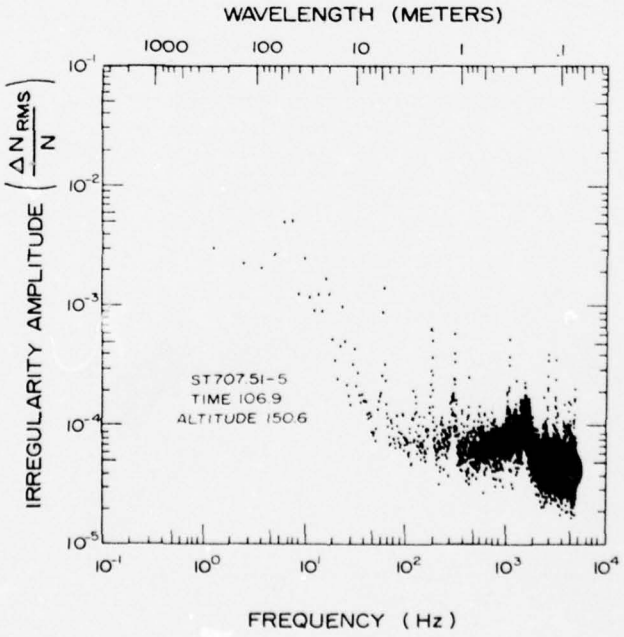

Figure 6.16

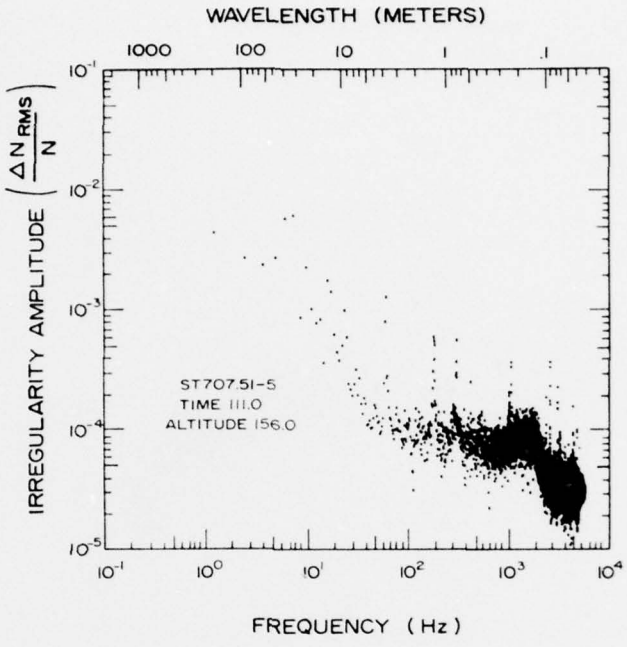

Figure 6.17

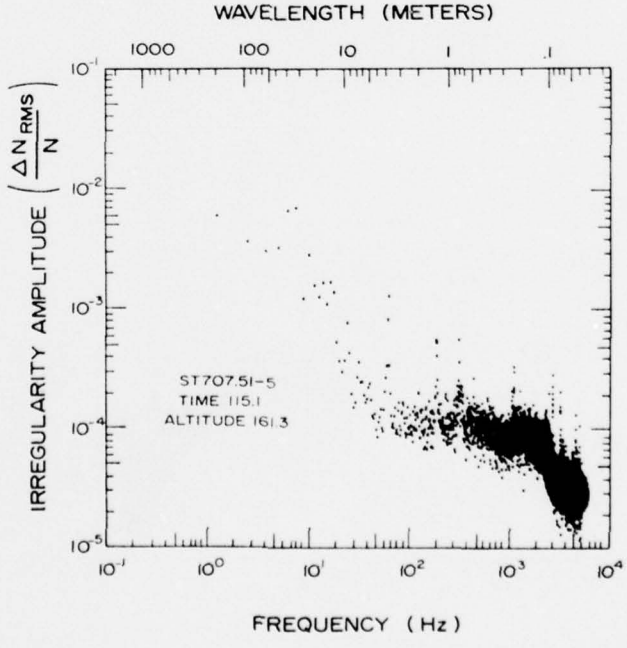

Figure 6.18

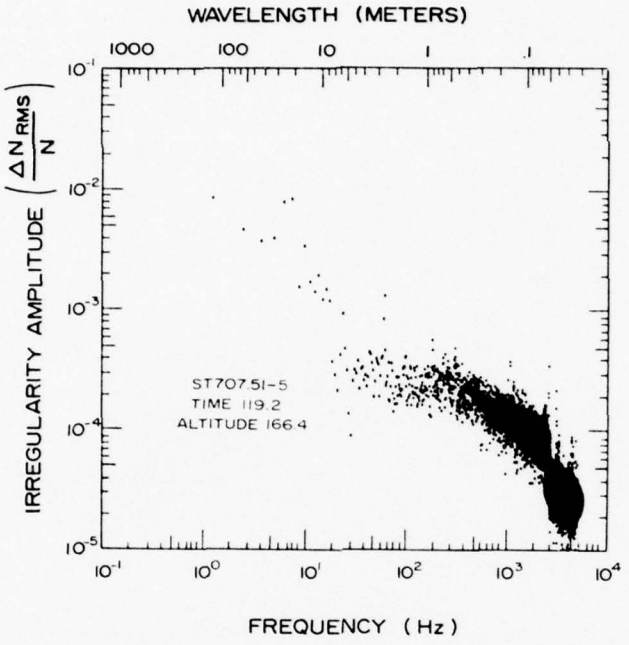

Figure 6.19

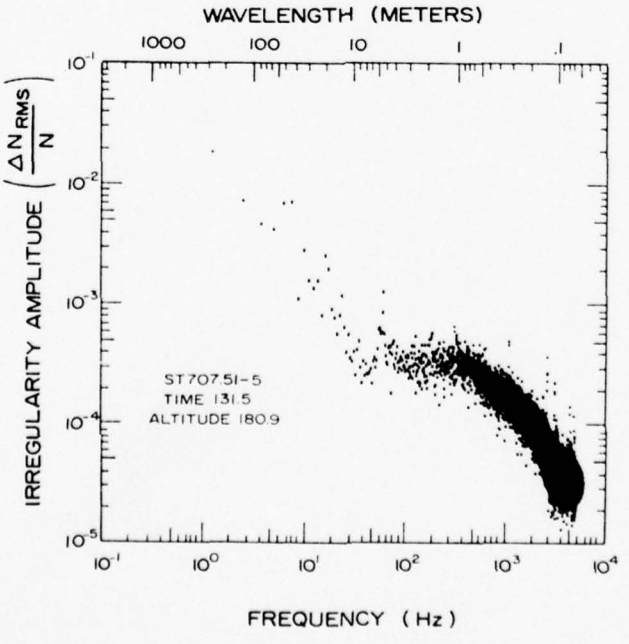

Figure 6.20

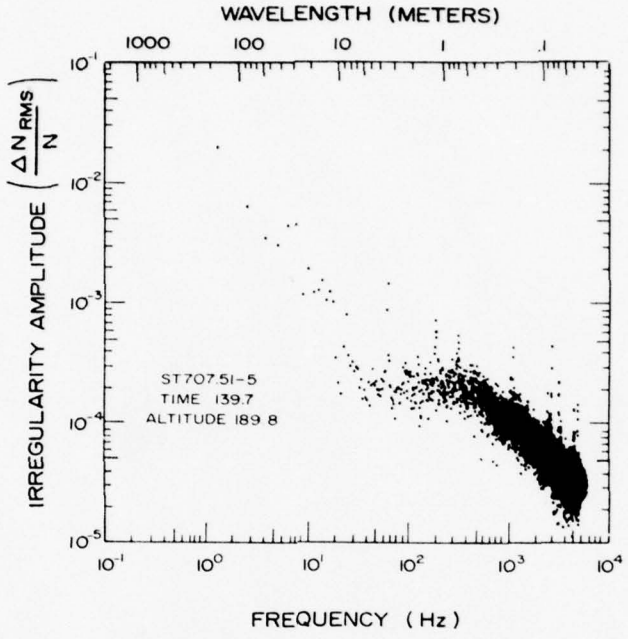

Figure 6.21

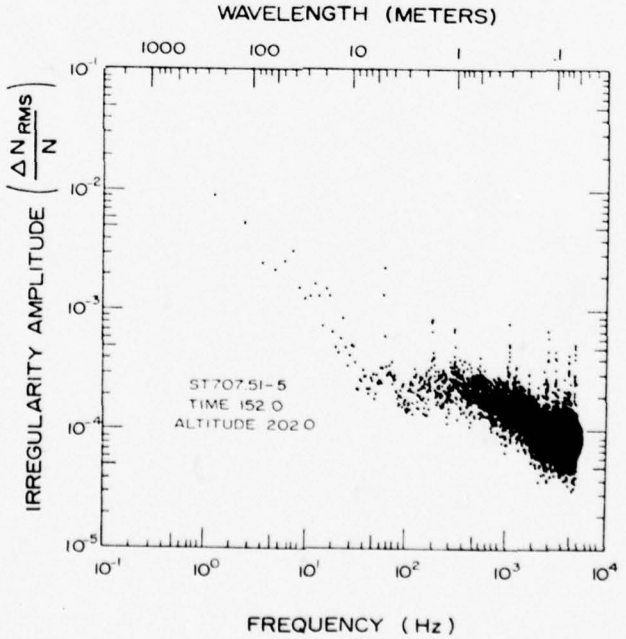

Figure 6.22

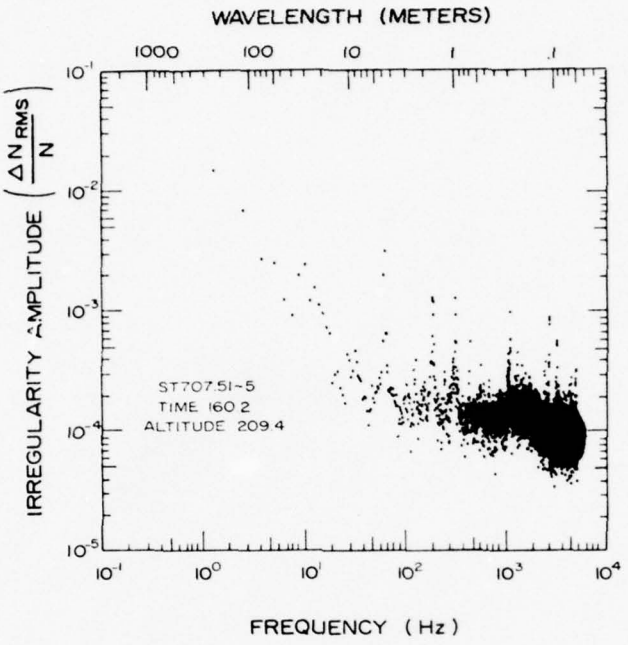
WAVELENGTH (METERS)
1000
100
10
1
.1
IRREGULARITY AMPLITUDE $\left(\frac{\Delta N_{RMS}}{N}\right)$
10^{-1}
10^{-2}
10^{-3}
10^{-4}
10^{-5}
ST707.51-5
TIME 160 2
ALTITUDE 209.4
10^{-1}
10^{0}
10^{1}
10^{2}
10^{3}
10^{4}
FREQUENCY (Hz)

Figure 6.23

Long Wavelength Characteristics

Rocket ST707.51-4

The power spectrum shown in Figure 6.24 was obtained over the time interval from 140 to 153 sec of rocket ST707.51-4 (Esther) utilizing the DC probe x1 data. These data were decimated by averaging together 16 points and detrended by fitting to a polynomial of degree 3. Note the uniform slope between .2 and 50 Hz. Figure 6.25 shows the power spectrum for rocket ST707.51-5 (Fern) in the striated region. The data were decimated by averaging together 80 points and detrended by fitting to a polynomial of degree 3. These results are very similar to Figure 6.24 with the slope not quite as steep however. The implications of the Long Wavelength Spectra are discussed in the next sections.

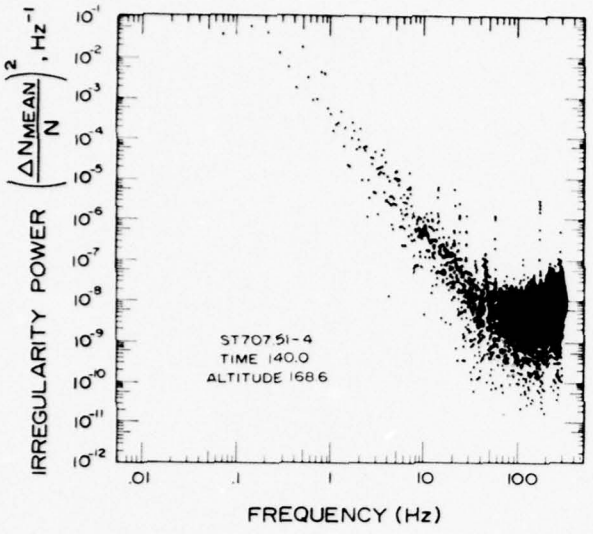

Figure 6.24. Power spectral density of electron density irregularities (long wave analysis) for rocket probe ST707.51-4 (Esther) in the region of striations.

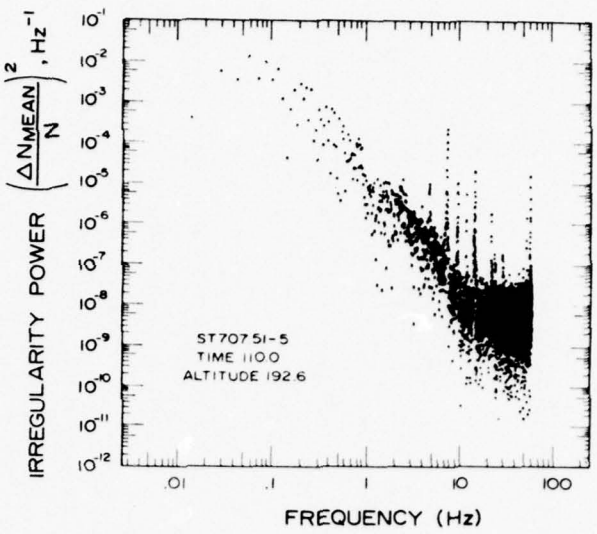

Figure 6.25. Power spectral density of electron density irregularities (long wave analysis) for rocket probe ST707.51-5 (Fern) in the region of striations.

7. COMPARISON BETWEEN THEORY AND OBSERVATION OF BARIUM CLOUD STRUCTURE

1. Location Of Large Scale Striations

In this section we relate the data to the predictions of linear and nonlinear theory for the structures which develop in large barium clouds. The basic phenomena can be understood in relation to equation 7.1 which relates the velocity $\bar{V}_\perp$ of a barium cloud perpendicular to the Earth's magnetic field $\bar{B}$ to the ambient electric field $\bar{E}$ and the neutral wind $\bar{V}_n$ (Haerendel et al., 1967)

$$\bar{V}_\perp = \frac{2}{\lambda^*+1}\frac{\bar{E}\times\bar{B}}{B^2} - \left(\frac{\lambda^*-1}{2}\right)\frac{\bar{V}_n\times\bar{B}}{B} \tag{1}$$

where

$$\lambda^* = \frac{\text{integrated cloud conductivity + integrated background conductivity}}{\text{integrated background conductivity}}$$

We have dropped a term of order ν_{in}/Ω_{in}, the collision frequency of ions divided by their gyro frequency, which is valid at the altitude of the clouds studied. In the case of a small cloud $\lambda^*\approx 1$, and the cloud moves with the perpendicular velocity $\bar{E}\times\bar{B}/B^2$. For a large cloud, λ^* can become significantly larger than 1, which is the case of interest here. Consider first the case that $\bar{V}_n=0$. Then in the center of the cloud, the total electric field is smaller than either the ambient field or the field in the surrounding cloud (an effect verified with electric field measurements during the Secede program by Schutz et al., 1974). Those parts of the cloud in the direction of the background $\bar{E}\times\bar{B}$ move away from the center, the "leading edges" while those at the opposite side catch-up to the central portion. The number density following a fluid element changes according to the convective derivative

$$\frac{DN}{Dt} = \frac{\partial n}{\partial t} + (\bar{V}\cdot\bar{\nabla})n \tag{2}$$

At long times after release no new barium ions are forming in the main part of the cloud and recombination is slow, so $\partial n/\partial t=0$. Thus the only changes in density occur where $(\bar{V}\cdot\bar{\nabla})n\neq 0$. In the backside $\bar{V}$ is parallel to $\bar{\nabla}n$ so the density increases and in the frontside they are opposite so the density decreases. The leading edges become tenious ($\lambda^*\to 1$) and approaches the $\bar{E}\times\bar{B}$ velocity of the ambient medium while the backside

becomes more dense and forms a steep gradient in density. It is this gradient in electron density which is unstable to striation development. To determine the sector of instability, one can thus draw a vector from the cloud center in the direction of $-(\bar{E}x\bar{B})$.

In the mid-latitude ionosphere one can seldom ignore the neutral wind term. However, if one transforms to a reference frame moving with velocity $\bar{V}_n$ (the direction of the wind velocity in the plane perpendicular to $\bar{B}$, then the neutral wind is zero and we can use the derivation outlined above with the electric field in the new frame given by the transformation (Jackson, 1960)

$$\bar{E}' = \bar{E} + \bar{V}_n x \bar{B} \tag{3}$$

where $\bar{E}$ and $\bar{V}_n$ are measured in the Earth's fixed frame. Note that $\bar{B}$ is unchanged in such a transformation if $\bar{V}_n << c$. The unstable sector is again in the $-(\bar{E}'x\bar{B})/B^2$ direction. We relate our measurements to Earth fixed quantities so we must substitute 7.3 into this expression:

$$\frac{-(\bar{E}' x \bar{B})}{B^2} = \frac{-(\bar{E}x\bar{B})}{B^2} - (\bar{V}_n x \bar{B})x\bar{B}/B^2 = \bar{V}_n - \bar{E}x\bar{B}/B^2 \tag{4}$$

Thus to determine the unstable region we can construct this vector if we know $\bar{V}_n$ and $\bar{E}$. Unfortunately, viewing conditions during the experiment were such that optical measurements of the wind from the neutral cloud and of $\bar{E}$ from the "leading edge" of the barium were not possible. We can thus only show consistency with the theory, but not detailed comparison. Optical observations of these quantities plus the striations made in the Secede series (Davis et al., 1974) were able to show detailed agreement and we can have confidence that our interpretation is valid.

If we know the velocity of the cloud, $V_\perp$, and the neutral wind, we can still determine the direction of the striated region without knowledge of the ambient electric field or λ^* as follows. In the neutral wind frame from equation 7.1 we know that the cloud velocity $\bar{V}_\perp'$ is given by

$$\bar{V}_\perp' = \left(\frac{2}{\lambda^* + 1}\right)\bar{E}' x \bar{B}/B^2 \tag{5}$$

Thus the sector of striation is in the direction $-V_\perp'$ which can be determined without knowledge of λ^*. To construct $-V_\perp'$, we first determine

$\bar{V}_\perp$ in the Earth fixed frame. In the neutral wind frame then $\bar{V}_\perp' = \bar{V}_\perp - \bar{V}_n$. Thus the direction of striations should be $\bar{V}_n - \bar{V}_\perp$. In the cases of interest (Esther and Fern) when striations were observed, $\bar{V}_\perp$ was obtained from radar measurements, but we must appeal to models for the neutral wind velocity.

Esther: Probe 51-3 detected a very strong density enhancement, but no striations. Since we do not have a neutral wind measurement due to the early cloud deployment in sunlit conditions, we can only estimate the wind velocity from measurements and models constructed for Millstone Hill (42.6°N; 71.5°W) as reported by Roble et al. (1977). For winter season at the local time of interest the neutral wind at release altitude is given as 94 m/s, 32° north of east. The ion cloud velocity $\bar{V}_\perp$ was determined from radar measurements (Gonzales, personal communication, 1977). The resulting vector $\bar{V}_n - \bar{V}_\perp$ was 38° north of geomagnetic east, while probe 51-3 passed through the south east portion of the cloud.

Probe 51-4, however, passed through the cloud much closer to the predicted region of instability. The radar map at 185 km is reproduced in Figure 7.1 along with the rocket position and its direction of travel. The position when striated plasma was observed is indicated as is the $(\bar{V}_n - \bar{V}_\perp)$ direction.

Fern: Only one probe functioned during the Fern event and it also detected strong striations. Detailed radar measurements are not available, but vector $\bar{V}_n - \bar{V}_\perp$ constructed as defined above was in the same quadrant of the cloud which the rocket penetrated. Striations were observed for a longer time since the rocket trajectory was steeper and hence more closely aligned with the cloud axis.

We thus conclude that the region of occurrence of the large scale structures is consistent with the $\bar{E}x\bar{B}$ instability as a causative mechanism.

2. Comparison With Linear and Nonlinear Theory

Before comparing the results with nonlinear theory and computer simulations, it is instructive to see why the striations develop at all. In Figure 7.2, the steep "backside" density gradient discussed earlier is depicted along with a sinusoidal perturbation. The picture is drawn

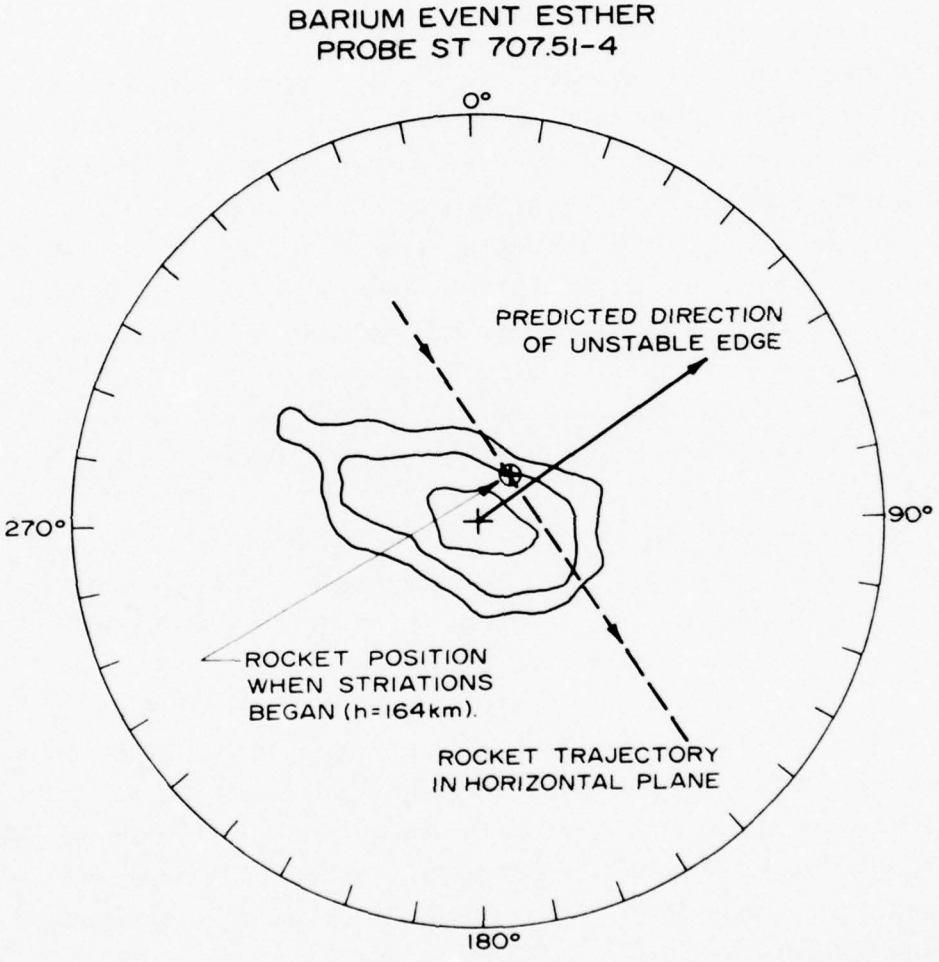

Figure 7.1. Cross section of ion cloud (from V. Gonzalez) and rocket trajectory for probe ST707.51-4 showing entrance of probe in striated region and predicted direction of development of instability.

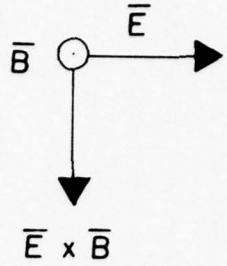

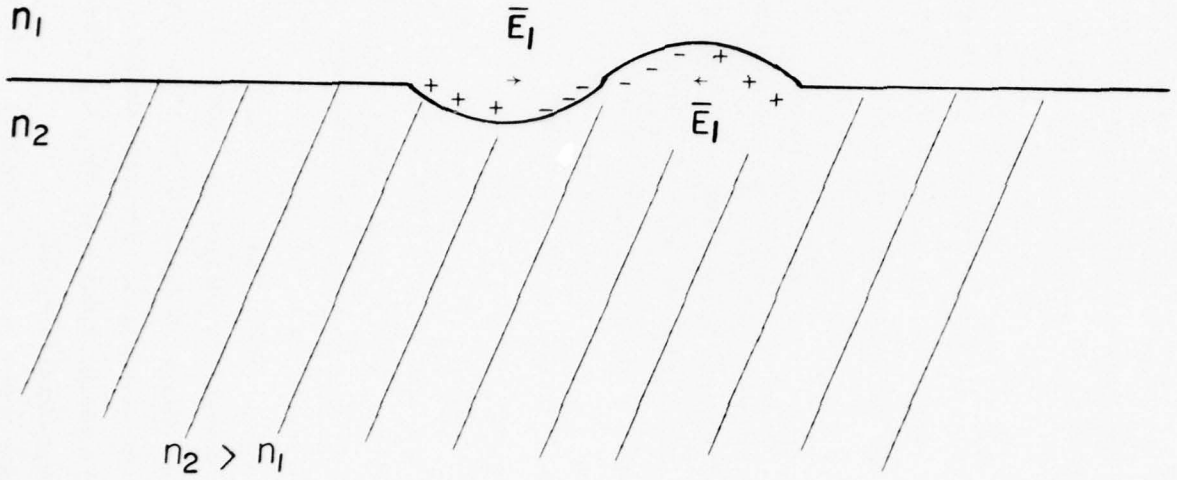

Figure 7.2. Illustration of development of striations caused by a buildup of change due to a perturbation (shown as sinusoidal perturbation) in the unstable sector. (see text)

in the frame of the neutral wind so there is only an electric field, which is pointed to the right, $\bar{B}$ is out of the paper, and $\bar{E}x\bar{B}$ downward. The Pedersen current flowing in the cloud piles-up positive and negative charge as indicated until the low density region (not cross-hatched) has a large enough electric field $\bar{E}+\bar{E}_1$ to make the current continuous across the boundary. The high density region will adjust charge to have a smaller electric field $\bar{E}-\bar{E}_1$ and will again be such that the current is continuous. These changes are in accordance with the conservation of charge equation

$$\bar{\nabla}\cdot\bar{J} = -\partial\rho/\partial t \qquad (6)$$

which says that charge will build-up in a way to keep $\bar{J}$ divergence free.

The resulting perturbation electric fields $\bar{E}_1$ and $-\bar{E}_1$ are oriented in such a way that the low density region will $\bar{E}_1 x\bar{B}$ drift into the cloud and the high density region will $-\bar{E}_1 x\bar{B}$ drift the opposite direction. The resulting perturbation is larger and hence will intercept even more charge and then grow larger still, an instability.

The linear growth rate has been derived by several workers (Simon, 1963; Linson and Workman, 1970) and tested in a computer simulation by Zabrusky et al. (1973) very successfully. As discussed below, the growth rate, γ, is a function of wavelength but is usually normalized to $\gamma_o = E'/BL\ s^{-1}$ where L is the density gradient in the cloud and E' is the magnitude of $\bar{E}+\bar{V}_n x\bar{B}$. For E'/B equal to 100 m/s and L of 4 km, $\gamma_o = 2.5\times10^{-2}$ seconds. The earliest striation measurements made in this rocket series were at t+42 minutes. Thus time was available for more than 50 e-folds ($e^{\gamma t}$) of any initial perturbations. Thus the clouds were clearly into the fully nonlinear regime and comparison with linear theory relevant only to the question of where the striations first should develop, and not their final amplitude nor their distribution of amplitude with respect to wavelength (spectrum). In fact, it is very clear that linear theory is deceiving in this regard since it predicts that the shortest wavelengths grow the fastest (Linson and Workman, 1970) whereas the observations show that the final state has more intensity at the longest wavelengths.

The nonlinear computer simulation of late time striation development performed by Scannapieco et al. (1976) seems most applicable to the data. In fact, the results are in excellent agreement with the

data. We concentrate on the Fern data here due to the longer time interval and hence the larger number of observed structures. In order to best compare the results to theory, we have detrended the data by fitting a third order polynomial to the time interval t+110 seconds to t+165.5 seconds and dividing each data point by the value of the curve at that point. This yields a curve of relative density with near zero mean value which is plotted in Figure 7.3. The distance scale was determined by projecting the rocket velocity onto the direction $(\bar{V}_n - \bar{V}_\perp) \times \bar{B}$. This is in the direction of the most unstable wave vectors in the linear theory and corresponds to the $\bar{x}$ direction in the paper by Scannapieco et al. (1976). The projected velocity was 179 m/s. The striations appear to have dominant power in the 1-5 km range and display very steep gradients.

The power spectrum of this data set has been determined by a Fast Fourier Transform and the result plotted in Figure 7.4. A power law is indicated with index 2.3 ± 0.2. As in all probe data this corresponds to a one-dimensional power law since an implicit integral is made by the detector as it passes across a two-dimensional structure. Scannapieco et al. have numerically calculated one-dimensional spectra for late time striations in the $\bar{x}$ direction and found an index between 2 and 3 for wavelengths between 0.6 and 12 km.

We thus conclude that the observations are in excellent agreement with the nonlinear theory for $\bar{E} \times \bar{B}$ instability (k between 0.5 and 10 km^{-1}).

3. Short Wavelength Irregularities

The peaks in the spectra at high frequencies (short λ) plotted earlier are remarkable since they appear in the otherwise undisturbed barium plasma. Since a Langmuir probe measures a scalar quantity and since there is no clear theoretical explanation for these waves, we cannot even be sure of the correct mapping between frequency and wavenumber space. For any electrostatic mode below the lower hybrid resonance, however, we expect phase velocities $\lesssim$ the acoustic speed which is comparable to the rocket velocity. Thus the frequency spectra must correspond to wavelengths between 0.1-10 meters. Such waves could have quite serious effects upon backscatter radars looking through the disturbed medium if the wave vector were parallel or anti-parallel to

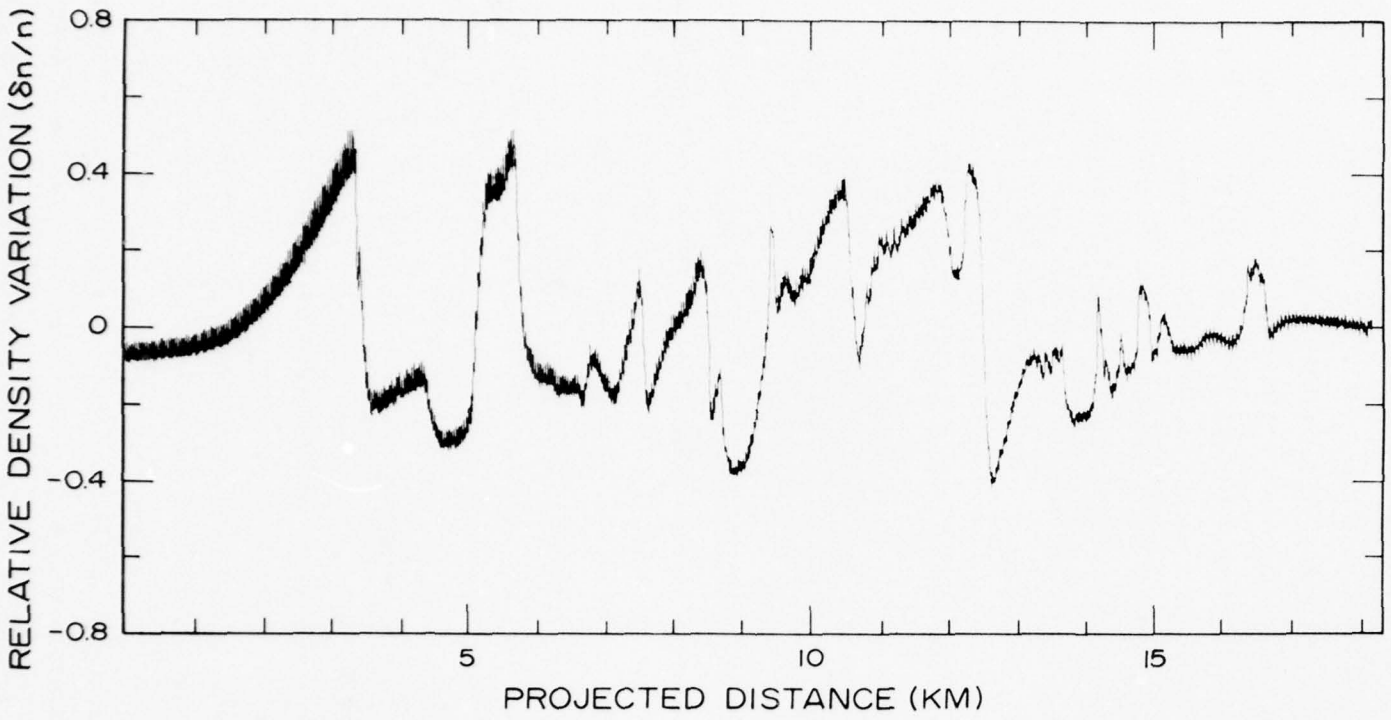

Figure 7.3. Detrended data showing electron density variations ($\delta n/n$) about the mean value for region of striations from probe results of rocket ST707.51-5 (Fern, 42 min) for the interval T+110 to T+165.5 seconds.

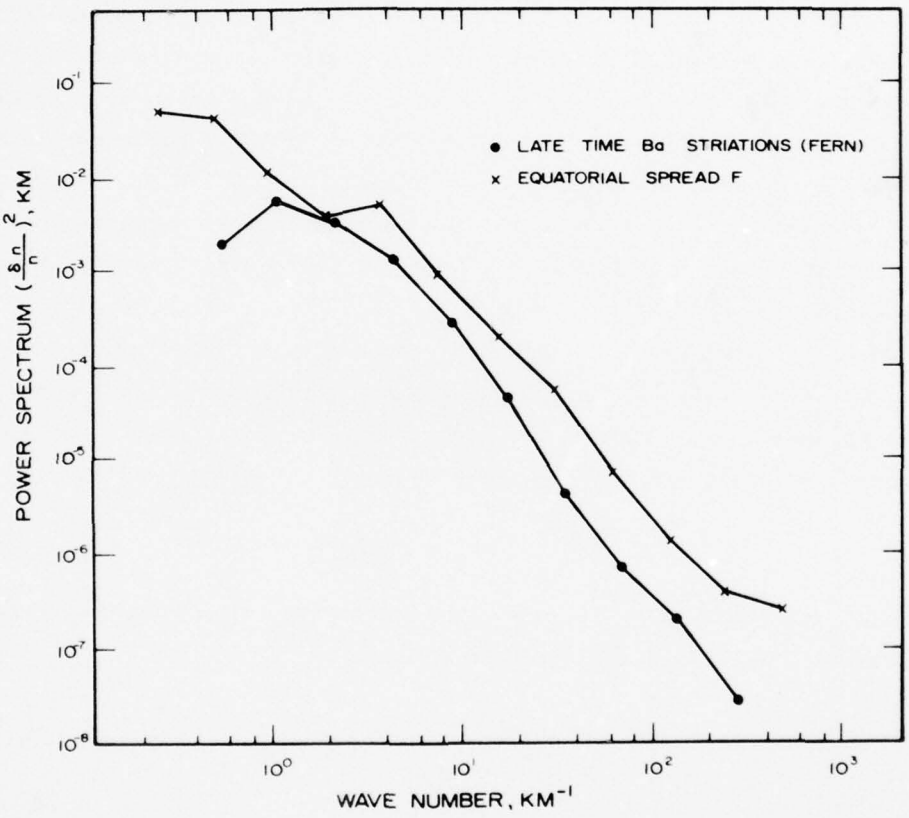

Figure 7.4. Power spectrum of the data of Figure 7.3 (Fern, ST707.51-5) determined by a Fast Fourier Transform (FFT). Also shown is a spectrum from a rocket flown into an equatorial spread F condition (*Costa and Kelley*, 1977).

radar look direction.

Similar band-limited electrostatic noise has been reported by Kelley et al. (1974); Timerin and Kelley (1977); and Kintner et al. (1976) in the earliest stages of very small barium releases. In the latter case there was also an electric field detector which showed that the waves were polarized parallel to the magnetic field direction. This suggests an ion acoustic mode and not the flute-like mode polarized perpendicular to $\bar{B}$ which are characteristic of the $\bar{E}x\bar{B}$, Rayleigh-Taylor and drift wave instabilities.

Counter-streaming of the cloud ions, barium, and the ambient ions has been suggested as a mechanism for generating ion acoustic waves. Even in the late time case studied here, there will be counter-streaming because of pressure gradients and the gravitational field. In the polar wind it is thought that the ambipolar electric field due to oxygen plasma expansion accelerates the light hydrogen ions. An estimate for the oxygen velocity due to a barium plasma induced electric field is

$$V_o = \frac{M_{Ba} g}{M_o \nu_{in}} \tag{7}$$

At 200 km, $\nu_{in}=7\ sec^{-1}$ and $V_o \sim 12$ m/s. This velocity is too low to generate ion acoustic waves in a two-stream process.

8. APPLICATIONS ASPECTS OF THE STRIATION OBSERVATIONS TO ARTIFICIAL AND NATURAL IONOSPHERIC DISTURBANCES

1. Application to Scintillations

In the preceeding section, it was shown that the experimental and theoretical basis for the understanding of striations in large ionospheric plasma clouds is on a very firm basis. The physical phenomena are understood as are the detailed time evolution of the irregularities. Further progress in understanding the propagation of radiowaves through such striated media depends upon proper application of the physical description to scintillation theory. The purpose of this section is to review the recent history of such scintillation calculations and to point out a possible mis-interpretation of the present results and the need for a new type of scintillation calculation.

Original models of scintillation effects assumed that the irregular medium could be characterized by some dominant scale size a, with larger and smaller scales of little importance. In such a case the irregularities could be modeled by a Gaussian distribution about a and the weak scattering, thin diffracting screen equations easily integrated to yield predictions of the scintillation effect at large distances from the screen. Rufenach (1975) realized that the magnetic field must play an essential role and suggested that, if indeed Gaussian, ionospheric irregularities should at least be anisotropic. He also introduced approximate calculations of scintillation effects due to non-Gaussian distributions of irregularities, namely, the isotropic and anisotropic power laws. Interest in the latter type of calculation has been high since (1) many natural phenomena result in power law forms for turbulent processes and (2) many in situ ionospheric rocket and satellite probes have indicated power law distributions of irregularities (Dyson et al., 1974; Sagalyn et al., 1976; Kelley et al., 1976; Morse et al., 1977).

These experiments have uniformly reported a power law spectrum varying as k^{-2}. Costa and Kelley (1977) have carried out mathematically rigorous calculations for the anisotropic power law spectra with arbitrary index and introduced a third, hybrid model, which is Gaussian along $\bar{B}$ and a power law in the plane perpendicular to $\bar{B}$. The hybrid model was meant to model flute-like processes in which the plasma

distribution along $\bar{B}$ is due to production, diffusion, and recombination processes (such as in barium striations) whereas the perpendicular structure is due to the instability process.

The fact that so much work has been done on power law calculations seems to imply that propagation through k^{-2} irregularities is well understood. The problem is that the ambigious k^{-2} spectrum may not be due to turbulence-like irregularities at all, but to the steep edges which develop upon the longest scale size structures. To draw an analogy, our present interpretation of the data is that the late time striations are more similar to breaking water waves than to the turbulent eddies in a rushing mountain stream.

The difference between these two descriptions is illustrated in Figure 8.1. In the upper plot the detrended data from probe 51-5 is plotted as done previously in Figure 7.3. The time series of data was then Fourier analyzed and one complex amplitude and phase determined for each of the discrete frequencies. Then an arbitrary phase angle was added to each of these complex numbers using a table of random numbers and the data was transformed back into the time domain and plotted in the Figure. The upper plot corresponds to no change in the phase angle and hence it returns to the original data sample. The two other data sets are from different random sets of phase angle. Since the phase angle does not affect the power spectrum, which is the absolute value of each of the complex numbers referred to above, the power spectrum of these three data streams is absolutely identical and, in fact, has already been plotted in Figure 7.4. We contend the two lower plots are physically different from the true data and conform to the concept of a "power law" irregularity spectrum as used in scintillation calculations. The real data does not. The reason that a random phase factor accomplishes this transformation is that steepened structures require a certain coherence in the phase of the Fourier components to produce the sharp edges. In turublence this coherence does not exist.

This type of analysis was first used by Costa and Kelley (1978), after a suggestion by D.T. Farley, to analyze naturally occurring equatorial spread F which, as discussed below, is a remarkably similar

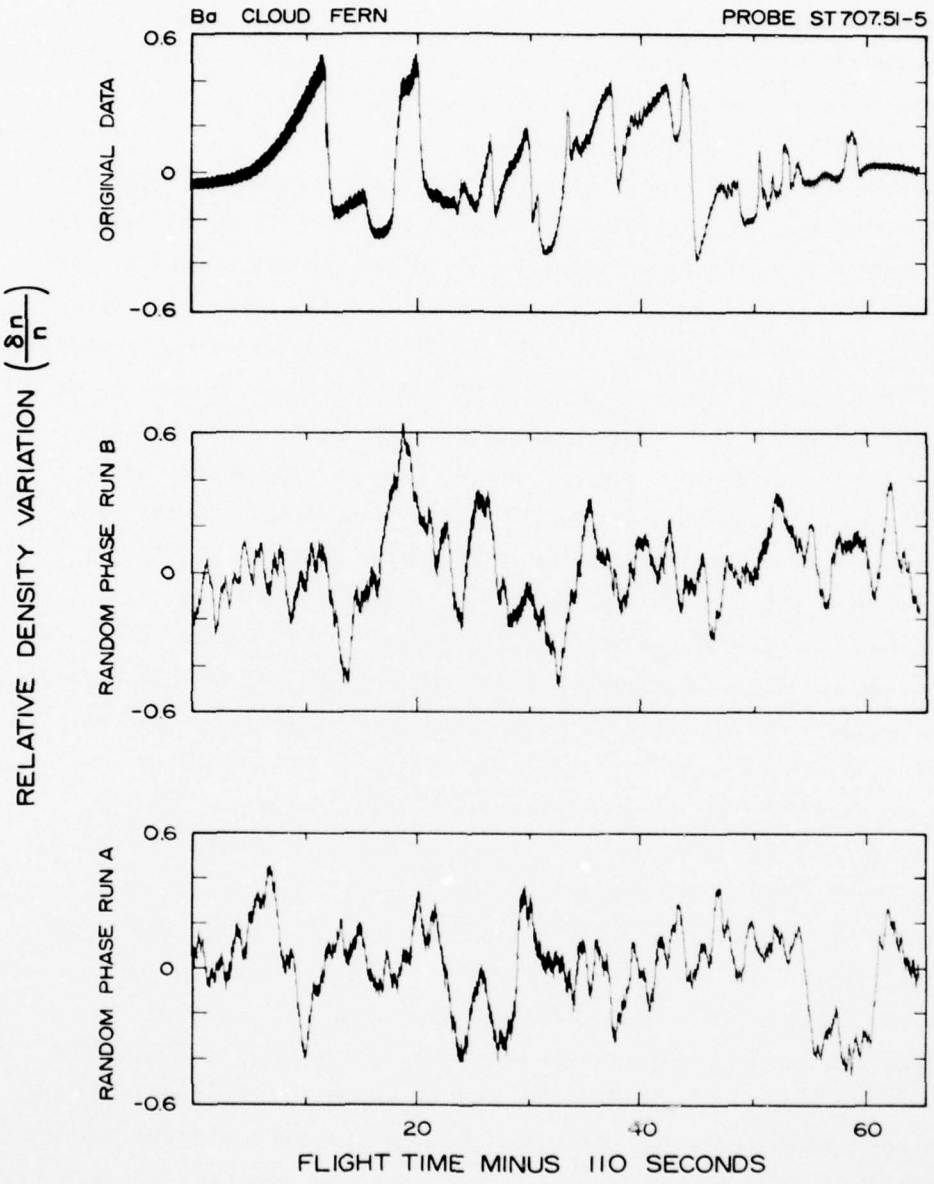

Figure 8.1. Electron density variations ($\Delta N/N$) about the mean value. The upper plot is the data from probe ST707.51-5 shown in Figure 7.3 while the bottom two plots are generated from adding arbitrary phase angle to the Fourier analyzed results of the upper data.

phenomenon to late time barium cloud striation. It thus seems clear that new models of scintillation phenomena using realistic irregularity models are required both for propagation through the natural and artificially disturbed ionospheric medium.

2. Relevance To The Naturally Disturbed Ionosphere-Equatorial Spread F

Extensive rocket, satellite, and radio wave probing of the equatorial ionosphere is currently underway in an effort to understand the naturally occurring phenomena called equatorial spread F. Various types of "spread F" occur worldwide and are casued by quite different processes. The equatorial type is one of the most interesting since it occurs far from regions such as the auroral zone where extraterrestrial effects complicate the theory, since it is readily accessible to experimental study, and since it causes quite remarkable intense scintillation problems extending even into the Gigahertz frequency range. A review of the status of equatorial scintillation and spread F theory, circa summer 1976, has been published by Basu and Kelley (1977) with an update to be presented at the IES symposium in January 1978 by the same authors.

The connection between late time striation of barium clouds and equatorial spread F is clearly indicated in Figure 8.2 where we plot probe data obtained on a NASA rocket flight from Natal, Brazil. The rocket probes detected intense irregularities on the bottomside of the equatorial F region (Costa and Kelley, 1978). The structures are very similar in appearance to the barium cloud data. In addition, both sets have similar power spectra as shown in Figure 7.4 where the two spectra are plotted. The spread F spectral index was $-2.14 \pm .15$.

These data were obtained below the peak in electron density which occurs at a relatively high altitude near the magnetic equator (~400 km). This is the region where the disturbances orginate and are first detected by ionosondes and backscatter radars. A remarkable feature of equatorial spread F, however, is that the structure is not confined to the bottomside but burrows through into the dense topside region where they have been detected as "holes" or "plumes" by satellites (McClure et al., 1977), rocket (Kelley et al., 1976), and radar (Woodman and La Hoz, 1976) techniques. The high plasma density in this topside region coupled with the large layer thickness accessible to the irregularity formation

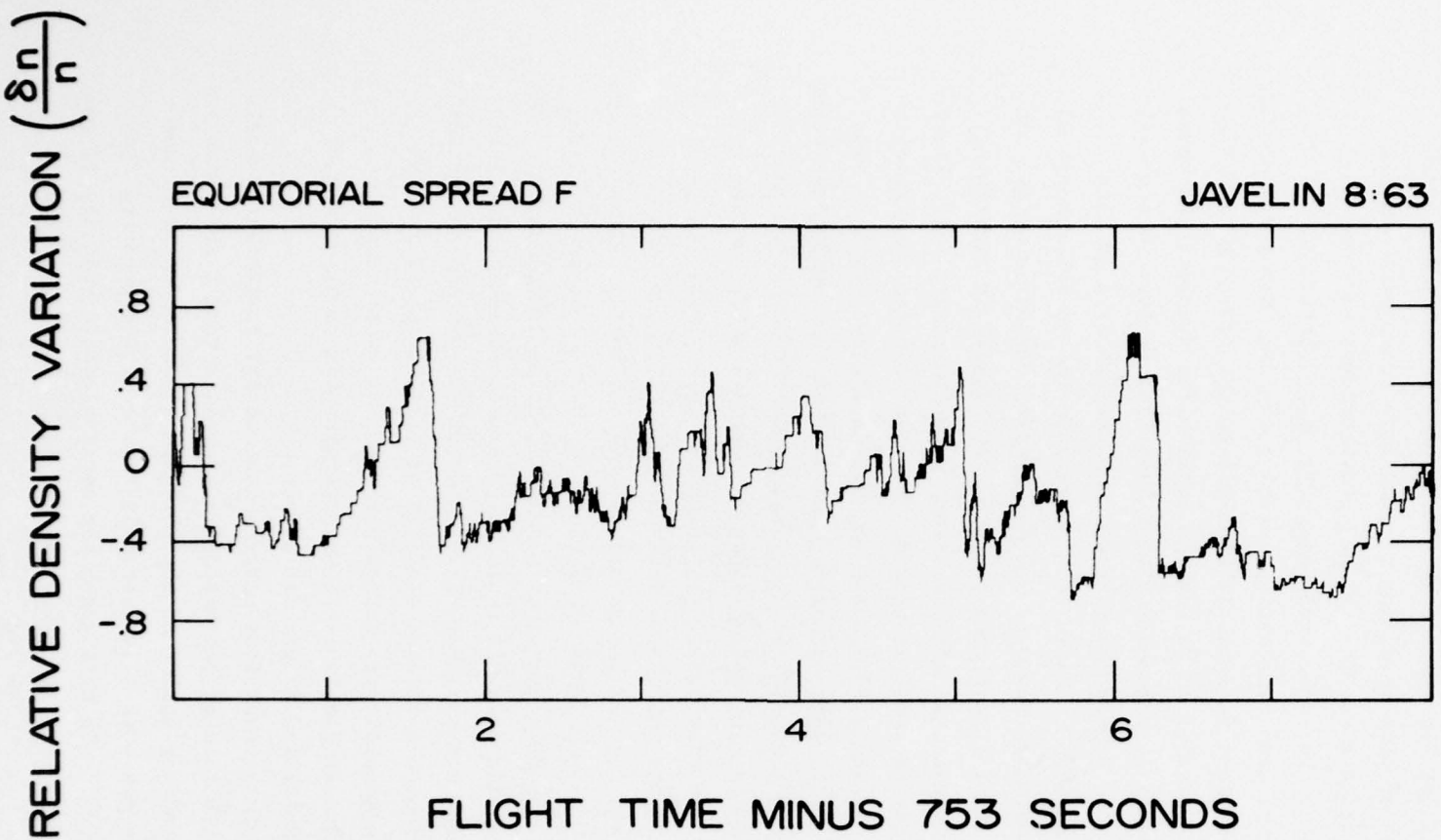

Figure 8.2. Electron density variations from rocket probe from Natal, Brazil into an equatorial spread F condition (*Costa and Kelley*, 1977).

process accounts for the intense VHF and Gigahertz scintillations.

Indications of this upwelling process have encouraged several workers to investigate the collisional gravitational Rayleigh-Taylor instability due to the encouraging geometry on the bottomside of the equatorial F peak, namely, $\bar{g}$ anti-parallel to $\bar{\nabla}n$ and both perpendicular to $\bar{B}$. This conditions is linearly unstable to the growth of flute mode waves. If $\bar{g}$ is parallel to $\bar{\nabla}n$, on the topside for example, the waves are linearly damped in a process almost identical in form to the backside instability of barium clouds (just replace $\bar{E}x\bar{B}$ by $\bar{g}$ in Figure 7.2 and $\bar{J}=\sigma p\bar{E}$ by $\bar{J}=nm\bar{g}x\bar{B}/B^2$. Under this model there is an interchange of high density flux tubes downward and low density regions upwards. As pointed out earlier, linear theory cannot be trusted in describing final states and nonlinear effects become very important. As a finite plasma hole pushes up into the topside (see the computer simulation by Scannapieco and Ossakow, 1976), the concept of a growth rate becomes meaningless and it is more appropriate to discuss the terminal velocity of such structures (Ott, 1977). Note that on the topside the $\bar{g}x\bar{B}$ current continues to flow, unlike Pedersen currents which require collisions, and hence can still supply charge to the edges of the bubbles. Thus charge causes the internal electric field to grow.

Thus it seems that on the topside a gravitationally driven process is necessary. This success of gravitational theories on the topside, however, should not preclude other possibilities at low altitudes. We contend here that the same $\bar{E}x\bar{B}$ instability process which causes late time striation in barium clouds contributes to the bottomside instability just after sunset and for a class of equatorial spread F which occurs during geomagnetically active periods. At other times the gravitational process continues to operate and will cause growth of irregularities initiated in the $\bar{E}x\bar{B}$ process.

The geophysical conditions under which the $\bar{E}x\bar{B}$ instability should enhance the growth rate of bottomside equatorial spread F are those when there is a strong uplift of the F region plasma. The key times alluded to above are both illustrated in Figure 8.3 reproduced from Fejer et al. (1977). In this graph the vertical drift velocity of the F region ionosphere over Jicamarca Peru is plotted along with an

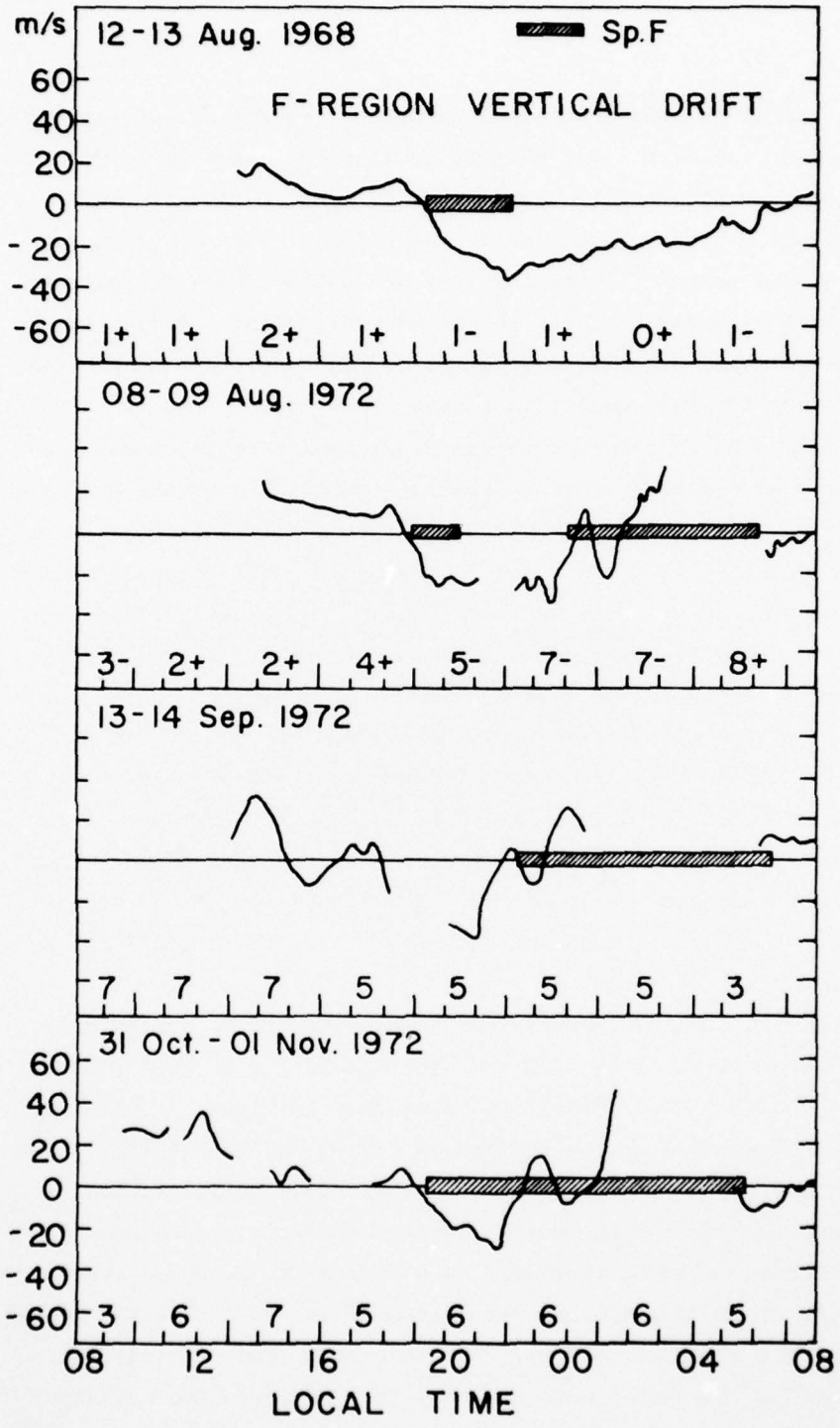

Figure 8.3. Examples of occurrence of spread-F compared with F-region vertical drift velocities over Jicamarca, Peru (from *Fejer et al.*, 1977).

indication of times when equatorial spread F occurred (cross-hatched areas) on several days. The pattern of vertical drift on 12-13 August 1968 is typical of the equatorial region. During the day the ionosphere drifts upward slowly. Near sunset there is often an enhanced upward velocity, seen this day at 1830 LT which is followed by a reversal to downward drift which lasts all night. Farley et al. (1970) have pointed out that initiation of equatorial spread F often is correlated with this uplift in plasma.

We argue here that this electric field and its enhancement near sunset plays an important role in the initiation of equatorial spread F. Before pursuing this further, we must point out that it is not just the increased electric field which controls the onset of equatorial spread F. When the sun sets on the E region recombination rapidly destroys the conductivity of that layer. This allows the build-up of the F layer perturbation electric fields E_1 shown in Figure 7.2 During the daytime such fields would be shorted out by the "conducting end plates", to use the vernacular of laboratory plasma physics. Recombination also eats away at the bottomside of the F layer to create a steep vertically directed gradient on the bottomside. These three factors then play a role in the $\bar{E}x\bar{B}$ instability of the equatorial F layer; the absence of an E region, the steep vertical gradient, and the eastward electric field.

In order to compare the relative importance of the collisional Rayleigh-Taylor instability with the $\bar{E}x\bar{B}$ instability we have plotted the linear growth rates of these two processes in Figure 8.4 for the same conditions using the results of Hudson and Kennel (1975) for the former and Linson and Workman (1970) for the latter. In making these plots, we have chosen sunspot maximum conditions (Johnson, 1960), a vertical drift velocity of 20 m/s (see Figure 8.3), and a gradient scale length of 20 km which has been measured during equatorial spread F conditions (Kelley et al., 1976). We see that in the altitude range less than 380 km the $\bar{E}x\bar{B}$ linear growth rate γ_o exceeds the Rayleigh-Taylor growth rate. This result is somewhat misleading since the $\bar{E}x\bar{B}$ growth rate decreases with increasing wavelength. However, the rocket data indicates that the characteristic wavelength of bottomside

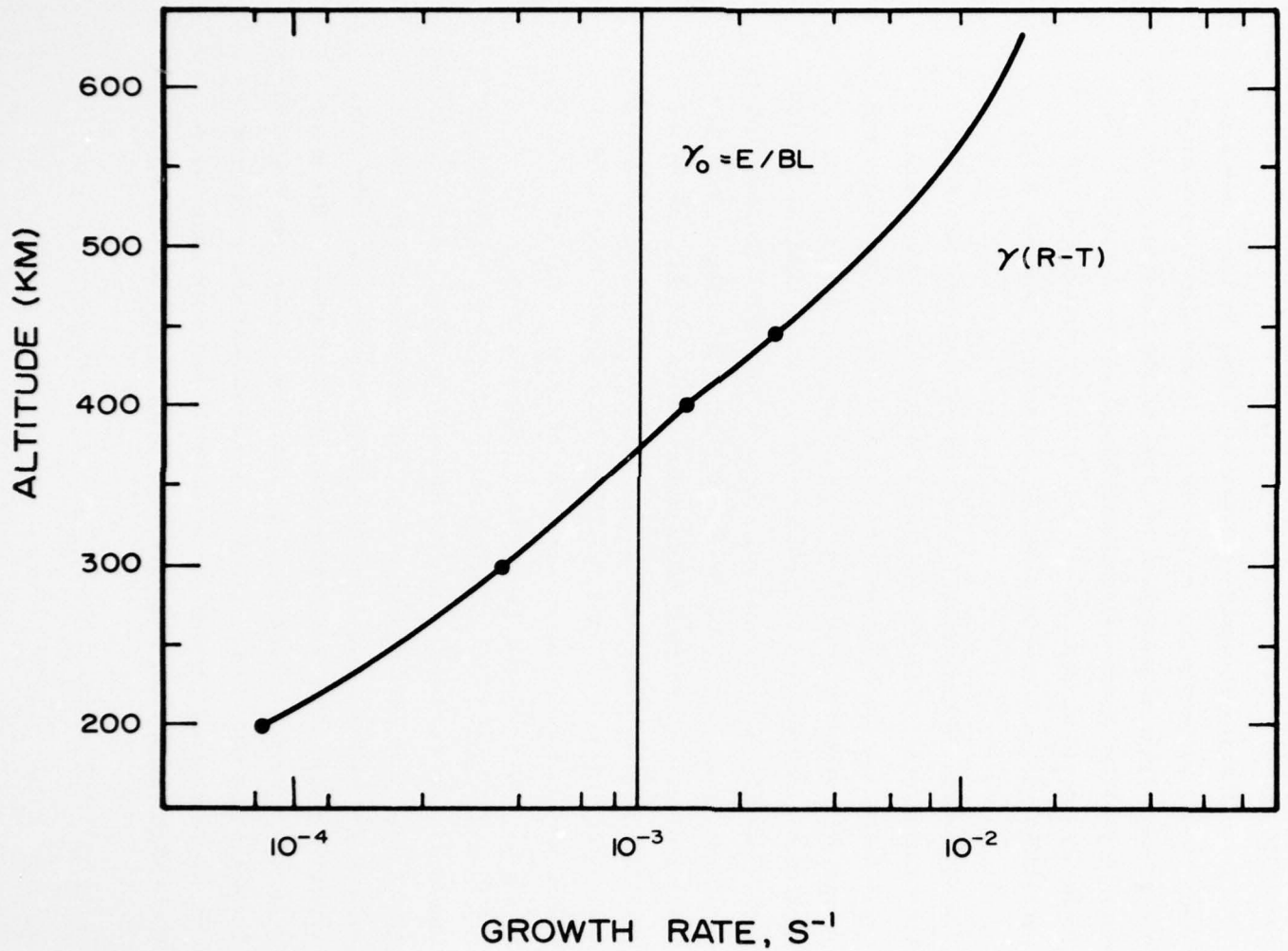

Figure 8.4. Plot of linear growth rates for the Rayleigh Taylor instability (γ(R-T)) and the $\bar{E} \times \bar{B}$ instability γ_0 for maximum solar conditions, vertical drift velocity of 20 m/s and a scale length of 20 km.

structures is ~5 km which for L=20 km, corresponds to kL=8π. The Linson-Workman growth rate at this value of kL is $0.75\gamma_o$ which exceeds γ_{RT} for h<350 km.

The re-initiation of equatorial spread F late in the evening on the other three nights plotted in Figure 8.3, may also be explained by this process since an anomalous reversal of the vertical drift from negative to positive preceeded this increase in irregularities. The particular change in equatorial electric field on August 8-9, 1972 was correlated with a sharp increase in the auroral zone electric field.

The relevance of the present late time barium cloud striation results to equatorial spread F is clear. As we have already pointed out the spectra and space domain signatures of the two phenomena are almost indistinguishable. The form of the linear growth rate is identical during times when the $\bar{E}x\bar{B}$ instability dominates the natural process. Even if the Rayleigh-Taylor mode is the more important linear process (during very slow or zero upward drifts) it seems likely that the final nonlinear state will be identical, since the $\bar{E}x\bar{B}$ growth rate decreases at long wavelength but still nonlinearly evolves into large scale irregularities. The Rayleigh-Taylor mode growth rate peaks at the lowest wavenumber and hence should be at least as effective as the $\bar{E}x\bar{B}$ instability in producing large scale irregularities.

It should be noted that Scannapieco et al. (1976) have pointed out the similarity between equatorial spread F bubbles and the depleted regions of late time barium striations. The latter propagate toward the front of the barium cloud since they have a larger $\bar{E}x\bar{B}$ drift than the central portion which is loading down the flux tubes. The effect should be even more pronounced than the simulation shown (see Figure 5 of Scannapieco et al., 1976), since in a one-dimensional cloud simulation the dense central portion cannot polarize and must continue to $\bar{E}x\bar{B}$ drift with the ambient velocity.

9. SUMMARY AND FUTURE EXPERIMENTAL DIRECTIONS

Summary

- We have measured late time striations in barium clouds and found their development to be in excellent agreement with the computer codes developed by the group at NRL. For example, they predicted the wavenumber power law index to be in the range -2 to -3 which compares favorably to the observed index of -2.16.

- A phase analysis of the data indicates that modeling the structures with an anisotropic power law, as typically done in existing scintillation calculations, may not properly take into account the physical structure of the irregularities. The power law results from nonlinear steepening of the large scale structures and not plasma turbulence.

- The results are remarkably similar to the bottomside instability in naturally occurring equatorial spread F. This implies that the nonlinear development of the two phenomena are identical. We also suggest that the $\bar{E}x\bar{B}$ instability at times is more important than collisional Rayleigh Taylor process in bottomside equatorial spread F.

- A bandlimited short wavelength instability operates in the portion of the cloud undisturbed by the striation process. No viable theory has been identified for this process. Depending upon the direction of the wave vectors, such irregularities may have strong effects upon VHF and UHF radars propagating through such a medium.

Future Experimental Directions

It can safely be said that the major process affecting large plasma cloud development in the mid-latitude ionosphere is well understood theoretically and that the theories have been checked in detail by experiment. Development of such a cloud at high latitudes may be significantly modified, however.

The major difference of importance is the large ambient electric field at high latitudes. The linear growth rate will, of course, be higher by a factor of ten (for E=50 mV/m which is not atypical). This may just decrease the time for full nonlinear development. It seems likely, though, that modest amplitude structures will peel off the

edges of the backside and flow in the $\bar{E}x\bar{B}$ direction. Since this ambient flow is east-west this will lead to an elongated curtain of irregularities stretching across the sky upstream from the cloud.

Other processes at high latitudes may effect the cloud development. Velocity shear instabilities may play a role, as may feedback from enhanced cold plasma density onto particle precipitation on the same field lines, and the existance of ambient irregularities.

As in the mid-latitude Stress experiment a detailed controlled experiment at high latitudes may yield important insights into the processes which create the irregularities in the natural disturbed F region at high latitude.

10. REFERENCES

Baker, K.D., E.F. Pound, and J.C. Ulwick, Digital plasma frequency probe for fine scale ionospheric measurements, *Small Rocket Instrumentation Techniques*, ed. by K.-I. Maeda, p. 49, North-Holland Publishing Co., Amsterdam, 1969.

Basu, S., and M.C. Kelley, Review of equatorial scintillation phenomena in light of recent developments in the theory and measurements of equatorial irregularities, to appear in *J. Atmos. Terr. Phys.*, 1977.

Costa, E., and M.C. Kelley, Evidence for and development of a 2-step theory for equatorial spread F., *J. Geophys. Res.*, submitted, 1977.

Costa, E., and M.C. Kelley, Ionospheric scintillation calculations based on in situ irregularity spectra, in press, *Radio Science*, 1977.

Davis, T.N., G.J. Romick, E.M. Wescott, R.A. Jeffries, D.M. Kerr, and H.M. Peek, Observations of the development of striations in large barium ion clouds, *Planet Space Sci.*, *22*, 67, 1974.

Dyson, P.L., J.P. McClure, and W.B. Hanson, In situ measurements of the spectral characteristics of F region ionospheric irregularities, *J. Geophys., Res., 79*, 1497, 1974.

Farley, D.T., B.B. Balsley, R.F. Woodman, and J.P. McClure, Equatorial spread F: Implications of VHF radar observations, *J. Geophys. Res.*, *75*, 7199, 1970.

Fejer, B.G. D.T. Farley, B.B. Balsley, and R.F. Woodman, Radar studies of anomalous velocity reversals in the equatorial ionosphere, *J. Geophys. Res., 81*, 4621, 1976.

Haerendel, G., R. Lust, and E. Rieger, Motion of artificial ion clouds in the upper atmosphere, *Planet Space Sci., 15*, 1, 1967.

Hudson, M.K., and C.F. Kennel, Linear theory of spread F., *J. Geophys. Res., 80*, 4581, 1975.

Jackson, J.D., *Classical Electrodynamics*, John Wiley and Sons, New York, NY, 380, 1960.

Kelley, M.C., C.A. Pedersen, U.V. Fahleson, D. Jones, and D. Kohn, Active experiments stimulating waves and particle precipitation with small ionospheric barium releases, *J. Geophys. Res., 79*, 2859, 1974.

Kelley, M.C., G.A. Haerendel, B.B. Balsley, and F.S. Mozer, Evidence for a Rayleigh-Taylor type instability and upwelling of depleted density regions during equatorial spread F., *Geophys. Res. Letts., 3*, 448, 1976.

Kintner, P.M., M.C. Kelley, G. Holmgren, and U.V. Fahleson, Plasmawave results from Trigger, Seattle IAGA/IAMAP Program 83, 1977.

Linson, L.M., and J.B. Workman, Formation on striations in ionospheric plasma clouds, *J. Geophys. Res.*, *75*, 3211, 1970.

McClure, J.P., W.G. Hanson, and J.H. Hoffman, Plasma bubbles and irregularities in the equatorial ionosphere, *J. Geophys. Res.*, *83*, 2650, 1977.

Morse, F.A., B.C. Edgar, H.C. Koons, C.J. Rice, W.J. Heikkila, J.H. Hoffman, B.A. Tinsely, J.D. Winningham, A.B. Christensen, R.F. Woodman, J. Pomalaza, and N.R. Teixeira, *Rpt SAMSO-TR-76-158*, Aerospace Corp., El Segundo, CA, 1976.

Ott, E., Theory of Rayleigh-Taylor bubbles in the equatorial ionosphere, submitted to *J. Geophys. Res.*, 1977.

Rufenach, C.L., Ionospheric scintillation by a random phase screen; Spectral approach, *Radio Sci.*, *10*, 155, 1975.

Sagalyn, R.C., M. Smiddy, and M. Ahmed, High latitude irregularities in the topside ionosphere based on ISIS I thermal probe data, *J. Geophys. Res.*, *79*, 4252, 1974.

Scannapieco, A.J., and S.L. Ossakow, Nonlinear equatorial spread F., *Geophys. Res. Letts.*, *3*, 451, 1976.

Scannapieco, A.J., S.L. Ossakow, S.R. Goldman, and J.M. Pierre, Plasma cloud striation spectra, *J. Geophys. Res.*, *81*, 937, 1976.

Schutz, S., G.J. Adams, and F.S. Mozer, Probe electric field measurements near a mid-latitude ionospheric barium release, *J. Geophys. Res.*, *78*, 6634, 1973.

Simon, A., Instability of a partially ionized plasma in crossed electric and magnetic fields, *Phys. Fluids*, *6*, 382, 1963.

Timerin, M., and M.C. Kelley, Rocket borne wave measurements in the dayside auroral oval, submitted to *J. Geophys. Res.*, 1977.

Woodman, R.f., and C. La Hoz, Radar observations of F region equatorial irregularities, *J. Geophys. Res.*, *81*, 5447, 1976.

Zabusky, M.H., J.H. Doies III, and F.w. Perkins, Deformation and striation of plasma clouds in the ionosphere, 2, Numberical simulation of a nonlinear two-dimensional model, *J. Geophys. Res.*, *78*, 711, 1973.

DISTRIBUTION LIST

DEPARTMENT OF DEFENSE

Assistant to the Secretary of Defense
Atomic Energy
ATTN: Executive Assistant

Command & Control Technical Center
ATTN: C-650

Defense Advanced Rsch. Proj. Agency
ATTN: NMRO
ATTN: STO

Defense Communication Engineer Center
ATTN: Code R410, J. McLean
ATTN: Code R820, R. Crawford

Defense Communications Agency
ATTN: Code 103, M. Raffensperger
ATTN: Code 101B
ATTN: Code 480
ATTN: Code 810, R. Rostron

Defense Documentation Center
Cameron Station
12 cy ATTN: TC

Defense Nuclear Agency
ATTN: RAAE
ATTN: DDST
ATTN: STVL
4 cy ATTN: TITL

Field Command, Defense Nuclear Agency
ATTN: FCPR

Interservice Nuclear Weapons School
ATTN: Document Control

Joint Chiefs of Staff
ATTN: J-3, WWMCCS Evaluation Office

Joint Strat. Tgt. Planning Staff
ATTN: JLTW-2

Livermore Division, Field Command, DNA
Lawrence Livermore Laboratory
ATTN: FCPRL

National Security Agency
ATTN: R52, J. Skillman
ATTN: R5

NATO School (SHAPE)
ATTN: U.S. Documents Officer

Under Secretary of Defense for Rsch. & Engrg.
ATTN: Strategic and Space Systems (OS)

WWMCCS System Engineering Org.
ATTN: R. Crawford

DEPARTMENT OF THE ARMY

U.S. Army Comm-Elec. Engrg. Instal. Agy.
ATTN: EED-PED, G. Lane

DEPARTMENT OF THE ARMY (Continued)

BMD Advanced Tech. Ctr.
Huntsville Office
ATTN: ATC-T, M. Capps

Harry Diamond Laboratories
ATTN: DELHD-NP
ATTN: DELHD-NP, F. Wimenitz
ATTN: DELHD-TI, M. Weiner

U.S. Army Foreign Science & Tech. Ctr.
ATTN: P. Crowley

U.S. Army Satellite Communications Agency
ATTN: Document Control

U.S. Army TRADOC Systems Analysis Activity
ATTN: ATAA-SA

DEPARTMENT OF THE NAVY

Office of Naval Research
ATTN: Code 461

Naval Electronic Systems Command
ATTN: Code 5011

Naval Intelligence Support Ctr.
ATTN: STIC 12, Mr. Dubbin

Naval Ocean Systems Center
ATTN: Code 2200

Naval Research Laboratory
ATTN: Code 5400, B. Wald
ATTN: Code 5430
ATTN: Code 7127, C. Johnson
ATTN: Code 7700, T. Coffey

Naval Surface Weapons Center
ATTN: Code F31

Navy Space Systems Activity
ATTN: Code 52

Strategic Systems Project Office
ATTN: NSP-2141
ATTN: NSSP-2722, F. Wimberly

DEPARTMENT OF THE AIR FORCE

AF Geophysics Laboratory, AFSC
ATTN: OPR-1, J. Ulwick
ATTN: PHD, J. Mullen
ATTN: SUOL, Research Library
ATTN: PHP, J. Aarons
ATTN: PHD, J. Buchau

AF Weapons Laboratory, AFSC
ATTN: DYT, L. Wittwer
ATTN: DYT, M. Fry
ATTN: SUL
ATTN: DYC, J. Kamm

DEPARTMENT OF THE AIR FORCE (Continued)

Air Force Technical Applications Center
ATTN: TN

Air Force Avionics Laboratory, AFSC
ATTN: AAD, A. Johnson

Foreign Technology Division, AFSC
ATTN: NICD Library

Rome Air Development Center, AFSC
ATTN: Documents Library/TSLD

Space and Missile Systems Organization/MN
Air Force Systems Command
ATTN: MNNL, Lt Col Kennedy

Space and Missile Systems Organization/SK
Air Force Systems Command
ATTN: SKA, M. Clavin

Space and Missile Systems Organization/YA
Air Force Systems Command
ATTN: YAT, L. Blackwelder

Strategic Air Command
ATTN: NRT
ATTN: ADWATE, B. Bauer
ATTN: XPFS, B. Stephan

DEPARTMENT OF ENERGY

Lawrence Livermore Laboratory
ATTN: Doc. Con. for Technical Information
Dept. Library

Los Alamos Scientific Laboratory
ATTN: Doc. Con. for R. Jefferies
ATTN: Doc. Con. for J. Wolcott
ATTN: Doc. Con. for J. Zinn

Sandia Laboratories
ATTN: Doc. Con. for W. Brown
ATTN: Doc. Con. for D. Dahlgren
ATTN: Doc. Con. for T. Wright
ATTN: Doc. Con. for J. Martin

OTHER GOVERNMENT AGENCIES

Central Intelligence Agency
ATTN: RD/SI, Rm. 5G48, Hq. Bldg.,
for OSI/PSTD

Institute for Telecommunications Sciences
National Telecommunications & Info. Admin.
ATTN: W. Utlaut

NASA
Goddard Space Flight Center
ATTN: ATS-6, P. Corrigan

DEPARTMENT OF DEFENSE CONTRACTORS

Aerospace Corp.
ATTN: N. Stockwell
ATTN: SMFA for PWW
ATTN: J. Carter
ATTN: T. Garfunkel

DEPARTMENT OF DEFENSE CONTRACTORS (Continued)

Berkeley Research Associates, Inc.
ATTN: J. Workman

Boeing Co.
ATTN: D. Murray
ATTN: G. Keister

Charles Stark Draper Laboratory, Inc.
ATTN: J. Gilmore
ATTN: D. Cox

Computer Sciences Corp.
ATTN: J. Spoor
ATTN: C. Nail

Cornell University
Department of Electrical Engineering
ATTN: D. Farley, Jr.

Electrospace Systems, Inc.
ATTN: P. Phillips

ESL, Inc.
ATTN: J. Marshall
ATTN: C. Prettie

General Electric Co.
ATTN: F. Reibert

General Electric Co.-TEMPO
Center for Advanced Studies
ATTN: DASIAC
ATTN: W. Knapp

General Research Corp.
Santa Barbara Division
ATTN: J. Garbarino
ATTN: J. Ise, Jr.

Geophysical Institute
University of Alaska
ATTN: Technical Library

University of Illinois
Department of Electrical Engineering
ATTN: K. Yeh

Institute for Defense Analyses
ATTN: E. Bauer

International Tel. & Telegraph Corp.
ATTN: Technical Library

JAYCOR
ATTN: S. Goldman

Johns Hopkins University
Applied Physics Laboratory
ATTN: T. Potemra
ATTN: Document Librarian
ATTN: J. Dassoulas

Kaman Sciences Corp.
ATTN: T. Meagher

Linkabit Corp.
ATTN: I. Jacobs

DEPARTMENT OF DEFENSE CONTRACTORS (Continued)

University of Lowell Research Foundation
ATTN: K. Bibl

MIT Lincoln Laboratory
ATTN: D. Towle

McDonnell Douglas Corp.
ATTN: Technical Library Services

Mission Research Corp.
ATTN: R. Bogusch
ATTN: F. Fajen
ATTN: D. Sappenfield
ATTN: R. Hendrick
ATTN: R. Kilb

Mitre Corp.
ATTN: W. Sen

Mitre Corp.
ATTN: W. Hall
ATTN: W. Foster

R&D Associates
ATTN: W. Karzas
ATTN: R. Lelevier
ATTN: B. Gabbard

Rand Corp.
ATTN: C. Crain
ATTN: E. Bedrozian

DEPARTMENT OF DEFENSE CONTRACTORS (Continued)

Raytheon Co.
ATTN: B. Adams

Science Applications, Inc.
ATTN: D. Hamlin
ATTN: D. Sachs
ATTN: L. Linson

SRI International
ATTN: D. McDaniels
ATTN: W. Chesnut
ATTN: C. Rino
ATTN: V. Gonzales
ATTN: R. Leadabrand
ATTN: R. Hake, Jr.

Technology International Corp.
ATTN: W. Boquist

Utah State University
ATTN: K. Baker
ATTN: J. Ulwick
ATTN: M. Kelley
ATTN: L. Howlett
ATTN: G. Allred
ATTN: D. Delorey
ATTN: N. Crossbard